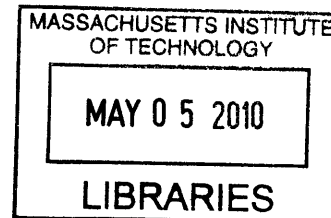


**Phase-Space Representation of Digital
Holographic and Light Field Imaging with
Application to Two-Phase Flows**

ARCHIVES



by

Lei Tian

Submitted to the Department of Mechanical Engineering
in partial fulfillment of the requirements for the degree of

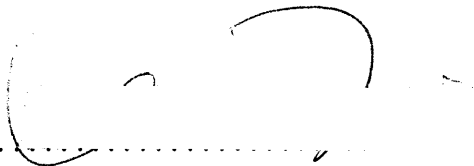
Master of Science in Mechanical Engineering

at the

MASSACHUSETTS INSTITUTE OF TECHNOLOGY

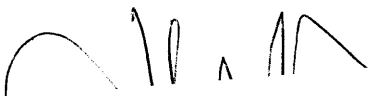
February 2010

© Massachusetts Institute of Technology 2010. All rights reserved.

Author 

Department of Mechanical Engineering

January 15, 2010

Certified by 

George Barbastathis

Associate Professor

Thesis Supervisor

Accepted by 

David E. Hardt

Chairman, Department Committee on Graduate Theses

Phase-Space Representation of Digital Holographic and Light Field Imaging with Application to Two-Phase Flows

by

Lei Tian

Submitted to the Department of Mechanical Engineering
on January 15, 2010, in partial fulfillment of the
requirements for the degree of
Master of Science in Mechanical Engineering

Abstract

In this thesis, two computational imaging techniques used for underwater research, in particular, two-phase flows measurements, are presented. The techniques under study, digital holographic imaging and light field imaging, are targeted at different flow conditions. In low-density flows, particles and air bubbles in water can be imaged by a digital holographic imaging system to provide 3D flow information. In the high-density case, both occlusions and scattering become significant, imaging through these partial occlusions to achieve object detection is possible by integrating views from multiple perspectives, which is the principle of light field imaging. The analyses on the digital holographic and light field imaging systems are carried out under the framework of phase-space optics.

In the holographic imaging system, it is seen that, by tracking the Space bandwidth transfer, the information transformation through a digital holographic imaging system can be traced. The inverse source problem of holography can be solved in certain cases by posing proper *priori* constraints. As is in the application to two-phase flows, 3D positions of bubbles can be computed by well tuned focus metrics. Size statistical distribution of the bubbles can also be obtained from the reconstructed images.

Light field is related to the Wigner distribution through the generalized radiance function. One practical way to sample the Wigner distribution is to take intensity measurements behind an aperture which is moving laterally in the field. Two types of imaging systems, the light field imaging and the integral imaging, realize this Wigner sampling scheme. In the light field imaging, the aperture function is a rect function; while a sinc aperture function in the integral imaging. Axial ranging through the object space can be realized by digital refocusing. In addition, imaging through partial occlusion is possible by integrating properly selected Wigner samples.

Thesis Supervisor: George Barbastathis
Title: Associate Professor

Acknowledgments

I would like to thank, first and foremost, my thesis advisor, Professor George Barbas-tathis. I came to MIT without any optics or electro-magnetics background. He has been warmly and patiently guiding me during the course of my research and giving me many helpful suggestions.

I would also like to thank my colleges (past and present) at the 3D Optical Systems group for all their help and many helpful discussion: Laura A. Waller, Jose A. Dominguez-Caballero, Nick Loomis, Se Baek Oh, Aditya Bhakta, Yuan Luo, Hanhong Gao, Jason Ku, Justin Lee, Chih-Hao Chang, Se Young Yang, Satoshi Takahashi, Martin Deterre, Hyun-Jin In, Nader Shaar, Anthony Nichol, Baile Zhang, and Xiaogang Liu. Especially, I would like to thank Jose A. Dominguez-Caballero and Nick Loomis for their many helps in my first year when George is at Singapore, they gave me many helpful guidance on optics, signal processing and other advices in research.

Finally, I would like to thank my parents for their love, support, and encouragement.

Contents

1	Introduction	11
1.1	Fundamentals of imaging systems	12
1.2	Imaging of two-phase flows	13
1.3	Phase-space optics	14
1.4	Outline of the thesis	14
2	Introduction to phase-space optics	17
2.1	Wigner distribution function	18
2.1.1	Properties of the WDF	19
2.1.2	WDF of special optical signals and transformations	22
2.2	Space-bandwidth product in phase-space	27
2.2.1	Numerical space-bandwidth product	28
2.2.2	Space-bandwidth product in phase-space	29
3	Holographic imaging in phase-space and its application to two-phase flows	31
3.1	Holography in phase-space	34
3.1.1	Holographic information in phase-space	34
3.1.2	Space-bandwidth transfer in different holographic imaging system setups	38
3.2	Digital holographic recording and reconstruction	45
3.2.1	Digital holography recording	45
3.2.2	Digital reconstruction	46

3.3	Digital holography applied to two-phase flows	54
3.3.1	Automated data analysis	55
3.4	Conclusion	66
4	Light field imaging in phase-space	75
4.1	Light fields and the Wigner distribution function	78
4.1.1	Light fields	78
4.1.2	Radiance and the Wigner distribution	79
4.1.3	Light field and the Wigner distribution	83
4.2	Wave optics analysis of light field imaging	85
4.2.1	Field at the sensor plane	85
4.2.2	Coherent Point Spread Function	88
4.2.3	Incoherent Point Spread Function	88
4.2.4	Partially coherent imaging using a light field imaging system .	101
4.2.5	Simulation results	104
4.3	Wave optics analysis of integral imaging	108
4.3.1	Coherent Point Spread Function	109
4.3.2	Incoherent Point Spread Function	110
4.3.3	Partially coherent imaging	113
4.3.4	Simulation results	114
4.4	Conclusion	118
5	Conclusion	121
5.1	Digital holographic imaging	122
5.2	Light field imaging	123

List of Figures

1-1	Schematic of imaging system.	12
2-1	Relations among the the Wigner distribution, Ambiguity function, and the Cohen's class distribution.	22
2-2	Special optical signals in the space domain and their corresponding Wigner distribution functions.	23
2-3	Representation of common optical transforms in Wigner space	27
2-4	Space-bandwidth product of an optical signal after different optical transformations	30
3-1	Interferometric recording.	32
3-2	Wavefront reconstruction	33
3-3	Holographic information in phase-space.	35
3-4	The WDF of a hologram.	37
3-5	In-line holography setup.	39
3-6	The space-bandwidth transfer and the Fourier spectrum of in-line holography	40
3-7	Off-axis holography setup.	41
3-8	The space-bandwidth transfer and the Fourier spectrum of off-axis holography	42
3-9	Space-bandwidth transfer in hologram reconstruction.	44
3-10	Digital in-line holography setup.	46
3-11	Fresnel diffraction kernel	50
3-12	Point source holograms and their WDFs.	52

3-13	Digital in-line holography setup.	54
3-14	Sample holograms of the studied two-phase flows.	56
3-15	Schematic diagram of the digital reconstruction algorithm.	57
3-16	Demonstration of the edge minimum intensity focus metric	60
3-17	Key steps of the proposed DH data analysis algorithm applied to the air-in-water two-phase flows	61
3-18	Applying GMM to separate overlapping bubbles	62
3-19	Key steps of the proposed DH data analysis algorithm applied to the oil-in-water two-phase flows	64
3-20	Data processing result from a 1000×1000 -pixel hologram of the air- in-water two-phase flows.	67
3-21	Bubble size data fitted to lognormal and gamma distributions.	68
3-21	Bubble size data fitted to lognormal and gamma distributions.	69
3-22	Bubble size distribution parameter evolution over eight consecutive holograms; error bars show the 90% confidence intervals for the esti- mated distribution parameters.	70
3-23	Evolution of the holograms of the air-in-water two-phase flows.	71
3-24	Data processing result from a 900×900 -pixel hologram of the oil-in- water two-phase flows.	72
3-25	Oil-droplet size distribution parameter evolution over 21 consecutive holograms spaced approximately 15 seconds apart; error bars show the 90% confidence intervals for the estimated distribution parameters.	73
3-26	Evolution of the holograms of the oil-in-water two-phase flows.	74
4-1	Schematics of integral imaging and light field imaging	76
4-2	Conventional single lens imager	77
4-3	Light field parameterizations.	79
4-4	Illustration of the definition of the radiance function $B(\mathbf{r}, \mathbf{s})$	80
4-5	Measurable WDF and radiance	84
4-6	Light field imaging system setup.	86

4-7	Illustration of the incoherent point spread function of the light field imaging system.	92
4-8	Wigner distribution function of a rect function	93
4-9	Illustration of the information spread on the sensor plane in the light field imager	95
4-10	Illustration of incoherent point spread function	97
4-11	Digital processing to compute the image of the in-focus object and digitally refocus to the defocused object	98
4-12	The Fourier Slicing Theorem	100
4-13	Geometrical defocus	100
4-14	Illustration of input spatial frequency and output spatial frequency .	103
4-15	Sampling in the Wigner space by a light field imaging system	105
4-16	Simulation results of sampling in the Wigner space using the light field imaging system	106
4-16	(Continued) Simulation results of sampling in the Wigner space using the light field imaging system	107
4-17	Integral imaging system setup.	109
4-18	Illustration of incoherent point spread function of integral imaging system.	112
4-19	Sampling in the Wigner space by a integral imaging system	115
4-20	Simulation results of sampling in the Wigner space by an integral imaging system	116
4-20	(Continued) Simulation results of sampling in the Wigner space by an integral imaging system	117

Chapter 1

Introduction

Historically, advances in optical imaging instrumentation, such as the microscope and the telescope, have facilitated diverse scientific discovery. In recent decades, the fusion of computational power and conventional optical imaging techniques has created a new paradigm known as computational imaging. The design of computational imaging systems simultaneously incorporates traditional and novel optical elements, electronic optical sensors, signal processing and advanced mathematical algorithms. In addition, it leverages the speed and accuracy of optical processing to enable highly computational systems, which optimize the tradeoffs between the optical and digital world. Generally, a computational imaging system comprises two kinds of elements, including analog or field transforming elements, such as lenses, apertures and wave-plates, and digital or intensity transforming elements, such as CCD and CMOS. Computational imaging involves a series of transformations on the optical signals. The intensity patterns recorded on the detector are not necessarily the image that are physically analogous to the original objects. All required is that the intensity patterns encode sufficient information to allow the recovery of the object after appropriate digital processing operations.

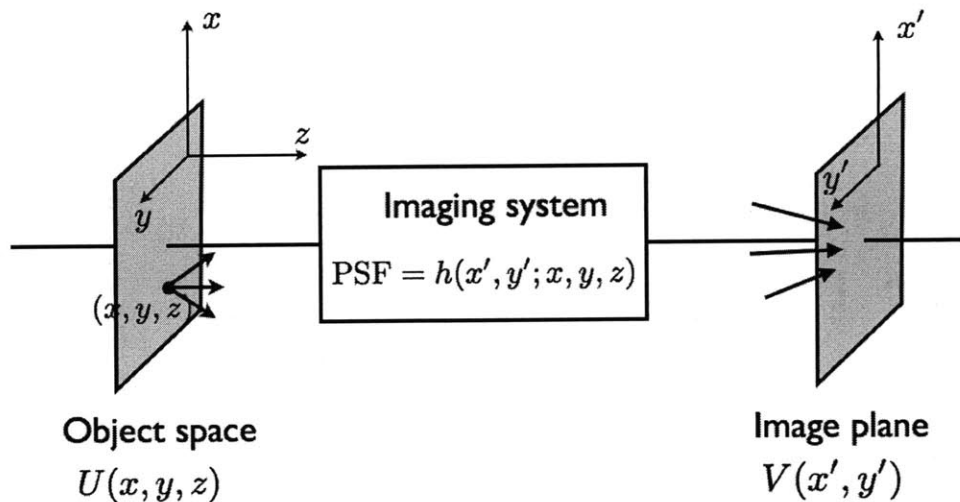


Figure 1-1: Schematic of imaging system.

1.1 Fundamentals of imaging systems

Figure 1-1 shows a schematic of an imaging system. The object is three dimensional (3D) with point emitters located in the 3D space. Radiation from these sources serves as the input to the imaging system. The detector is typically two dimensional, which records some intensity pattern due to the inputs. The imaging system is completely described by the impulse response [34]. In general, the impulse response is a 5D function [28, 10, 101], $h(x', y'; x, y, z)$ that relates the 2D output image $V(x', y')$ to the 3D input $U(x, y, z)$. The physical interpretation of the impulse response depends on the nature of the illumination. Spatially coherent illumination involves a linear superposition of fields whereas quasi-monochromatic spatially incoherent illumination results in a linear combination of the intensities from from the point emitters in the object space. In partially coherent illumination case, the impulse response relates to the propagation of mutual intensity [8].

1.2 Imaging of two-phase flows

Two-phase flows occur in a wide variety of application areas, e.g., meteorology, fuel injection and combustion, chemical reactors, pollution, and cavitation. Many efforts have been devoted to their investigation by experimental methods and modeling approaches. Nevertheless, due to the complex fluid dynamics of turbulent, 3D, two-phase flows, the physics of bubble formation, propagation and annihilation is not well understood. During the past decades, numerous imaging techniques have been developed for imaging two-phase flows in the past decades. They can be summarized into three main categories: single point measurement techniques, such as phase-Doppler imaging [64]; planar imaging techniques, such as particle imaging velocimetry (PIV) [3]; and 3D imaging techniques. Obviously, 3D imaging is preferable due to the 3D nature of two-phase flows. Existing 3D imaging techniques such as neutron radiography [61], scanning particle imaging [9] and defocusing digital particle imaging velocimetry [83] typically trade off system complexity for spatial and temporal resolution.

Holography [31] is able to record and reconstruct, in a single shot, information about the history of the field propagation within an entire 3D volume of interest. Moreover, Digital holography and digital holographic image processing [94] have recently become feasible due to advances in mega-pixel electronic sensors, e.g. CCD and CMOS, with high spatial resolution and high dynamic range. Unlike traditional imaging techniques, digital holography is lens-less, i.e. image formation occurs purely through digital processing that reverses the effects of diffraction on the optical field. This becomes possible because holography allows access to the phase information present in the optical field. Having the information available in digital form, digital holography gives the access to the large amount of 3D information, e.g. velocity, vorticity, void fraction and etc., in the flow fields to be extracted by computational method.

In high-density flows, the hologram of particle/bubble flows taken from a single view becomes a speckle-like noisy image. In addition, significant occlusions prevent targets from being observed due to information loss. One way to overcome the chal-

lence of partial occlusion is to integrate views from multiple perspectives. Occlusion differs from view to view, and by digitally integrating multiple views, the shape of a target embedded in an occlusive media can be reconstructed.

1.3 Phase-space optics

Phase-space optics refers to a representation of optical signals in an artificial configuration space simultaneously providing space and spatial frequency information. The Wigner distribution [5] is one of the mathematical tools for representation optical signals in the phase-space. It has been widely used for analyzing holographic imaging [53], volume holographic imaging [70], axial imaging [68], coherence imaging [69], wavefront coding [21], integral imaging display [29], and phase imaging [67]. In optics, spatial frequency is determined by the angle of the rays, which relates to the concept of perspective. The Wigner analysis provides a guideline of how to implement the idea of integrating views from different perspectives. The principle is that, if we can sample the optical signal in multiple positions and their corresponding spatial frequencies, by combining all the data digitally, the target can be recovered.

1.4 Outline of the thesis

This thesis aims to advance the field of computational imaging by developing novel computational imaging techniques used for underwater research, allowing flow characterization and object detection and identification. The techniques under study, digital holographic imaging and light field imaging, are targeted at different flow conditions. In low-density flows, particles and air bubbles in water can be imaged by a digital holographic imaging system to provide 3D flow information. In the high-density case, both occlusions and scattering become significant, and imaging flow itself becomes difficult. However, imaging through these partial occlusions to achieve object detection is still possible by integrating views from multiple perspectives, which is the principle of light field imaging. The analyses on the digital holographic and light field

imaging systems are carried out under the framework of phase-space optics.

In Chapter 2, phase-space optics is introduced. The basic concept and properties of the Wigner distribution function and other related phase-space analysis functions are summarized. The space-bandwidth product (SBP) is fundamental for analyzing the performance of an optical system. The SBP is a specific area in the Wigner space. The transformations on the SBP of an optical signal by first-order optics are analyzed in the Wigner space.

In Chapter 3, phase-space optics is applied to analyze the holographic imaging system. The SBPs recorded by different types of holographic setups are studied. Finally, an in-line holographic imaging system is applied to the two-phase flow studies.

In Chapter 4, the Wigner distribution is related to the radiance. This bridges the intensity measurements to the Wigner space samples. Two types of imaging systems, the light field imaging and integral imaging, are studied. The capabilities and limitations of sampling in the Wigner space using these two systems are presented.

In Chapter 5, conclusions of this thesis and directions for future research are presented.

Chapter 2

Introduction to phase-space optics

Phase-space optics refers to a representation of optical signals in a space simultaneously providing information about spatial properties of the signal and its angular spectrum, or equivalently in terms of its temporal and time-frequency characteristics. Phase-space representation provides unique insights of the physical phenomena. As compared to the classical Fourier analysis, which provides only global spectrum of the signal, phase-space analysis uses both local space and spatial frequency information simultaneously.

The Wigner distribution function (WDF) is one of the mathematical tools for representation signals in the phase-space. It was introduced by Wigner [111] in mechanics in 1932. The WDF is only one example of the larger class of joint representation called Cohen's class distribution function [14]. For instance, in the signal processing community, the Wigner-Ville distribution is widely used as a joint time-frequency transform. Closely connected with the WDF through a double Fourier transform, the ambiguity function [116] is used by the radar community for representing signals simultaneously carrying information about the down range of the target and its velocity.

The WDF, being well suited to combine the physics of wave propagation with the power of signal processing in the joint space-spatial frequency domain, was first introduced into optics by A. Walther [107, 109] to relate partial coherence to radiometry and revisited by M. J. Bastiaans [5, 6, 7] a few years later.

2.1 Wigner distribution function

The WDF of an coherent optical field $f(x)$, with its Fourier transform as $F(u)$, can be defined as

$$\mathcal{W}(x, u) = \int f(x + x'/2) f^*(x - x'/2) \exp\{-i2\pi u x'\} dx' \quad (2.1)$$

where $f(x)$ is a scalar function at position x , and u is the local spatial frequency component. One-dimensional signal is being discussed in this notation for convenience, and higher dimensional analysis can be carried out in similar fashion.

The physical meaning of x' and u' in (2.1) is evident by looking at the form $\Gamma(x_1, x_2)$

$$\Gamma(x_1, x_2) = f(x_1) f^*(x_2). \quad (2.2)$$

In the partially coherent case, $\Gamma(x_1, x_2)$ is recognized as mutual intensity function by taking the ensemble average. We use the coordinate transformation

$$x = \frac{1}{2}(x_1 + x_2), \quad \xi = x_2 - x_1 \quad (2.3)$$

Now it is clear that Wigner distribution $\mathcal{W}(x, u)$ arises “midway” of mutual intensity.

Instead of the definition in the space domain, there exists an equivalent definition in the frequency domain, reading

$$\mathcal{W}(x, u) = \int F(u + u'/2) F^*(u - u'/2) \exp\{i2\pi x u'\} du' \quad (2.4)$$

where $F(u)$ is the Fourier transform of $f(x)$.

It is also worth mentioning the definition of cross-Wigner distribution function of two functions $f(x)$ and $g(x)$,

$$\mathcal{W}_{fg} = \int f(x + x'/2) g^*(x - x'/2) \exp\{-i2\pi u x'\} dx' \quad (2.5)$$

2.1.1 Properties of the WDF

Here, some of the important properties of the WDF are summarized [103] as follows.

1. *Inversion*: The original function can be recovered from its WDF within a constant phase factor as

$$f(x) = \frac{1}{f^*(0)} \int \mathcal{W}(x/2, u) \exp\{i2\pi xu\} du. \quad (2.6)$$

2. *Realness*: The WDF is a real function:

$$\mathcal{W}(x, u) = \mathcal{W}^*(x, u). \quad (2.7)$$

3. *Projection property*: Although the WDF is real, it is not necessarily non-negative; this prohibits a direct interpretation of the WDF as an energy density function (or radiance function). Nevertheless, several projection integrals of the WDF can be interpreted as energy quantities.

Intensity of the signal

$$I(x) = |f(x)|^2 = \int \mathcal{W}(x, u) du, \quad (2.8)$$

Fourier spectrum intensity of the signal

$$|F(u)|^2 = \int \mathcal{W}(x, u) dx, \quad (2.9)$$

Total energy of the signal

$$E = \iint \mathcal{W}(x, u) dx du = \int |f(x)|^2 dx = \int |F(u)|^2 du. \quad (2.10)$$

4. *Region properties*: If $f(x) = 0$ for $x \geq x_0$, $\mathcal{W}(x, u) = 0$ for $x \geq x_0$.

5. *Interference:* Due to the bilinear nature of the WDF, the WDF of the sum of two signals $f(x) + g(x)$ is the WDF of $f(x)$, $g(x)$ and an interference term

$$\mathcal{W}_{f+g}(x, u) = \mathcal{W}_f(x, u) + \mathcal{W}_g(x, u) + \mathcal{W}_{f,g}(x, u) + \mathcal{W}_{g,f}(x, u). \quad (2.11)$$

6. *Multiplication and Convolution:*

$$\text{If } g(x) = f(x)h(x)$$

$$\mathcal{W}_g(x, u) = \mathcal{W}_f(x, u) *_u \mathcal{W}_h(x, u) \quad (2.12)$$

where $*_u$ indicates convolution in u .

$$\text{If } g(x) = f(x) * h(x)$$

$$\mathcal{W}_g(x, u) = \mathcal{W}_f(x, u) *_x \mathcal{W}_h(x, u) \quad (2.13)$$

where $*_x$ indicates convolution in x .

7. *Correlation:*

$$\text{If } g(x) = \int f(x + x')h(x')dx'$$

$$\mathcal{W}_g(x, u) = \int \mathcal{W}_f(x + x', u)\mathcal{W}_h(x', -u)dx'. \quad (2.14)$$

8. *Shifting and Modulation property:*

$$\text{If } g(x) = f(x - x_0)$$

$$\mathcal{W}_g(x, u) = \mathcal{W}_f(x - x_0, u). \quad (2.15)$$

$$\text{If } g(x) = e^{i2\pi u_0 x} f(x)$$

$$\mathcal{W}_g(x, u) = \mathcal{W}_f(x, u - u_0). \quad (2.16)$$

9. *Instantaneous frequency:* For a coherent signal $f(x) = |f(x)| \exp\{i2\pi\phi(x)\}$, the instantaneous frequency is defined as $d\phi(x)/dx$, it can be derived from $\mathcal{W}_f(x, u)$

through

$$\frac{d\phi}{dx} = \frac{\int u \mathcal{W}_f(x, u) du}{\int \mathcal{W}_f(x, u) du}. \quad (2.17)$$

10. *Ambiguity function:* The ambiguity function (AF) $A(x', u')$ [81] is defined by

$$\mathcal{AF}(u', x') = \int f(x + x'/2) f^*(x - x'/2) \exp\{-i2\pi u'x\} dx, \quad (2.18)$$

is related to the WDF through a double Fourier transform:

$$\mathcal{AF}(u', x') = \iint \mathcal{W}_f(x, u) \exp\{i2\pi(x'u - u'x)\} dx du \quad (2.19)$$

One thing to notice about AF is that it takes the form similar to autocorrelation function ($\int f(x + x'/2) f^*(x - x'/2) dx$), which makes it particularly convenient for analysis in some cases.

11. *Cohen's class distribution function:* Cohen's class distribution function [14] is a generalized phase-space representation. The definition of the Cohens class distribution function is as follows:

$$C(x, u) = \iiint e^{i2\pi\xi(s-x)} h(\xi, x') f(s + x'/2) f^*(s - x'/2) e^{-i2\pi ux'} d\xi ds dx'. \quad (2.20)$$

This definition can be rearranged to two forms, which have more obvious physical meaning. The first is

$$C(x, u) = \iint \mathcal{AF}(\xi, x') h(\xi, x') \exp\{-i2\pi(\xi x + x'u)\} d\xi dx' \quad (2.21)$$

where $\mathcal{AF}()$ is the ambiguity function, and the physical meaning of h is a filter in ambiguity space. The second is

$$C(x, u) = \iint H(x - s, u - u') \mathcal{W}(s, u') ds du' \quad (2.22)$$

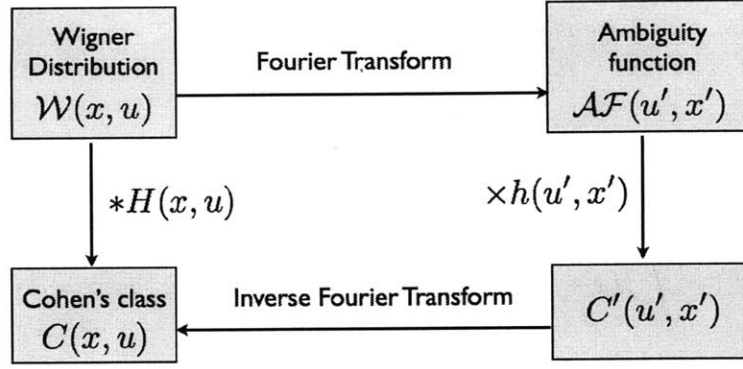


Figure 2-1: Relations among the the Wigner distribution, Ambiguity function, and the Cohen's class distribution.

where

$$H(x, u) = \iint h(x', u') \exp\{-i2\pi(xx' + uu')\} dx' du'. \quad (2.23)$$

This can be recognized as a convolution in the Wigner space and H is the convolution kernel, which is the 2D Fourier transform of h . The relations among the the Wigner distribution, Ambiguity function, and the Cohen's class distribution are illustrated in fig. 2-1.

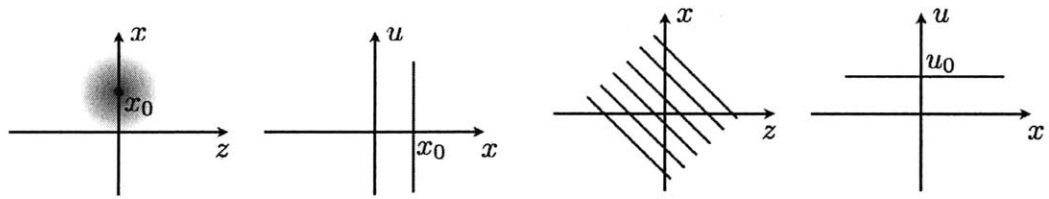
2.1.2 WDF of special optical signals and transformations

The local spatial frequency corresponds to the angle of a ray in geometrical optics [34]; hence, the WDF provides a connection between ray and wave optics. More importantly, the WDF is useful to analyze how light behaves as it propagates. As will seen in the following, the WDF can provide intuitive illustrations of light propagation in first-order optical systems by geometrical transformations.

We shall start by looking at special optical signals.

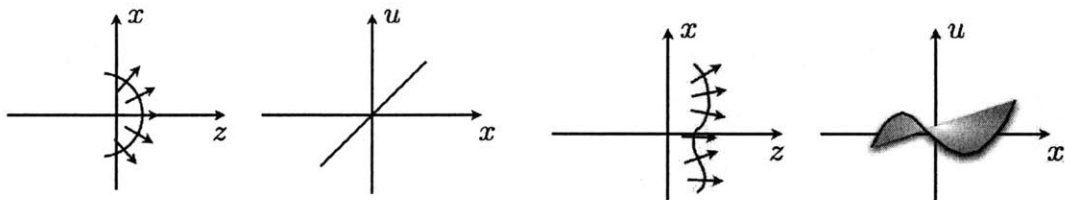
1. *Point source*: A point source located at the position x_0 can be described by the impulse signal $f(x) = \delta(x - x_0)$. Its WDF takes the form

$$\mathcal{W}(x, u) = \delta(x - x_0). \quad (2.24)$$



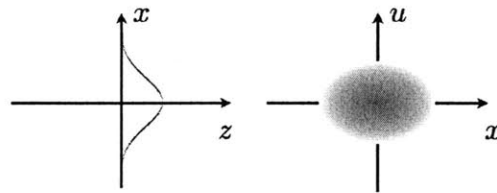
(a) Point source

(b) Plane wave



(c) Spherical wave (quadratic-phase signal)

(d) Smooth-phase signal



(e) Gaussian signal

Figure 2-2: Special optical signals in the space domain and their corresponding Wigner distribution functions.

as shown in fig. 2-2(a).

2. *Plane wave:* A plane wave with spatial frequency u_0 can be described by $f(x) = \exp\{i2\pi u_0 x\}$. Its WDF takes the form

$$\mathcal{W}(x, u) = \delta(u - u_0). \quad (2.25)$$

as shown in fig. 2-2(b).

3. *Spherical wave:* A spherical wave in paraxial approximation can be described by a quadratic-phase signal $f(x) = \exp\{i\pi\alpha x^2\}$. Its WDF takes the form

$$\mathcal{W}(x, u) = \delta(u - \alpha x). \quad (2.26)$$

as shown in fig. 2-2(c).

4. *Smooth-phase signal:* A smooth-phase signal $f(x) = \exp\{i\phi(x)\}$. Its WDF takes the form

$$\mathcal{W}(x, u) \simeq \delta(u - d\phi/dx). \quad (2.27)$$

by neglecting interference terms, as shown in fig. 2-2(d).

5. *Gaussian signal:* A Gaussian signal $f(x) = \exp\{-\frac{\pi}{\sigma^2}(x - x_0)^2\}$. Its WDF takes the form

$$\mathcal{W}(x, u) = \exp\left\{-\left(\frac{2\pi}{\sigma^2}(x - x_0)^2 + \frac{\sigma^2}{2\pi}u^2\right)\right\}. \quad (2.28)$$

which is a function that is Gaussian in both x and u , as shown in fig. 2-2(e).

Next, we will consider some common optical transformations.

1. *Fresnel propagation:* Fresnel propagation describes free space propagation under paraxial approximation. It relates the input and output fields by

$$g(x) = \int f(x') \exp\left\{i\frac{\pi}{\lambda z}(x - x')^2\right\} dx \quad (2.29)$$

So the WDF of the output field takes the form

$$\mathcal{W}_g(x, u) = \mathcal{W}_f(x - \lambda z u, u) \quad (2.30)$$

which is an x -shear of the input WDF, as shown in fig. 2-3(a), and the amount of shear is linearly proportional to the propagation distance.

2. *Chirp modulation (lens)*: Chirp modulation, which can be achieved by a lens or a quadratic phase mask, relates the input and output fields by

$$g(x) = f(x) \exp \left\{ i \frac{\pi}{\lambda f} x^2 \right\} \quad (2.31)$$

where f is the focal length if a lens is used or relates to the chirping rate in other cases. So the WDF of the output field takes the form

$$\mathcal{W}_g(x, u) = \mathcal{W}_f(x, u + \frac{x}{\lambda f}) \quad (2.32)$$

which is a u -shear of the input WDF, as shown in fig. 2-3(b), and the amount of shear is inversely proportional to f .

3. *Fourier transform*: The space and spatial frequency domains are interchanged as expected for a Fourier transformer.

$$\mathcal{W}_g(x, u) = \mathcal{W}_f(-u, x). \quad (2.33)$$

as shown in fig. 2-3(c).

4. *Fractional Fourier transform*: For 1D signal, Fractional Fourier transform (FRFT) [58, 59, 74] is the only transformation for phase-space rotation [50]. The input and output WDF are related by

$$\mathcal{W}_g(x, u) = \mathcal{W}_f(x \cos(\phi) - u \sin(\phi), u \cos(\phi) + x \sin(\phi)). \quad (2.34)$$

where ϕ is the rotation angle. The fractional degree is defined by $P = \phi/(\pi/2)$. Similarly, we can take a projection of $\mathcal{W}_g(x, u)$ over u , the result is given by [52]

$$|\text{FRFT}[f(x)]|^2 = \int \mathcal{W}_g(x, u) du = R[\mathcal{W}_f; \phi] \quad (2.35)$$

where $R[\mathcal{W}_f; \phi]$ indicates the Radon transform of \mathcal{W}_f at angle ϕ . (2.35) forms the principle of phase-space tomography [30, 88]. It should also be noted that in 2D signal case, there are other two phase-space rotational transformations [96], which are outside the scope of this thesis.

5. *Magnifier*: If an optical signal is magnified by m , its WDF takes the form

$$\mathcal{W}_g(x, u) = \mathcal{W}_f(mx, u/m), \quad (2.36)$$

as shown in fig. 2-3(e).

6. *First-order optical systems*: Similar to the matrix transformations in geometrical optics, it is shown that an ABCD-matrix can also be used to relate the input and output WDF in first-order optical systems [6].

$$\mathcal{W}_g(x, u) = \mathcal{W}_f(Ax + Bu, Cx + Du). \quad (2.37)$$

So the input (x, u) and output (x', u') space and spatial frequency are related by

$$\begin{bmatrix} x' \\ u' \end{bmatrix} = \begin{bmatrix} A & B \\ C & D \end{bmatrix} \begin{bmatrix} x \\ u \end{bmatrix} \quad (2.38)$$

where the ABCD-matrix is symplectic [15], with determinant equals to unity. It is easy to see that the matrices for the previous five basic optical transformations

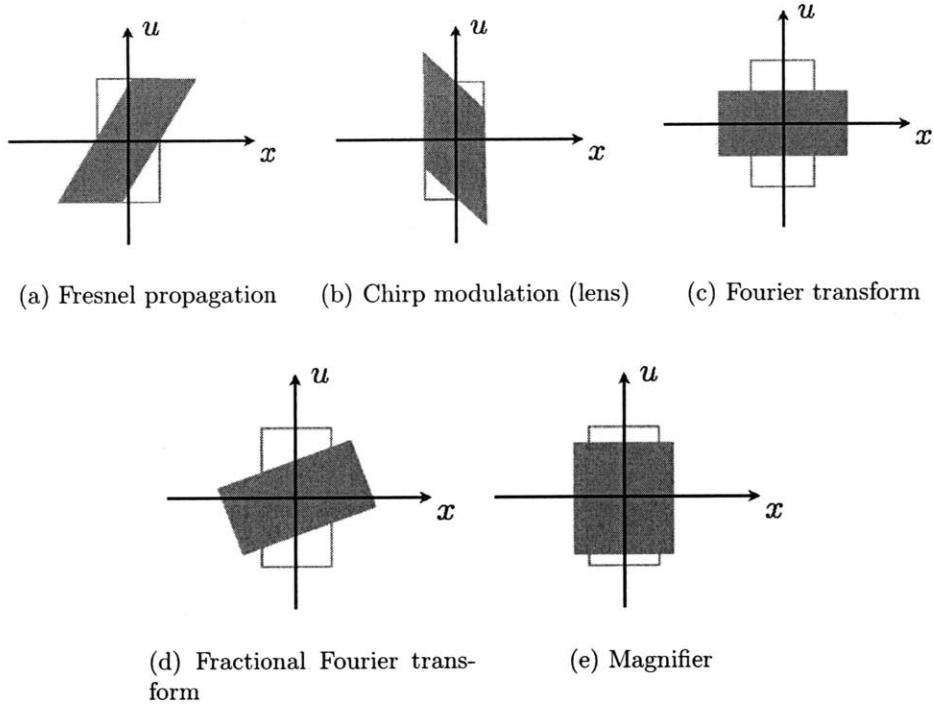


Figure 2-3: Representation of common optical transforms in Wigner space, where the blank rectangles indicate original fields and solid rectangles represent transformed fields.

are, respectively,

$$\begin{aligned}
 & \begin{bmatrix} 1 & -\lambda z \\ 0 & 1 \end{bmatrix}, \begin{bmatrix} 1 & 0 \\ 1/\lambda f & 1 \end{bmatrix} \begin{bmatrix} 0 & -1 \\ 1 & 0 \end{bmatrix}, \\
 & \begin{bmatrix} \cos(\phi) & -\sin(\phi) \\ \sin(\phi) & \cos(\phi) \end{bmatrix}, \begin{bmatrix} m & 0 \\ 0 & 1/m \end{bmatrix}.
 \end{aligned} \tag{2.39}$$

2.2 Space-bandwidth product in phase-space

The space-bandwidth product (SBP) is fundamental for judging the performance of an optical system. It measures the amount of information of an optical signal or capability for recording optical signals of an optical system. The SBP was first

defined as a pure number that counts the degrees of freedom of the system in the context of the resolution limit [16, 25]. With the introduction of optical phase-space, a more insightful description of SBP was introduced in terms of a specific area in the Wigner (x, u) domain [51]. It should also be noted that there are two different but related SBP definitions: SBP of an optical system and an optical signal. To evaluate the performance of an optical system, it is important to measure how well the system SBP satisfies the signal SBP requirement.

2.2.1 Numerical space-bandwidth product

A signal $f(x)$ can be assumed to be band-limited (2.40) and space-limited (2.41) if the majority amount (e.g. 90%) of energy is within the interval of Δx in space and $\Delta \nu$ in spatial frequency.

$$F(\nu) = \int f(x) \exp\{-i2\pi\nu x\} dx \approx 0, \quad \text{if } |\nu| > \Delta\nu/2. \quad (2.40)$$

$$f(x) \approx 0, \quad \text{if } |x| > \Delta x/2. \quad (2.41)$$

According to the Nyquist sampling theorem, the signal can be recovered if we sample the signal at equidistant sampling point separated by $\delta x = 1/\Delta\nu$. The total number of these samples is

$$N_I = \Delta x / \delta x = \Delta x \Delta \nu. \quad (2.42)$$

The number N_I is the SBP of the optical signal.

Similarly, we can analyze the numerical SBP of an optical system N_H . The physical size of the sensor/film $\Delta x'$ sets the spatial limits. The spatial frequency limits come from two aspects. First, the numerical aperture (NA) of the optical system limits the acceptable angle (spatial frequency) range $\Delta \nu'$ of the system. Second, the pixel size δ_{pix} of the sensor/film sets the sampling rate of the system. So the Nyquist frequency limit of the system is $\pm 1/(2\delta_{pix})$, $\Delta \nu' = 1/\delta_{pix}$. So SBP of an optical system

is

$$N_H = \Delta x' \Delta \nu' \quad (2.43)$$

$$N_H = \Delta x' / \delta_{pix} = N_{pix}, \text{ if the pixel size sets the limit,} \quad (2.44)$$

where N_{pix} is the number of pixels of a sensor/film. (2.44) also shows that the number of pixels of the sensor/film measures the numerical SBP of the sensor/film. This is evident if we recall that SBP measures the amount of information that an optical system can record.

2.2.2 Space-bandwidth product in phase-space

Equations (2.40) and (2.41) define a rectangular symmetrical region $\mathcal{W}(x, \nu)$ in phase-space, whose surface area equals the SBP of the signal, as shown in fig. 2-4 (a). As the optical signal propagates through different optical systems, the shape of $\mathcal{W}(x, \nu)$ changes correspondingly, as discussed in Section 2.1. Fig. 2-4 (b-e) shows the changes of the shape of the signal SBP $\mathcal{W}(x, \nu)$ after Fresnel propagation (b), a lens (c), a Fourier transform (d), and a fractional Fourier transform (e). The shape changes of the SBP by different first-order optical systems can be described as a linear transformation

$$\text{SBP}(x', \nu') = \text{SBP}(Ax + B\nu, Cx + D\nu). \quad (2.45)$$

It is clear that the (ABCD) coefficients here are the same as what we derived in previous discussion about WDF transformations after a first-order optical system. So the area of the non-zero region in phase-space (color areas in fig. 2-4) conserves, which proves the existence of the numerical SBP that a single number can describe the information content of an optical signal. On the other hand, if we want to record the signal without information loss, the numerical SBP N_I only sets the lower bound of the system SBP requirement. A more general condition is

$$\text{SBP}_I(x, \nu) \subset \text{SBP}_H(x, \nu) \quad (2.46)$$

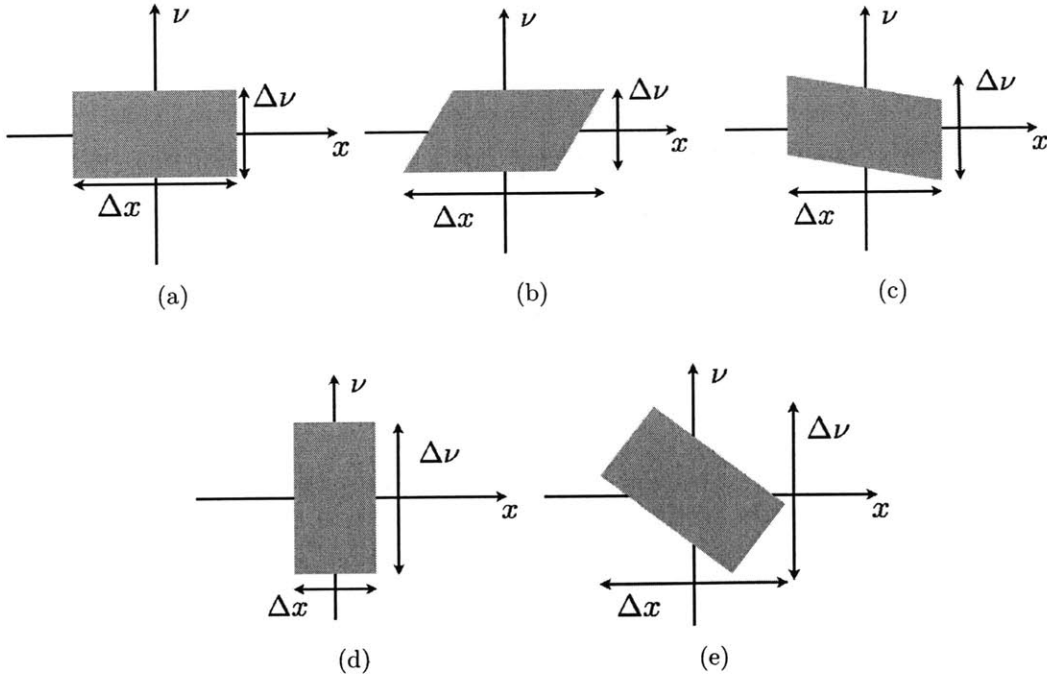


Figure 2-4: Space-bandwidth product of an optical signal after different optical transformations. (a) Original SBP; (b) Fresnel propagated SBP; (c) SBP after passage through a lens; (d) SBP after a Fourier transform; (e) SBP after a fractional Fourier transform.

where SBP_I is the SBP of the signal and SBP_H is the SBP of the system in phase-space. Note that in common optical systems, the system SBP has a rectangular shape with x and ν symmetry. So the minimum requirement of SBP_H is the regions indicated by Δx and $\Delta \nu$ in fig. 2-4. However, different shapes of system SBP can be obtained if a computational shaping of SBP_H is used. This leads to the area of the generalized sampling theorem [98, 99] and “super-resolution” [100] by phase-space filtering methods, which is outside the scope of this thesis.

Chapter 3

Holographic imaging in phase-space and its application to two-phase flows

The fundamental problem addressed by holography is that of recording, and later reconstructing, both the amplitude and the phase of an optical wave arriving from a coherently illuminated object [34]. So holographic imaging generally consists of two steps, recording and reconstruction.

In the recording step, a hologram is recorded as an interference pattern formed by combining a field scattered by a coherently illuminated object, with a field of illumination (termed reference wave). Although all recording media respond only to light intensity, the interferometric principle adopted in holographic recording step is able to store both the amplitude and phase information of the object wave. The schematic of interferometric recording is shown in Figure3-1.

The complex object can be written as

$$f(x, y) = |f(x, y)| \exp\{i\phi(x, y)\}, \quad (3.1)$$

and the complex reference wave is $r(x, y)$.

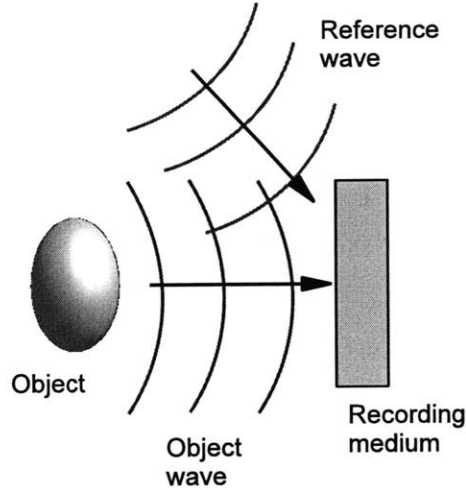


Figure 3-1: Interferometric recording.

The recorded intensity is given by

$$\begin{aligned}
 I(x, y) &= |f(x, y)|^2 + |r(x, y)|^2 + r^*(x, y)|f(x, y)| \exp\{i\phi(x, y)\} \\
 &\quad + r(x, y)|f(x, y)| \exp\{-i\phi(x, y)\} \\
 &= I_f + I_r + fr^* + f^*r.
 \end{aligned} \tag{3.2}$$

While the first two terms of this expression depend only on the intensities of the individual waves, the last two terms depend on the phase of the object wave, thus information about both the amplitude and phase of $f(x, y)$ has been recorded. In holography (i.e. as compared to general interferometry), we further require the amplitude of the reference wave is uniform.

In the reconstruction step, the hologram is illuminated by a coherent reconstruction wave $B(x, y)$. The wave, $R(x, y)$, transmitted past the hologram is

$$\begin{aligned}
 R(x, y) &= B(x, y)I(x, y) = BI_f + BI_r + fBr^* + f^*Br \\
 &= U_1 + U_2 + U_3 + U_4.
 \end{aligned} \tag{3.3}$$

If B is an exact duplicate of the original reference wave r , the third term of (3.3)

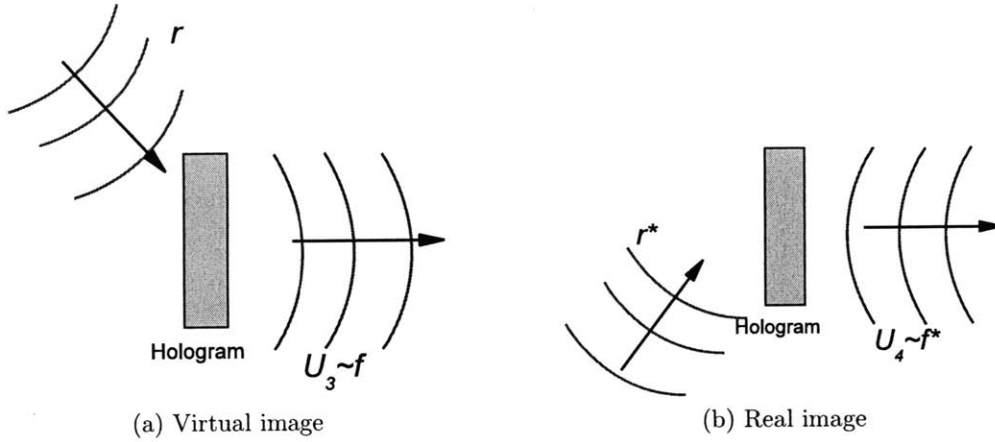


Figure 3-2: Wavefront reconstruction with (a) the original reference wave r as reconstruction illumination, and (b) the conjugate reference wave r^* as reconstruction illumination.

becomes

$$U_3 = |r|^2 f(x, y). \quad (3.4)$$

Since the intensity of the reference wave is uniform, U_3 is, up to a multiplicative constant, an exact duplication of the original wavefront $f(x, y)$. This is illustrated in Figure 3-2 (a).

In a similar fashion, if B is chosen as the conjugate of the original reference wave, i.e. as r^* , the fourth term becomes

$$U_4 = |r|^2 f^*(x, y). \quad (3.5)$$

which is proportional to the conjugate of the original wavefront $f^*(x, y)$. This is illustrated in Figure 3-2 (b).

In either case, the particular field component of interest is accompanied by three additional field components. By convention, U_1 is called the DC-term, U_2 is called the halo, and U_4 and U_3 are called the virtual image and the real image, U_4 is also referred to as U_3 's twin image, respectively.

3.1 Holography in phase-space

3.1.1 Holographic information in phase-space

In (3.3), we showed that a recorded hologram consists of four field components. We also showed that the information of the original object wave is recorded in U_3 (U_4) term. We shall start this section by revisiting these points by phase-space analysis.

In chapter 2, we showed that the WDF of a coherent superposition of two optical signals consist of four components

$$\mathcal{W}_{f+r}(x, u) = \mathcal{W}_f(x, u) + \mathcal{W}_r(x, u) + \mathcal{W}_{f,r}(x, u) + \mathcal{W}_{r,f}(x, u). \quad (3.6)$$

where f is complex object wave and r is the reference wave. One dimensional analysis is used here for simplicity, while extension to two dimensions is straightforward.

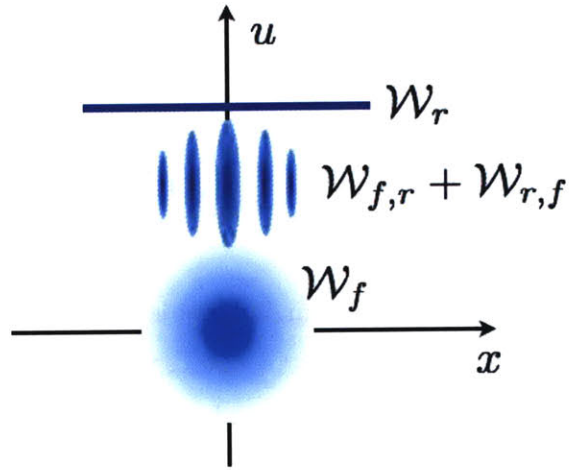
In order to find the connections between (3.6) and (3.3), we integrate (3.6) over spatial frequency u . From the projection property of the WDF, the projection equals to the intensity recorded on the hologram

$$\begin{aligned} I(x) &= \int \mathcal{W}_{f+r}(x, u) du \\ &= \int \mathcal{W}_f(x, u) du + \int \mathcal{W}_r(x, u) du + \int \mathcal{W}_{f,r}(x, u) du + \int \mathcal{W}_{r,f}(x, u) du \\ &= |f(x)|^2 + |r(x)|^2 + f(x)r^*(x) + f^*(x)r(x). \end{aligned} \quad (3.7)$$

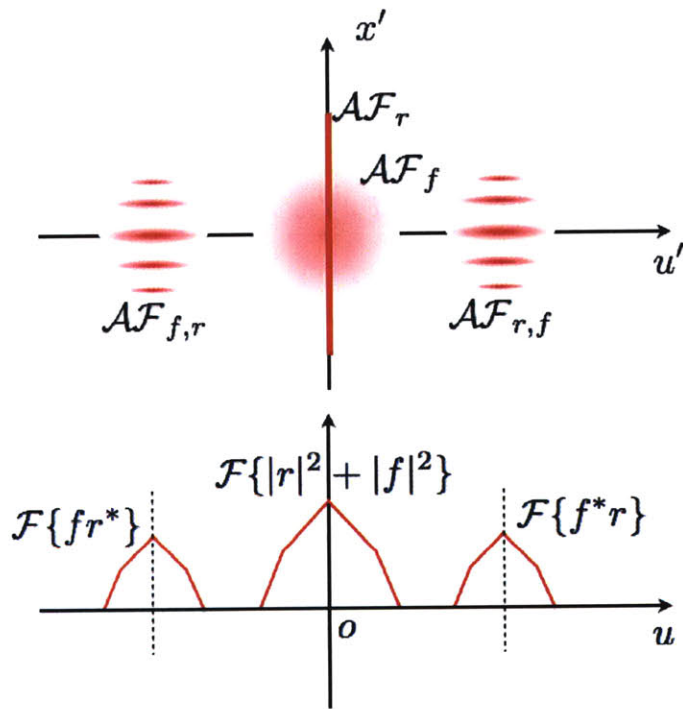
Note that the last two terms in (3.7) are exactly the real and virtual image terms in (3.3). So the holographic information in phase-space are in the strongly oscillating cross-terms [115]. This result is illustrated in Figure 3-3 (a). Notice that both $\mathcal{W}_{f,r}$ and $\mathcal{W}_{r,f}$ are in the midway between \mathcal{W}_r and \mathcal{W}_f in Wigner space. In fact, it is easy to see that

$$\mathcal{W}_{f,r} = \mathcal{W}_{r,f}^*. \quad (3.8)$$

Interestingly, the cross-terms were often considered undesirable, when the WDF was applied to time-frequency analysis in signal processing, and a number of algorithms were developed to reduce the cross-terms [75].



(a) Holographic information in the Wigner space.



(b) (top figure) Holographic information in the Ambiguity function space and (bottom figure) Fourier transform of the hologram, which is the slice of the AF at $x' = 0$.

Figure 3-3: Holographic information in phase-space.

It should also be pointed out that, up to now, we have assumed that all of the information in the object wave f are of interest in our analysis. However, in most of practical cases, the object wave f is also a combination of the waves scattered from multiple objects, for instance, multiple particles. In this case, f needs to be written as

$$f = \sum_n f_n. \quad (3.9)$$

The information of interest are individual object waves f_n , instead of their superposition f , in this case. Another type of cross-terms due to the interference between different object waves (termed cross-talks) are produced here. This type of cross-terms are usually undesirable in holographic signal processing [79].

Another insightful interpretation of holographic information is to analyze the coherent superposition of two signals in AF space [97]. Similar to the interference property of the WDF, the summation of two signals will also generate interference terms in AF

$$\mathcal{AF}_{f+r}(u', x') = \mathcal{AF}_f(u', x') + \mathcal{AF}_r(u', x') + \mathcal{AF}_{f,r}(u', x') + \mathcal{AF}_{r,f}(u', x'), \quad (3.10)$$

where

$$\mathcal{AF}_{f,r}(u', x') = \int f(x + x'/2)r^*(x - x'/2) \exp\{-i2\pi u'x\}dx. \quad (3.11)$$

It is informative to compute the cross-ambiguity function when the reference wave is a plane wave $r(x) = \exp\{i2\pi u_0x\}$.

$$\begin{aligned} \mathcal{AF}_{f,r}(u', x') &= \int f(x + x'/2) \exp\{-i2\pi u_0(x - x'/2)\} \exp\{-i2\pi u'x\}dx \\ &= \exp\{i2\pi(u'/2 + u_0)x'\}F(u' + u_0), \end{aligned} \quad (3.12)$$

$$\begin{aligned} \mathcal{AF}_{r,f}(u', x') &= \int f^*(x - x'/2) \exp\{i2\pi u_0(x + x'/2)\} \exp\{-i2\pi u'x\}dx \\ &= \exp\{-i2\pi(-u'/2 + u_0)x'\}F^*(u' - u_0). \end{aligned} \quad (3.13)$$

So the two cross-ambiguity function terms lie on two sides along u' -axis, as shown in the top figure of Figure 3-3 (b). It is easy to see that if we take a slice of the AF at

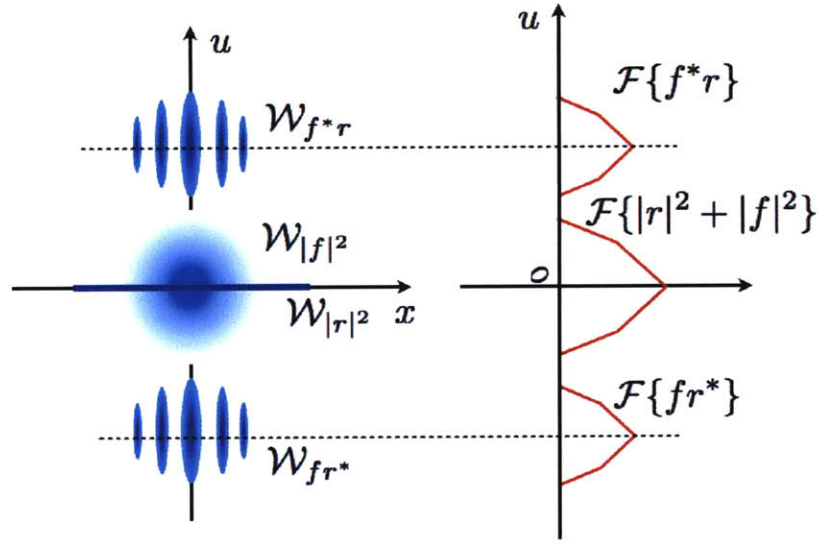


Figure 3-4: The WDF of a hologram.

$x' = 0$, we get the Fourier transforms of the four components in a hologram, as shown in the bottom figure of Figure 3-3 (b).

$$\mathcal{AF}_{f+r}(u', 0) = \mathcal{F}\{|f|^2\} + \mathcal{F}\{|r|^2\} + \mathcal{F}\{|f^*r|^2\} + \mathcal{F}\{|fr^*|^2\}. \quad (3.14)$$

Another useful observation is that, in general, the cross-Wigner terms appear in the middle of the WDFs of individual signals, as in Figure 3-3 (a); while the cross-ambiguity function terms lie on the “high frequency” part in AF space with the AFs of individual signals in the central part, as in Figure 3-3 (b). So, a number of AF based filtering methods have been developed according to this idea [77]. In fact, all Cohen’s class distribution functions can be understood in this way; filters are called kernels in Cohen’s notes [14].

Finally, to find the dual representation of (3.14), we shall look at the WDF of a hologram.

$$\mathcal{W}_I(x, u) = \mathcal{W}_{|f|^2}(x, u) + \mathcal{W}_{|r|^2}(x, u) + \mathcal{W}_{f^*r}(x, u) + \mathcal{W}_{fr^*}(x, u). \quad (3.15)$$

Compute the WDF of the last two terms by assuming the reference wave is a plane wave $r(x) = \exp\{i2\pi u_0 x\}$.

$$\mathcal{W}_{fr^*}(x, u) = \mathcal{W}_f(x, u) *_u \mathcal{W}_{r^*}(x, u) = \mathcal{W}_f(x, u + u_0) \quad (3.16)$$

$$\mathcal{W}_{f^*r}(x, u) = \mathcal{W}_{f^*}(x, u) *_u \mathcal{W}_r(x, u) = \mathcal{W}_f^*(x, u - u_0) \quad (3.17)$$

So the WDF of real (f^*) and virtual (f) image terms lie on two sides along u -axis, as shown in the left figure of Figure 3-4. By the projection property of the WDF, we get the Fourier transforms of the four components in a hologram by integrating the WDF over its spatial frequency u , as shown in the right figure of Figure 3-4.

3.1.2 Space-bandwidth transfer in different holographic imaging system setups

As pointed out previously, SBP is fundamental for judging the performance of an optical system. And phase-space analysis is useful to understand how the space-bandwidth shape evolves as an optical signal is transformed by an optical system [53, 54] and the space-bandwidth conditions for information recording [104].

The most commonly used holographic imaging system setups are in-line holography, invented by D. Gabor in 1948 [31], and off-axis holography, invented by E. N. Leith and Upatniek [43] in 1962. We will analyze these two setups in the following.

In-line holography

In in-line holography setup, both the reference wave and the object wave are collinear and normal to the recording medium, as shown in Figure 3-5. The object is assumed to be highly transmissive. With such an object being coherently illuminated by the collimated wave shown in Figure 3-5, the transmitted light consists of two components: (1) a strong uniform plane wave as reference wave and (2) a weak scattered wave as object wave.

By proper normalization, the reference wave can be written as $r(x) = 1$, and

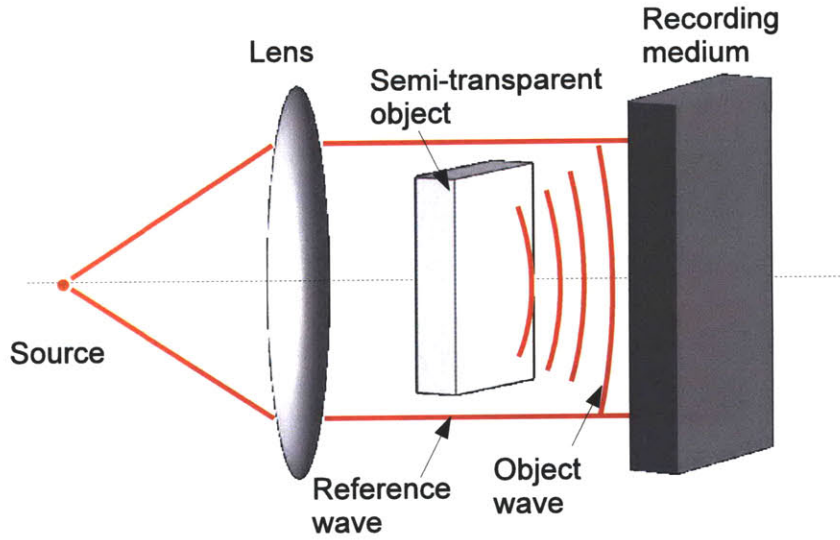


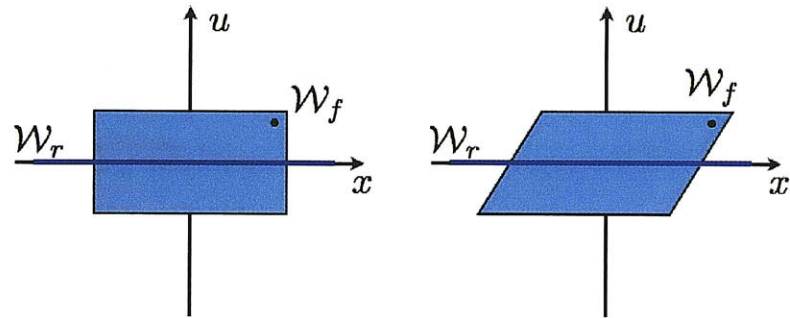
Figure 3-5: In-line holography setup.

assume the object wave is $f(x)$. The intensity recorded on the hologram is

$$\begin{aligned}
 I(x) &= |1 + f(x)|^2 \\
 &= 1 + |f(x)|^2 + f(x) + f^*(x).
 \end{aligned} \tag{3.18}$$

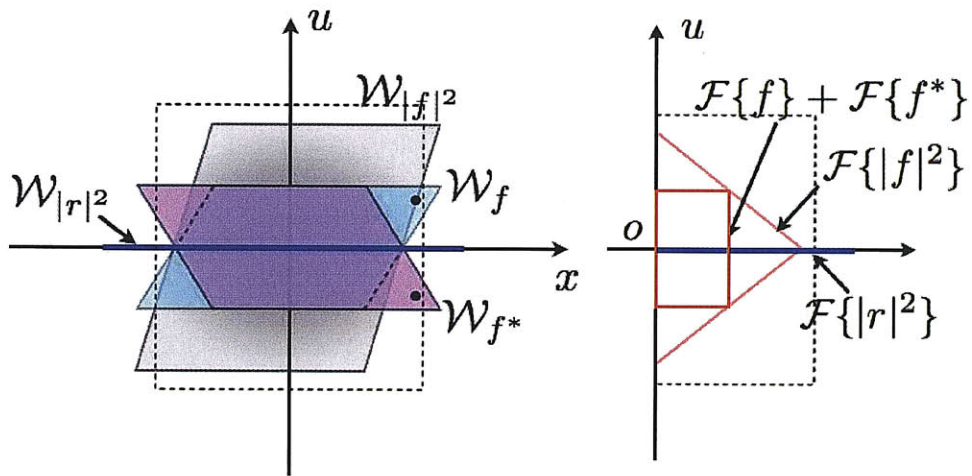
The formation of an in-line hologram is analyzed in Wigner space, as shown in Figure 3-6 (a-c). First, the object is illuminated by an on-axis plane wave. Assume the significant information content of an object signal is contained within a rectangular region \mathcal{W}_f in Wigner space, and the on-axis plane reference wave is a $\delta(u)$ -function \mathcal{W}_r in Wigner space, as shown in Figure 3-6 (a). Next, the object wave propagates a distance to the recording medium plane. This corresponds to, within the paraxial approximation, a x -shear in the Wigner space, as shown in Figure 3-6 (b). Finally, the intensity of the interference pattern is recorded by the recording medium with a known SBP (dotted rectangle), as shown in Figure 3-6 (c). By integrating the WDF of the hologram (in Figure 3-6 (c)), we can get the Fourier transform of the hologram, as shown in Figure 3-6 (d). The dotted line shows the Nyquist frequency cutoff of the recording medium.

As seen in both 3-6 (c) and (d), a limitation of in-line holography lies in the



(a) SBP at the object plane

(b) SBP at the detector plane



(c) SBP of an in-line hologram

(d) Fourier spectrum of an in-line hologram

Figure 3-6: The space-bandwidth transfer (a-c) and the Fourier spectrum (d) of in-line holography.

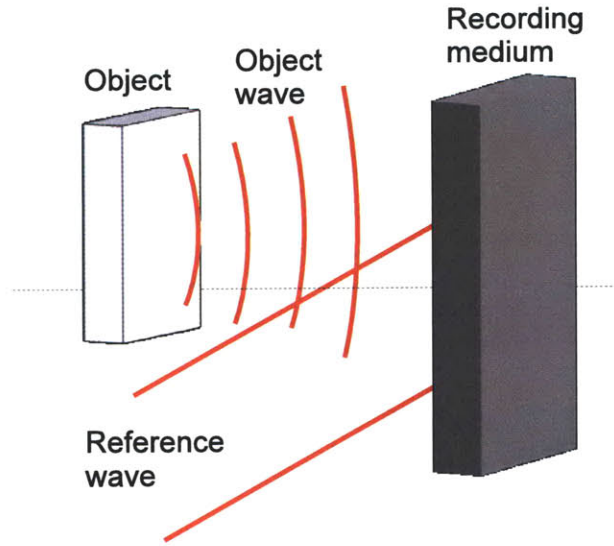


Figure 3-7: Off-axis holography setup.

generation of overlapping twin images. A number of methods have been proposed for eliminating or reducing the twin-image problem, including off-axis setup and phase-shifting method [117].

Off-axis holography

In off-axis holography, a separate and tilted reference wave are introduced to interfere with the object wave, as shown in Figure 3-7.

By proper normalization, the reference wave can be written as $r(x) = \exp\{i2\pi u_0 x\}$. Let the object wave be denoted as $f(x)$. The intensity recorded as the hologram is

$$\begin{aligned} I(x) &= |r(x) + f(x)|^2 \\ &= 1 + |f(x)|^2 + f(x) \exp\{-i2\pi u_0 x\} + f^*(x) \exp\{i2\pi u_0 x\}. \end{aligned} \quad (3.19)$$

Again, the formation of an off-axis hologram is analyzed in Wigner space, as shown in Figure 3-8 (a-c). First, the object is illuminated by an off-axis plane wave. Assume the significant information content of an object signal is contained within a rectangular region \mathcal{W}_f in Wigner space, and the off-axis plane reference wave is a $\delta(u - u_0)$ -function \mathcal{W}_r in Wigner space, as shown in Figure 3-8 (a). Next, the

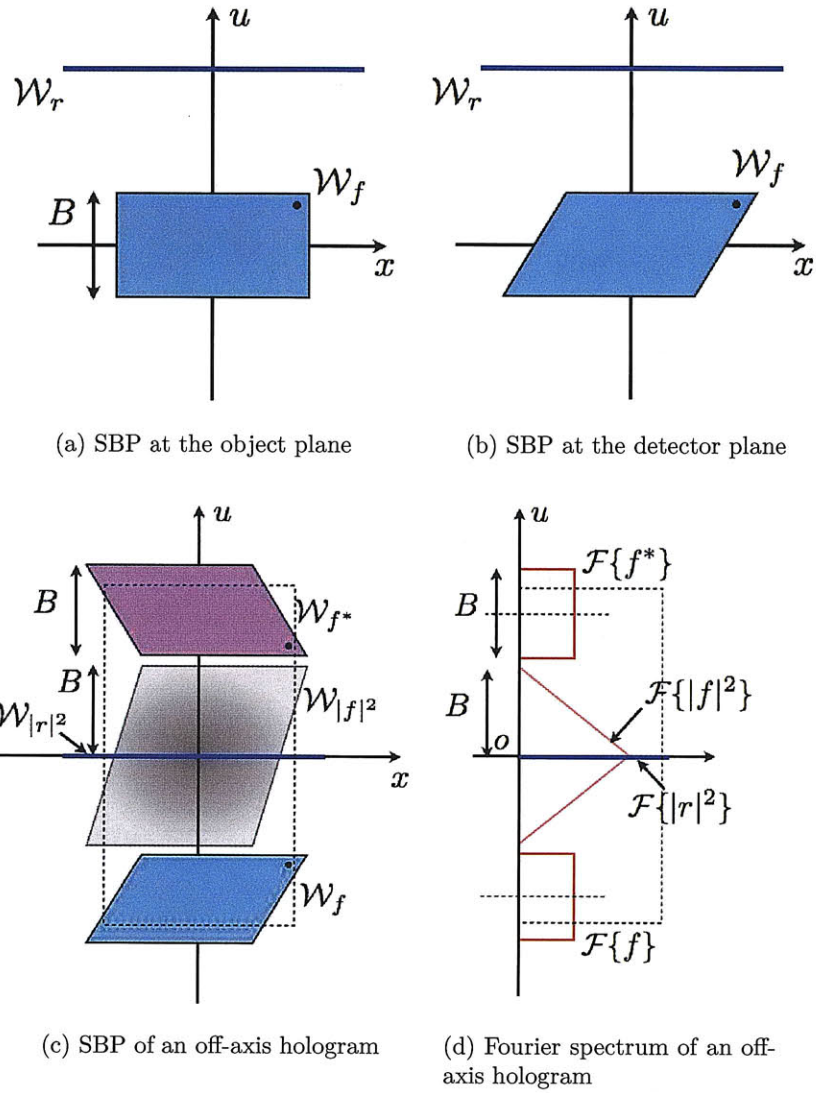


Figure 3-8: The space-bandwidth transfer (a-c) and the Fourier spectrum (d) of off-axis holography.

object wave propagates a distance to the recording medium plane. This corresponds to, within the paraxial approximation, an x -shear in the Wigner space, as shown in Figure 3-8 (b). Finally, the intensity of the interference pattern is recorded by the recording medium with a known SBP (dotted rectangle), as shown in Figure 3-6 (c). The SBPs of the real and virtual images are separated along u -axis by properly chosen tilting angle. By integrating the WDF of the hologram (in Figure 3-8 (c)), we can obtain the Fourier transform of the hologram, as shown in Figure 3-8 (d), and the dotted box shows the Nyquist frequency cutoff of the recording medium.

As seen from both 3-8 (c) and (d), the minimum reference angle required to separate the twin images is

$$u_0^{(min)} = 1.5B \quad (3.20)$$

where B is bandwidth of the optical signal. So the bandwidth requirement for the recording medium of off-axis holography is 4 times of the requirement of in-line holography. In terms of pixel size, off-axis holography requires 4 times smaller pixel size than the one for in-line holography. This limits the use of off-axis holography in a number of applications, especially in digital holography, where the production of the digital sensor, e.g. CCD and CMOS, with pixel size smaller than $1\mu m$ is hard to achieve with current technology.

Space-bandwidth transfer in hologram reconstruction

Once the information is recorded on a hologram, a reconstruction step is carried out to retrieve the object. The process of reconstruction is analyzed in Wigner space as shown in Figure 3-9. First, the recorded information is bounded by the detector's SBP, as shown in the shaded area in Figure 3-9(a). Next, the reconstruction wave propagates a distance to the object plane. This corresponds to, within the paraxial approximation, a x -shear in the Wigner space with the direction opposite to the one in the recording step, as shown in Figure 3-9 (b). Finally, if we assume the object has unknown complex-valued content, then both the positive and negative spatial-frequencies are needed to unambiguously recover the signal. The SBP which fulfills

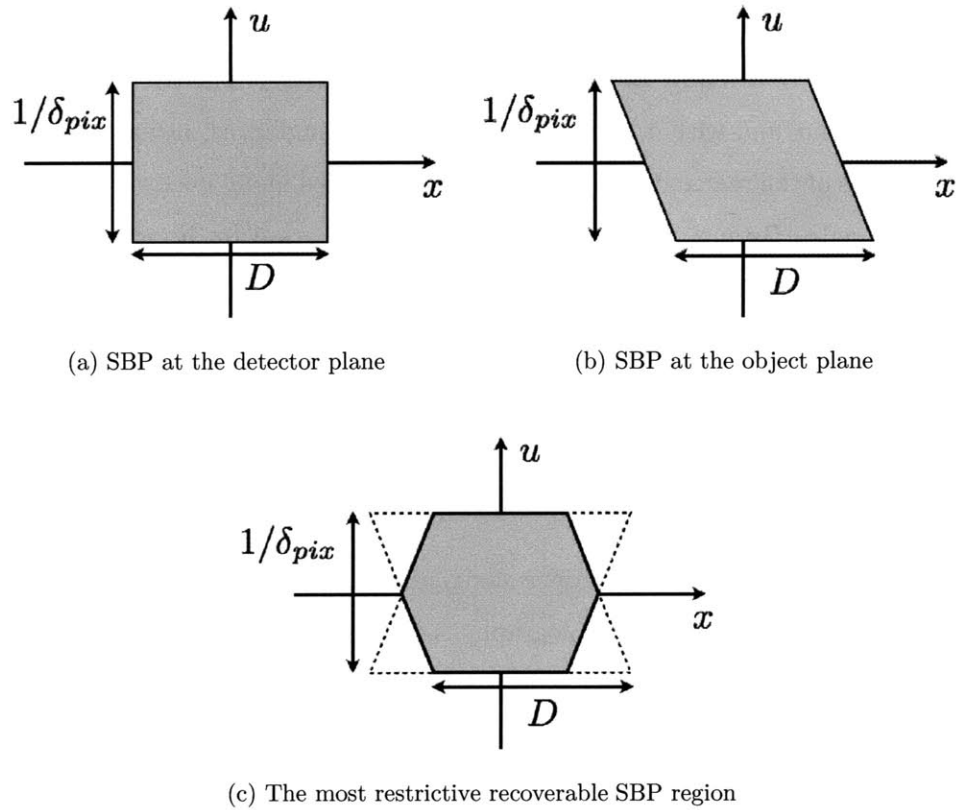


Figure 3-9: Space-bandwidth transfer in hologram reconstruction.

this requirement, the intersection of the detector and its conjugate SBPs, is shown in Figure 3-9 (c).

Note that the analysis carried out here assumes that the Nyquist frequency sets the limits in the spatial frequency of the detector's SBP. It has been pointed out in the literature that, by fulfilling certain criteria, some of the information that inside the space limit ($|x| < D/2$), but outside the Nyquist limit ($|u| > 1/(2\delta_{pix})$) can still be recovered [35, 71, 100].

3.2 Digital holographic recording and reconstruction

Conventionally, holography was recorded on a photographic film or plate. Digital holography (DH) and digital holographic image processing [94] have recently become feasible due to advances in megapixel electronic sensors, e.g. CCD and CMOS, with high spatial resolution and high dynamic range. DH, compared to conventional holography, does not have the cumbersome requirement of film positioning, handling, and processing, and has the additional advantage of making the information readily available in digital form for post-processing [93, 95]. Holography is well known for being able to record and reconstruct, in a single shot, information about the history of the field propagation within an entire 3D volume of interest. In addition, the fusion between optics and computational power makes DH an extremely powerful tool. It has been used increasingly in a broad spectrum of 3D imaging applications, such as flow diagnostics [39], e.g. holographic particle imaging velocimetry (PIV) [19, 80, 87], aquatic bio-imaging [20, 60], holographic microscopy [11, 62], and 3D object recognition [37].

Due to high space-bandwidth requirement of off-axis holography and relative low space-bandwidth support of digital sensors, the in-line holography setup is widely adopted in most of DH setups. In addition to the low space-bandwidth requirement, in-line holography also has a simple optical setup because the illumination and the reference beam share the same optics. Furthermore, digital processing makes it possible to computationally reduce the twin image in an in-line hologram, and several iterative methods have been proposed [23, 42].

3.2.1 Digital holography recording

Figure 3-10 shows an in-line holography configuration. The illumination is produced by a laser. The input beam is expanded by a spatial filter, and is collimated by a plano-convex lens. After propagating through the sample volume, the resultant

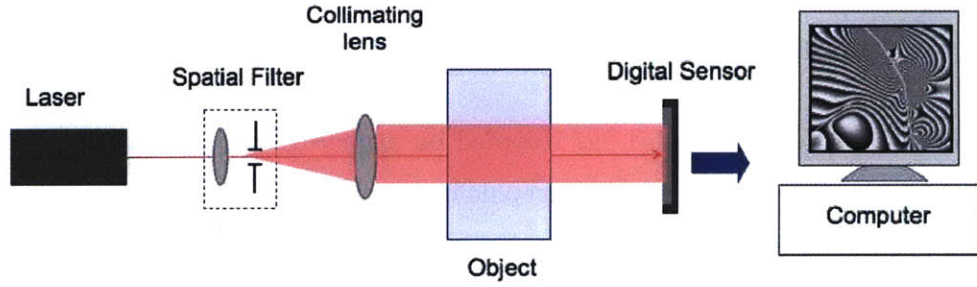


Figure 3-10: Digital in-line holography setup.

hologram is recorded by a digital sensor. The digital sensor provides a linear mapping of intensity incident during the integration time into the pixel value.

Assume the reference wave is

$$r(x, y) = A_r, \quad (3.21)$$

and the complex amplitude of the object wave is

$$o(x, y) = A_o(x, y) \exp\{-i\phi(x, y)\} \quad (3.22)$$

where A_o is the amplitude and ϕ is the phase. The recorded intensity is

$$I = A_r^2 + A_o(x, y)^2 + A_r o(x, y) + A_r o^*(x, y). \quad (3.23)$$

3.2.2 Digital reconstruction

Recall that in conventional holography, the reconstruction is achieved by illuminating the hologram by a spatially coherent reconstruction wave, which could be either the original reference wave or the conjugate of the original reference wave. The basic task of digital reconstruction is to digitally emulate the optical reconstruction process.

First, in in-line holography case, illuminating the hologram by a plane wave is equivalent to multiplying the hologram by a constant scaling factor, which can be

taken as unity. So we take the field at the hologram plane to be equal to the the intensity recorded on the hologram, determined by (3.23).

Second, the third (or fourth) term in (3.23) is the complex amplitude of the object wave propagated from the object plane to the hologram plane. In order to reconstruct the original object, we need to propagate it back to the original object plane. So we will discuss free space propagation in the following.

Shift-invariance and reconstruction kernel

The free space propagation is described by the Huygens-Fresnel theory of diffraction [34]. The propagated optical field at a particular image plane, a distance z from the original plane, is given by

$$E(x', y'; z) = \frac{1}{i\lambda} \iint I(x, y) \frac{\exp(ikr)}{r} \cos \theta dx dy, \quad (3.24)$$

where λ is the wavelength and k is the wave number given by $k = 2\pi/\lambda$. The variable r is the distance between a point in the original plane and a point in the image plane

$$r = \sqrt{(x - x')^2 + (y - y')^2 + z^2}, \quad (3.25)$$

and the obliquity factor $\cos \theta$ is given by

$$\cos \theta = \frac{z}{r}. \quad (3.26)$$

Substituting (3.25) and (3.26) into (3.24), we get

$$E(x', y'; z) = \frac{z}{i\lambda} \iint I(x, y) \frac{\exp(ik\sqrt{(x' - x)^2 + (y' - y)^2 + z^2})}{(x - x')^2 + (y - y')^2 + z^2} dx dy, \quad (3.27)$$

This result has the form of a two-dimensional (2D) linear convolution and may be written as

$$\begin{aligned} E(x', y'; z) &= \iint I(x, y) h_e(x' - x, y' - y; z) dx dy \\ &= \{I(x, y) ** h_e(x, y; z)\}|_{x=x', y=y'}, \end{aligned} \quad (3.28)$$

where ** indicates 2D linear convolution, and

$$h_e(x, y; z) = \frac{z}{i\lambda} \frac{\exp(ik\sqrt{x^2 + y^2 + z^2})}{x^2 + y^2 + z^2} \quad (3.29)$$

is the exact diffraction kernel for a distance z . The kernel is also called the Point Spread function (PSF) or the impulse response of the optical system. Its Fourier transform is

$$H(u, v; z) = \exp\left\{i2\pi\frac{z}{\lambda}\sqrt{1 - (\lambda u)^2 - (\lambda v)^2}\right\}, \quad \sqrt{u^2 + v^2} < 1/\lambda. \quad (3.30)$$

Further simplification can be achieved by adopting the paraxial or Fresnel approximation. This approximation is valid if the lateral displacements $|x - x'|$ and $|y - y'|$ are much smaller than the axial distance z . Expanding r by its Taylor series, we get

$$r = z + \frac{(x - x')^2}{2z} + \frac{(y - y')^2}{2z} - \frac{1}{8} \frac{[(x - x')^2 + (y - y')^2]^2}{z^3} + \dots \quad (3.31)$$

and neglecting the higher order terms,

$$r \approx z + \frac{(x - x')^2}{2z} + \frac{(y - y')^2}{2z}. \quad (3.32)$$

Substituting (3.32) into (3.24), we get the paraxial-approximated diffraction integral

$$E(x', y'; z) = \frac{\exp(ikz)}{i\lambda z} \iint I(x, y) \exp\left\{\frac{i\pi}{\lambda z}[(x' - x)^2 + (y' - y)^2]\right\} dx dy. \quad (3.33)$$

Equation (3.33) also can be expressed as a 2D linear convolution,

$$\begin{aligned} E(x', y'; z) &= \iint I(x, y) h_f(x' - x, y' - y; z) dx dy \\ &= \{I(x, y) ** h_f(x, y; z)\}|_{x=x', y=y'}, \end{aligned} \quad (3.34)$$

where

$$h_f(x, y; z) = \frac{\exp(ikz)}{i\lambda z} \exp\left\{\frac{i\pi}{\lambda z}(x^2 + y^2)\right\} \quad (3.35)$$

known as Fresnel diffraction kernel. It is a 2D chirp function. The Fourier transform of this kernel is also a 2D chirp function

$$H_f(u, v; z) = \exp(ikz) \exp\{i\pi\lambda z(u^2 + v^2)\}. \quad (3.36)$$

Both (3.28) and (3.34) show that free space propagation acts as a linear space invariant system and can be characterized by a transfer function.

In the non-paraxial regime, the transfer function is given by (3.30). Assume that the Fourier spectrum of the field at an arbitrary plane $E(x, y; z)$ is $U(u, v; z)$, so the field can be decomposed into plane waves as

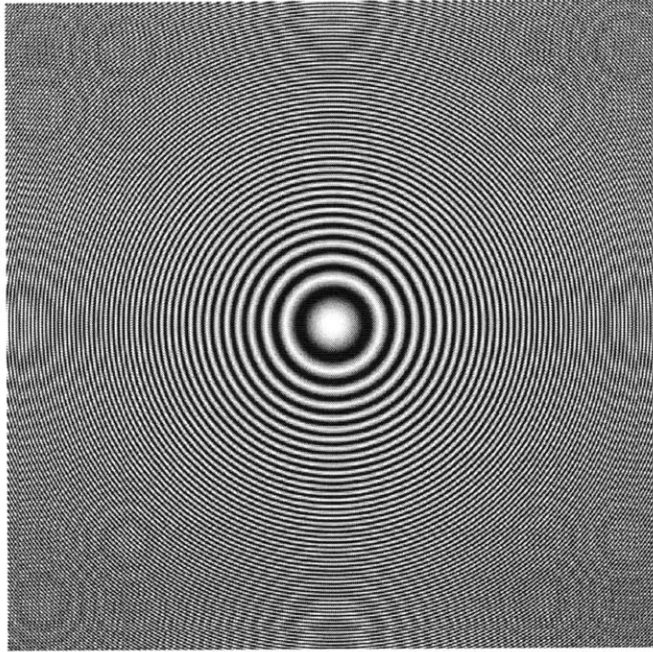
$$E(x, y; z) = \iint U(u, v; z) \exp\{i2\pi(ux + vy)\} dudv, \quad (3.37)$$

which is known as the angular spectrum of this field. So we can rewrite (3.28) in the angular spectrum domain using the transfer function, and then transform it back to the space domain

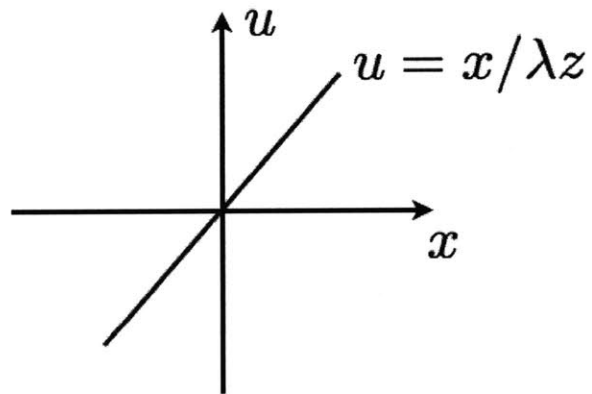
$$\begin{aligned} E(x, y; z) &= \iint U(u, v; 0) \exp\left\{i2\pi\frac{z}{\lambda}\sqrt{1 - (\lambda u)^2 - (\lambda v)^2}\right\} \\ &\quad \text{circ}(\lambda\sqrt{u^2 + v^2}) \exp\{i2\pi(ux + vy)\} dudv. \end{aligned} \quad (3.38)$$

Result (3.38) is known as the propagation of angular spectrum.

In the paraxial regime, the transfer function is given by (3.36). Similarly, we can



(a) 2D Fresnel diffraction kernel in space domain



(b) 1D Fresnel diffraction kernel in the Wigner space is a line with its slope inversely proportional to z

Figure 3-11: Fresnel diffraction kernel

get the propagation formula

$$E(x, y; z) = \exp(ikz) \iint U(u, v; 0) \exp \{i\pi\lambda z(u^2 + v^2)\} \exp\{i2\pi(ux + vy)\} dudv. \quad (3.39)$$

which is known as Fresnel propagation. We will restrict our discussion to the paraxial regime. A detailed discussion about the accuracy of Fresnel propagation as compared to the angular spectrum can be found in [34].

The Fresnel diffraction kernel in space domain is shown in Figure 3-11(a). The linear system theory applied before can be extended to the phase-space [68]. Taking 1D case for simplicity, the shift invariant system can be expressed as

$$E_2(x_2) = \int h(x_1 - x_2)E_1(x_1)dx_1. \quad (3.40)$$

By applying the WDF to both sides of (3.40), the input-output relation in the Wigner space is expressed as

$$\mathcal{W}_2(x_2, u_2) = \int \mathcal{W}_s(x_2 - x_1, u_2)\mathcal{W}_1(x_1, u_2)dx_1, \quad (3.41)$$

where

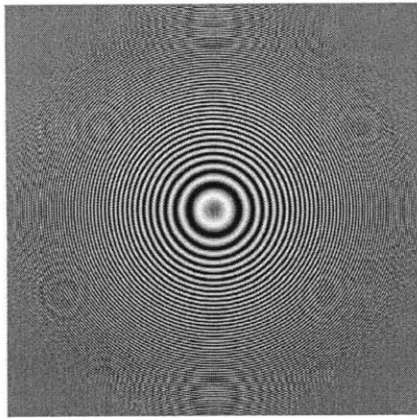
$$\mathcal{W}_s(x, u) = \int h(x + x'/2)h^*(x - x'/2) \exp\{-i2\pi ux'\}dx' \quad (3.42)$$

is the convolution kernel or impulse response in the Wigner space. In paraxial regime, this kernel can be computed by substituting (3.35) into (3.42), by neglecting the constant scaling terms, as

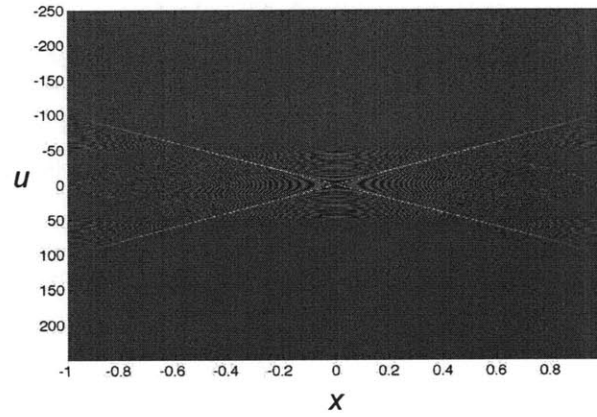
$$\mathcal{W}_s(x, u) = \delta(u - x/\lambda z). \quad (3.43)$$

The paraxial approximated kernel in the Wigner space is shown in Figure 3-11(b). It is a line whose slope is inversely proportional to the propagation distance z . For the non-paraxial case, readers may refer to [114].

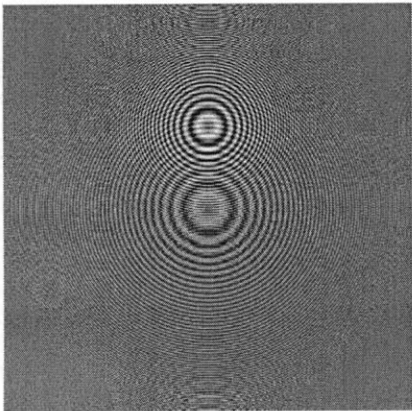
The paraxial Wigner space kernel can be applied to analyze Fresnel holograms.



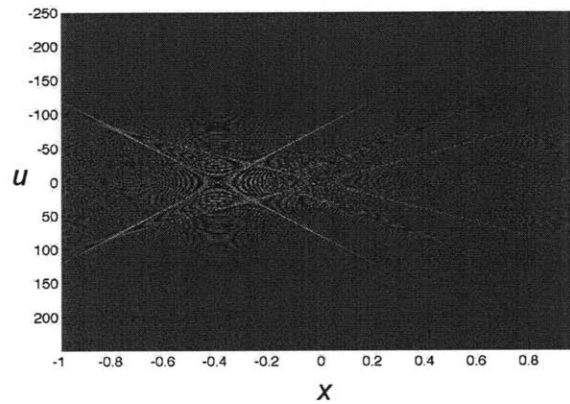
(a) Hologram of a single point source



(b) The WDF of the central vertical line in (a)



(c) Hologram of two point sources locating at different lateral and axial positions



(d) The WDF of the central vertical line in (c)

Figure 3-12: Point source holograms and their WDFs.

Examples are given in Figure 3-12. Figure 3-12(a) shows a hologram of a single point source. Analysis in the Wigner space can be carried out by taking the central vertical line of data and applying the WDF to it, as the results shown in Figure 3-12(b). Figure 3-12(c) shows a hologram of two point sources locating at different lateral and axial positions. Again, analysis in the Wigner space is carried out by taking the central vertical line of data and applying the WDF to it, as the results shown in Figure 3-12(d). The major feature of the WDF shown in Figure 3-12(b) and (d) is that there is an “X” shape with its center at the lateral position where the point source is located. This can be explained by considering that both the object wave and the conjugate object wave are recorded on the hologram

$$I \sim f + f^*. \quad (3.44)$$

For the point source case, the WDF consists of two lines with opposite slopes intersecting in the horizontal axis at the position where the point source is located. So the slopes of the two lines of the “X” shape are related to the axial position of the point source by (3.43). This technique can be applied to locate point objects [72] and separate chirp functions [78]. One limitation is the interference terms in the WDF, which are evident in Figure 3-12(d). One solution is to apply filtering in the phase space [79]. Interference terms are in the high frequency region in the Ambiguity space, thus low-pass filter can be applied to reduce them.

Similarly, we can apply the AF to both sides of (3.40); the input-output relation in the Ambiguity space is then expressed as

$$\mathcal{AF}_2(u'_2, x'_2) = \int \mathcal{AF}_s(u'_2, x'_2 - x'_1) \mathcal{W}_1(u'_2, x'_1) dx'_1, \quad (3.45)$$

where

$$\mathcal{AF}_s(u', x') = \int h(x + x'/2) h^*(x - x'/2) \exp\{-i2\pi u'x\} dx \quad (3.46)$$

is the convolution kernel or impulse response in the Ambiguity space.

Solution uniqueness and focus metrics

The inverse source problem of holography [85] is to find the full complex amplitude distribution of the original 3D object. It is well known that the solution to this problem by a single intensity measurement is not unique [8, 28, 86, 112]. However, a unique solution can be obtained by posing constraints using *priori* information. In particular, in digital holography reconstruction, a number of “focus metrics” have been developed. Applying these focus metrics to the digitally reconstructed images, “in-focus” features can be recognized.

In general, the focus metrics are based on four types of *priori* information, including optical property, shape, in-focus criteria of human vision perception and phase-space pattern recognitions. For instance, the optical properties can be that the object is pure amplitude, or pure phase [22, 48, 80]. In addition, if the objects have fixed size and shape, as for example in Holographic PIV case, where the tracer particles are all spherical with fixed size, then a template matching scheme based on cross-correlation metric [19, 118] can be used. Furthermore, commonly used in-focus criteria in imaging processing based on human vision perception can be applied, including intensity based metric [91, 105], edge sharpness metric [18, 20, 102] and local pixel-value statistics metric [33, 55, 57]. Finally, several phase-space focus metrics have been developed. For example, [72] uses the signature of the chirp function in the Wigner space to detect point scatters, and [41] uses a phase-space cross-correlation metric.

3.3 Digital holography applied to two-phase flows

In this section, an in-line DH system is applied to study two types of two-phase flows. The first type is air-in-water mixture flows. In the experiment, a DC motor drives a small propeller in a water tank to generate air bubbles, which is a typical cavitation phenomenon. The second type is oil-in-water mixture flows. The flows were generated by stirring at the oil-water interface. The holograms were taken after the stirring and the oil-water separation process was recorded.

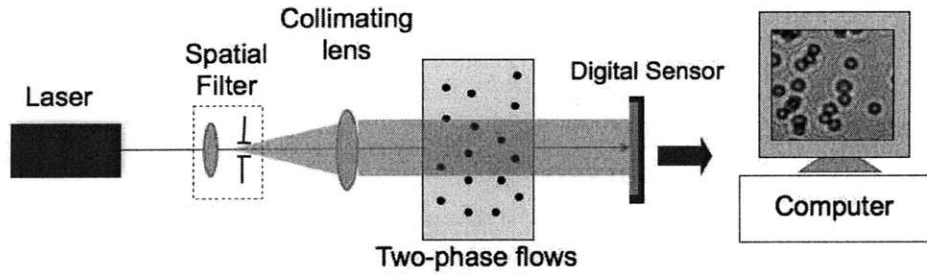


Figure 3-13: Digital in-line holography setup.

The system configuration is shown in Figure 3-13. The dimensions of the tank are $100 \times 100 \times 100\text{mm}^3$ and the central area with a diameter of 36mm is illuminated. In the air-in-water experiment, the illumination was produced by a diode laser with wavelength of 658nm. In the oil-in-water experiment, a HeNe laser with wavelength of 632.8nm was used. The input beam was expanded by a spatial filter, and was collimated by a plano-convex lens. After propagating through the sample volume, the resultant hologram was recorded by a large space-bandwidth product CCD sensor. In the air-in-water experiment, the sensor was a Kodak KAF16801E CCD with 4096×4096 pixels and $9\mu\text{m}$ pixel pitch.

In the oil-in-water experiment, a Basler A504 CMOS, with 1024×1024 pixels and $12\mu\text{m}$ pixel size, was used. One of the caveat of the CMOS sensor is that it has a sensor protection glass cover, which is not perfectly flat, and it produces large diffraction fringe overlapping with the entire hologram. We developed an automated data analysis algorithm which is robust to this type of noise without having to introduce an extra background noise reduction step.

The bubbles/oil-droplets are sparsely distributed through the water and their density is not high enough to corrupt the collimated beam. Thus the two-phase flows satisfy the assumption of weakly scattering object that is appropriate for in-line holography. The same beam serves both to illuminate the bubbles/oil-droplets and as a reference beam. Each bubble/oil-droplet acts like a point scatterer, which generates the object wave. The hologram is the result of interference between the undisturbed beam and light scattered by the bubbles/oil-droplets. Figure 3-14 shows

sample holograms of the air-in-water two phase flows (a) and the oil-in-water two-phase flows (b).

3.3.1 Automated data analysis

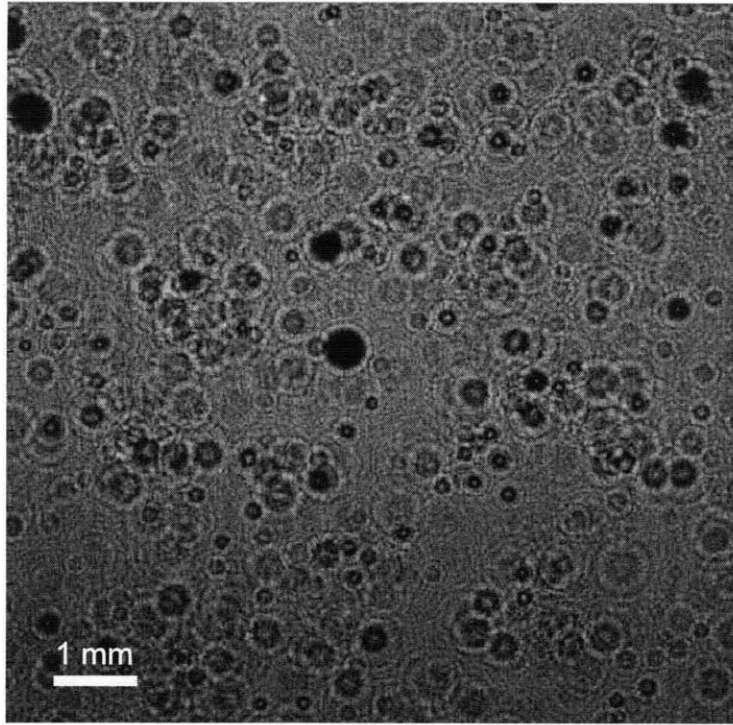
An automated data analysis algorithm is essential for quantitative measurement of two-phase flows due to the large amount of bubbles/oil-droplets to be measured. In general, there are four essential parts of analyzing this type of digital holograms: digital reconstruction, focus analysis, feature segmentation, and information extraction. In the rest of this section we describe each one of these sub-tasks as it applies to our system.

Digital reconstruction

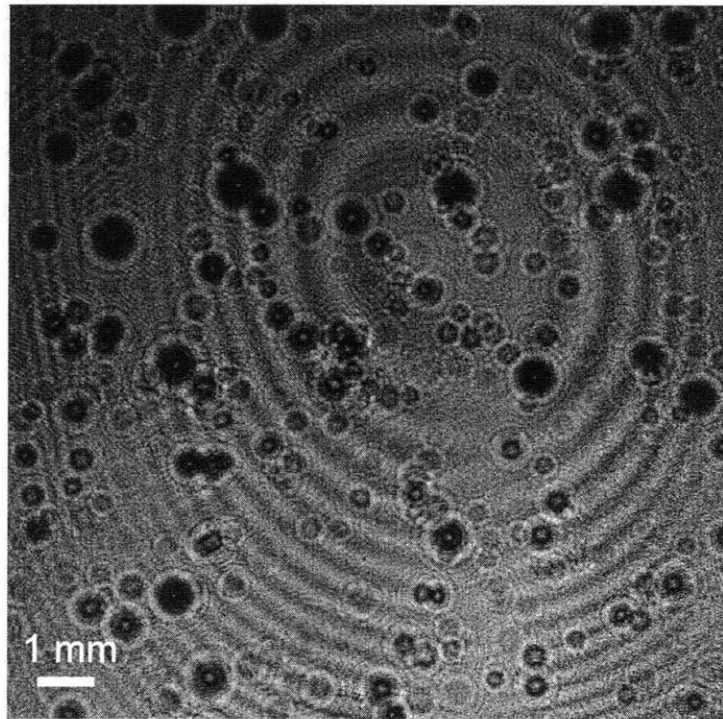
The captured holograms are reconstructed using the convolution method based on the Fresnel approximated transfer function as discussed in section 3.2.2. Instead of doing direct convolution, the reconstruction algorithm is implemented based on the Fast Fourier Transform (FFT), which speeds up the reconstruction. First, the Fourier transform of a hologram is multiplied by the Fresnel transfer function at a given axial distance z to find the spectral components at this axial distance z from the sensor plane. Then, an inverse Fourier transform is applied to reconstruct the object field in spatial domain from the computed spectra. Figure 3-15 shows a schematic diagram of the digital reconstruction algorithm. By changing the axial distance variable z in the Fresnel transfer function, it is possible to digitally reconstruct any plane within the volume of interest.

Focus analysis and feature segmentation

In general, feature segmentation algorithms can be applied to either 3D [60] or 2D reconstruction data [91, 118]. In the 3D case, the digital reconstruction algorithm is first applied to the hologram at every plane within the volume of interest. The resulting 3D reconstruction array stores all the reconstruction planes inside the volume



(a) A sample hologram of air-in-water two-phase flows



(b) A sample hologram of oil-in-water two-phase flows

Figure 3-14: Sample holograms of the studied two-phase flows.

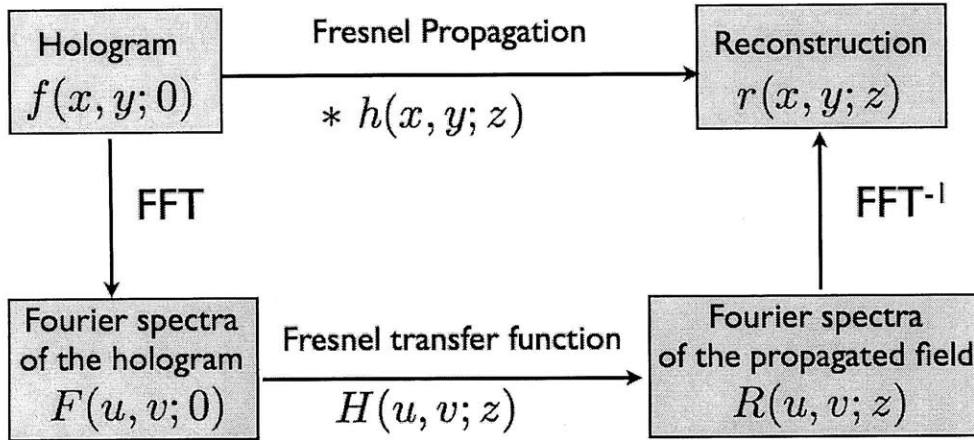


Figure 3-15: Schematic diagram of the digital reconstruction algorithm.

of interest with each plane having both in- and out-of-focus information, and subsequent analysis is carried out on this 3D matrix. For example, in [91], segmentation is achieved by looking for the local minimum intensity in this 3D array. In [118], a template matching scheme based on cross-correlation is used to segment particles in the 3D reconstruction data. In general, other different focus metrics [22, 33, 48, 55, 57, 80] can be used to segment the object of interest within the reconstructed 3D matrix.

On the other hand, 2D analysis techniques try to minimize the size of the reconstruction data. By using *priori* information, it is possible to find a 2D representation without doing the entire 3D reconstruction. For example, [13] uses a template matching scheme which is directly applied to the hologram. The interference pattern is fit to a template based on Lorenz-Mie theory to obtain of the particle's position, size and the refractive index. Another way to realize 2D analysis is to compress the 3D reconstruction data by throwing out redundant out-of-focus information. For example, [60] uses an axially projected Fresnel transfer function which simultaneously reconstructs all the planes within the volume of interest and axially sums the reconstructions to form a projected 2D reconstruction image. The resulting 2D projection image is thresholded to segment each of the object of interest (plankton in that work). This approach is only suitable for segmenting sparse objects. Similar 2D projections can also be produced by applying focus metrics at every reconstruction plane. As

expected, algorithms based on 2D segmentation usually require much less memory and can be much more computationally efficient in some applications.

In the two-phase flow experiments, a multi-step algorithm with a 2D segmentation step is implemented. This algorithm is designed for analyzing two-phase flows with moderate bubble density, but the general routine may also be applicable to other cases, such as holographic PIV and plankton imaging. In the first step, successive planes are reconstructed and the minimum intensity value at each pixel is recorded. This produces a 2D projection of the minimum intensity. At the same time, the axial position of where the minimum intensity occurred is recorded, creating a corresponding depth map. Figure 3-16 shows an example of how this method works for a bubble located 17.5mm from the hologram plane. Pixels a, b and c are edge pixels which reach a minimum intensity at the focal plane. An interior pixel, d, does not reach a minimum due to the formation of caustics. An example of the projected minimum intensity image and the corresponding depth map are shown in Figure 3-17(a) and (b), respectively.

The second step of the algorithm uses the intensity information to locate bubbles. The projected minimum intensity image is thresholded to create a map of bubble edges. Morphological operators are used to re-connect nearby regions through a dilation and an erosion. An example is depicted in Figure 3-17(c), where the thresholding creates a binary edge mask. This edge mask can then be used with the depth map to estimate depths of objects, similar to [102], which attempts to use a rough depth map with large objects. The benefit of this technique is that it provides a depth estimate for every object in the hologram – albeit poorly for the interior of objects and sharp corners. Fortunately, these problems have little effect when measuring the size or position of circular bubbles.

Two-phase flows face an additional challenge: since bubbles are distributed throughout the volume, there is a chance of overlapping edges in the intensity projection and depth maps. This appears as two or more distinct depths within a segmented edge map. A Gaussian Mixture Model (GMM) [89] is used to determine the most likely number and depths of the bubbles represented in each edge segment. GMMs with

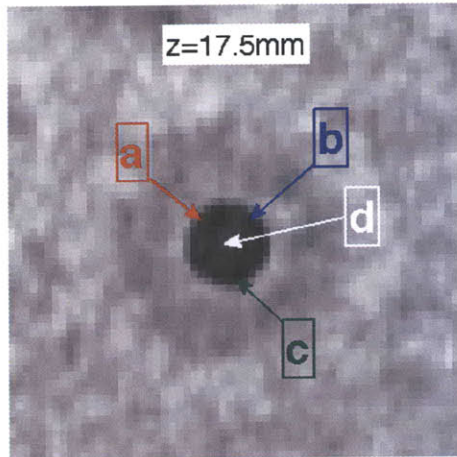
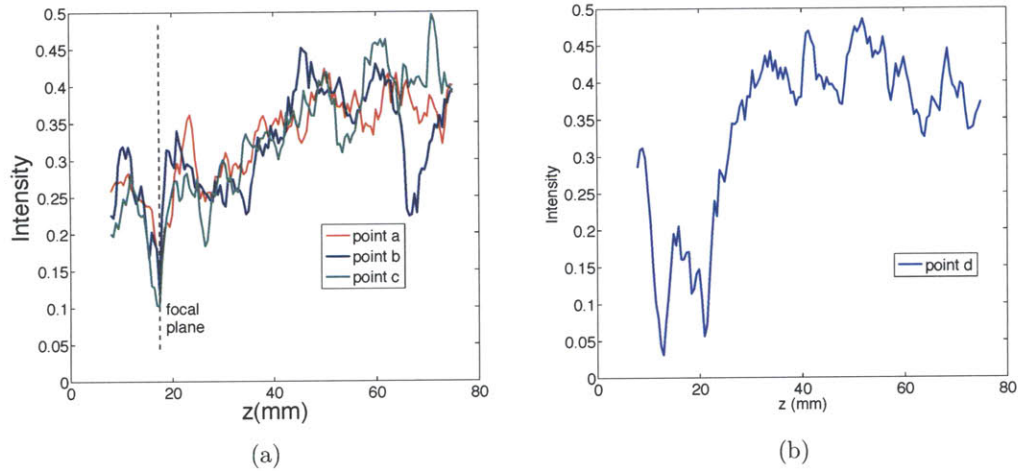


Figure 3-16: Demonstration of the edge minimum intensity focus metric. (a) intensity “column” corresponding to edge pixels a,b,c as function of distance z from the camera plane. The intensity is minimum at the focal plane. (b) In the intensity “column” for interior pixel d, the intensity is *not* minimum at the focal plane; (c) Intensity projection near a bubble that was located at $z=17.5$ mm.

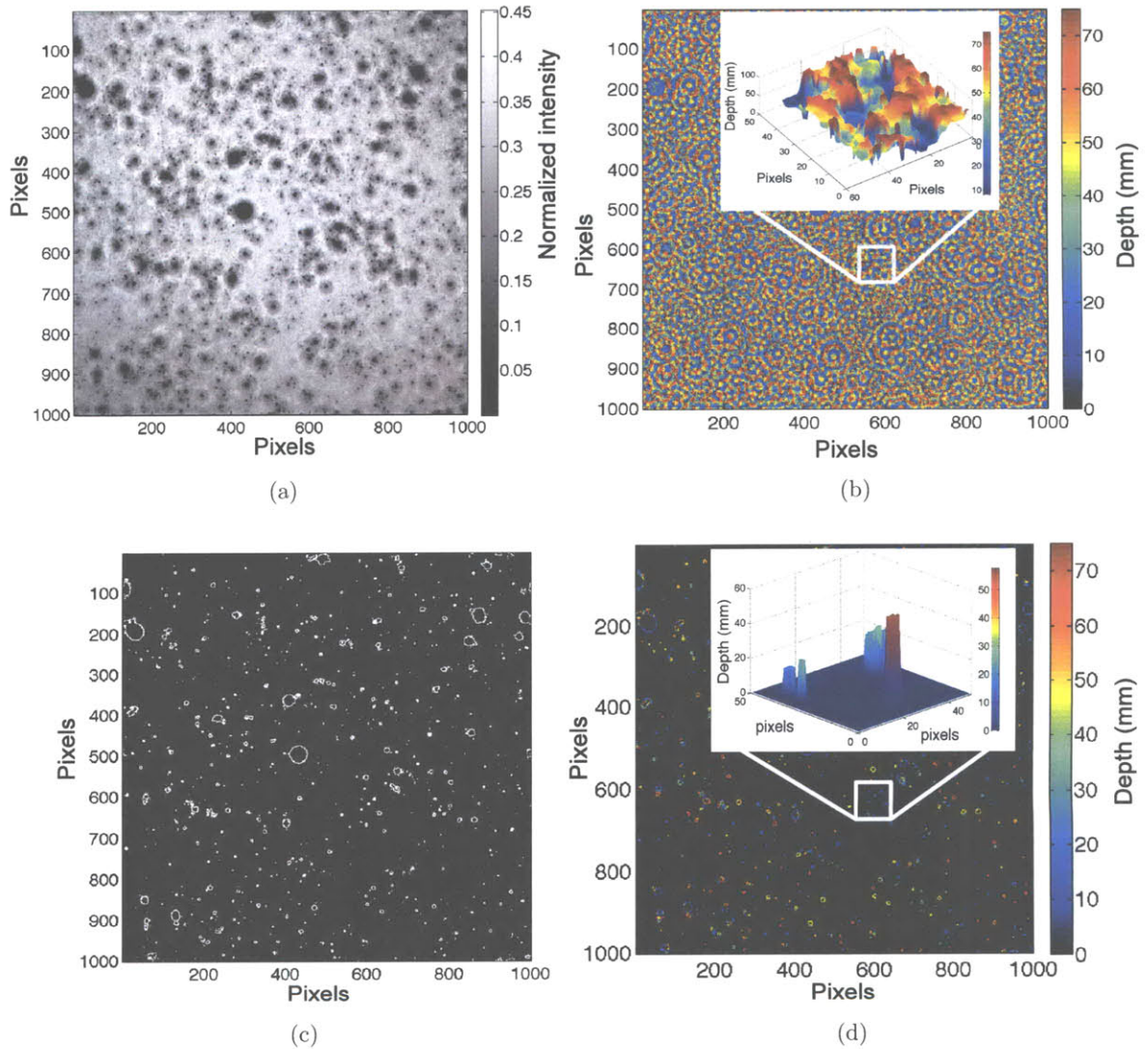


Figure 3-17: Diagram of key steps of the proposed DH data analysis algorithm applied to the air-in-water two-phase flows. (a) Intensity projection that contains all the in-focus pixels. (b) Original depth map records the axial value of the focal plane for every pixel. (c) Extracted edges on the thresholded intensity projection. (d) Refined depth map records only the axial value of in-focus bubbles.

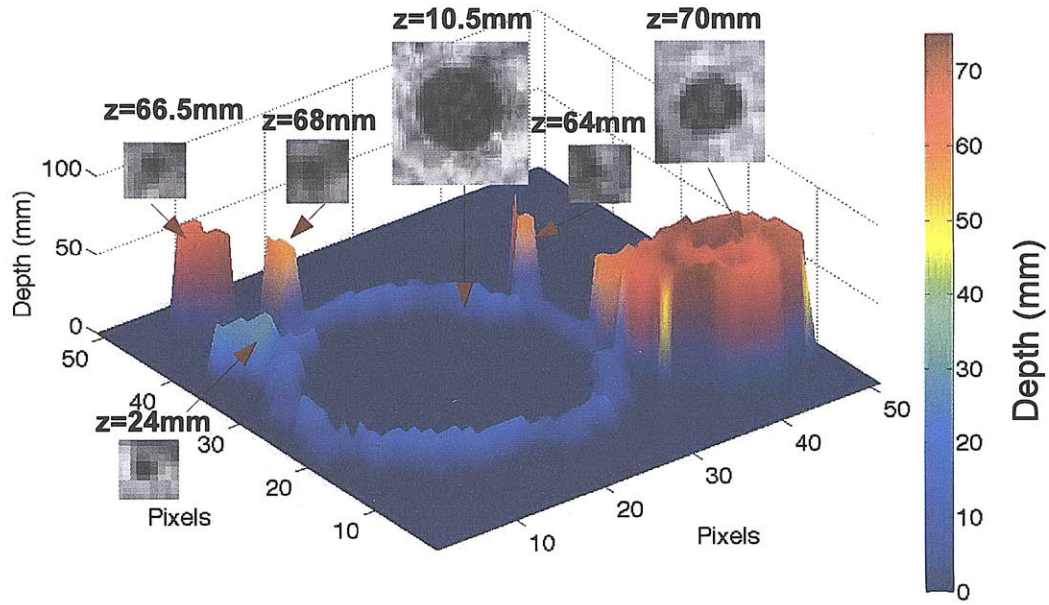


Figure 3-18: Depth map resulting from six bubbles, whose intensity projections are overlapping. After applying GMM (see text) they are successfully separated and their individual axial positions are determined. In-focus bubble images are shown in the insets.

varying number of mixture components are fit to the depth distribution for each edge segment, and the minimum Rissanen value [90] is used to select the most likely model. The mean of each mixture component gives the bubble depth. Edges corresponding to single bubbles also benefit from this approach as it statistically removes some of the measurement noise, applicable given that a *priori* knowledge that the bubble edge should appear at a single depth plane. A refined depth map, such as shown in Figure 3-17(d), is built from the GMM results. Figure 3-18 shows an example of how the GMM separates six overlapping bubbles as they appear on their common edge segment.

Finally, size and 3D position information of every bubble is obtained from the corresponding segments on the depth map. Bubble sizes are measured from the equivalent diameters computed from the enclosed areas of each segment.

The same data analysis algorithm is applied to the holograms of the oil-in-water two-phase flows. The intensity projection and the original depth map are shown in

Figure 3-19(a) and (b), respectively. The binarized projection is shown in 3-19(c). It is seen that the background fringes, produced by the sensor cover glass, are removed in this step. Finally, the refined depth map is shown in 3-19(d).

Experimental results

The automated data analysis algorithm is implemented in MATLAB (R2008a) on a Macintosh with a 2.5GHz Intel Core 2 Duo processor and 4 GB 667 MHz DDR2 SDRAM memory. The holograms are reconstructed with a 0.5mm separation between neighboring reconstruction planes. It takes about 9 minutes to process one hologram.

An example result from a single hologram of the air-in-water two-phase flows is shown in Figure 3-20. A 3D visualization of the positions and sizes of the bubbles recorded in this hologram is shown in Figure 3-20(a). Bubble sizes are scaled for visibility with color indicating bubble diameters. Figure 3-20(b) shows the bubble size distribution histogram. The first column of this histogram has an artifact due to pixel discretization. In this hologram, 1699 bubbles are detected with diameters ranging from less than $9\mu\text{m}$ (the detector pixel size) to $600\mu\text{m}$.

Fluid mechanics literature suggests that the air bubble generation process employed in our experiment should produce bubbles with size statistics following log-normal or gamma distribution [12, 106]. The probability density function of the log-normal distribution is

$$f(x; \mu, \sigma) = \frac{1}{x\sigma\sqrt{2\pi}} e^{-\frac{(\ln x - \mu)^2}{2\sigma^2}};$$

where μ is the mean of the bubble size's natural logarithm and σ is the standard deviation of the bubble size's natural logarithm.

The gamma distribution probability density function is

$$f(x; a, b) = x^{a-1} \frac{e^{-x/b}}{b^a \Gamma(a)}$$

The bubble size data from eight consecutive holograms, recorded in 1/3 fps, are

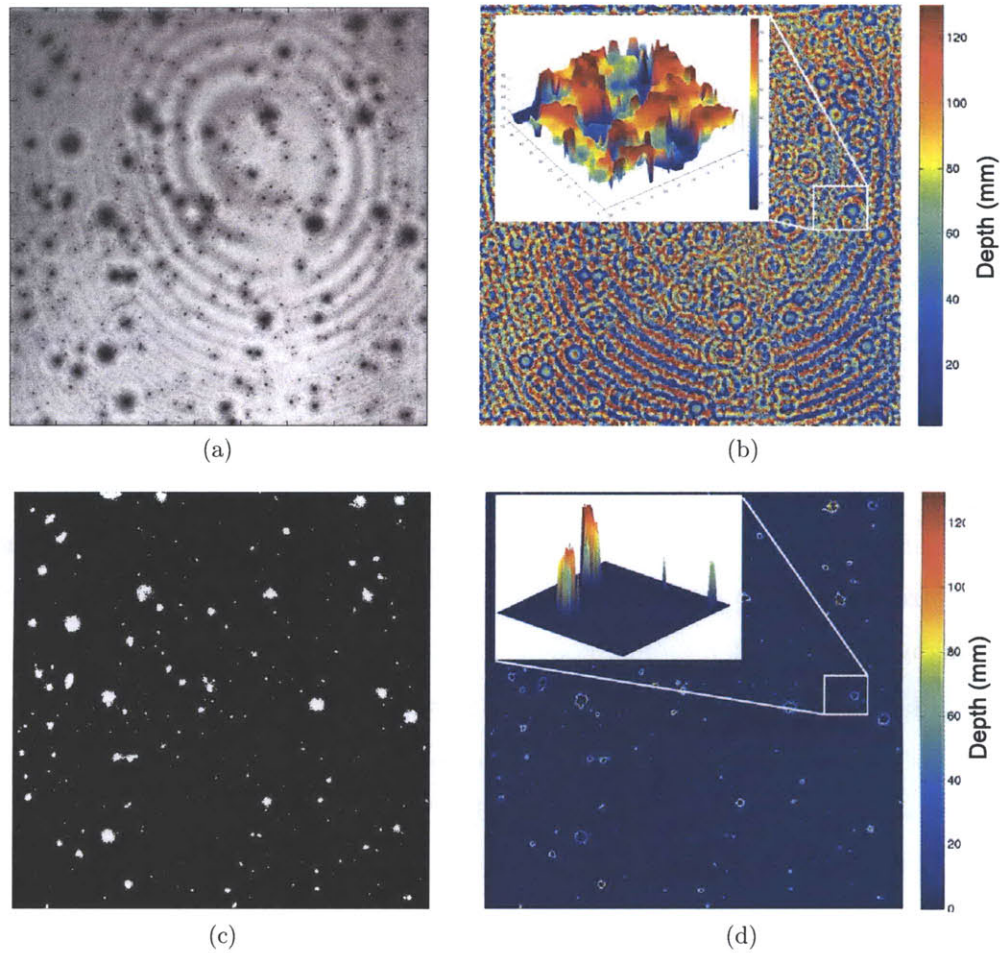


Figure 3-19: Diagram of key steps of the proposed DH data analysis algorithm applied to the oil-in-water two-phase flows. (a) Intensity projection that contains all the in-focus pixels. (b) Original depth map records the axial value of the focal plane for every pixel. (c) Binarized intensity projection. (d) Refined depth map records only the axial value of in-focus oil-droplets.

fitted to these distributions. The probability density and cumulative probability fitting curves of the bubble size data from one of the holograms are shown in Figure 3-21(a) and (b), whereas the fitting results for all the data from the eight holograms are shown in Figure 3-21(c) and (d). Figure 3-21 (a) and (c) have different bin settings because their data set had different cardinalities; nevertheless, both follow the Freedman-Diaconis rule [26] when generating histograms. The bubble size data were further subjected to a χ^2 goodness-of-fit test [17]. The parameters obtained by fitting the combined data are: in the log-normal distribution fit, $\mu = 3.31016$ and $\sigma = 0.718135$. In the gamma distribution fit, we obtained $a = 1.8665$ and $b = 19.6344$. Both log-normal and gamma distribution hypotheses passed the test at the 5% significance level. T-test [17] was also performed on the log-normal distribution hypothesis with $\mu = 3.31016$ assumption. The data passed the test with estimated $\sigma = 0.7181$.

The dynamic changes of the distribution parameters were further studied. The evolution in the log-normal and gamma distribution parameters over the eight consecutive holograms are shown in Figure 3-22(a) and (b), respectively. It is seen that, in the same experiment, all parameters fluctuate within a small range around the parameter obtained from the combined data quoted above. The holograms were recorded when the bubble generation process was in equilibrium. Log-normal distribution fits have relatively more stable parameters, which might suggest that log-normal distribution interprets this particular type of two-phase flows better. Figure 3-23 shows four frames among the eight consecutive holograms.

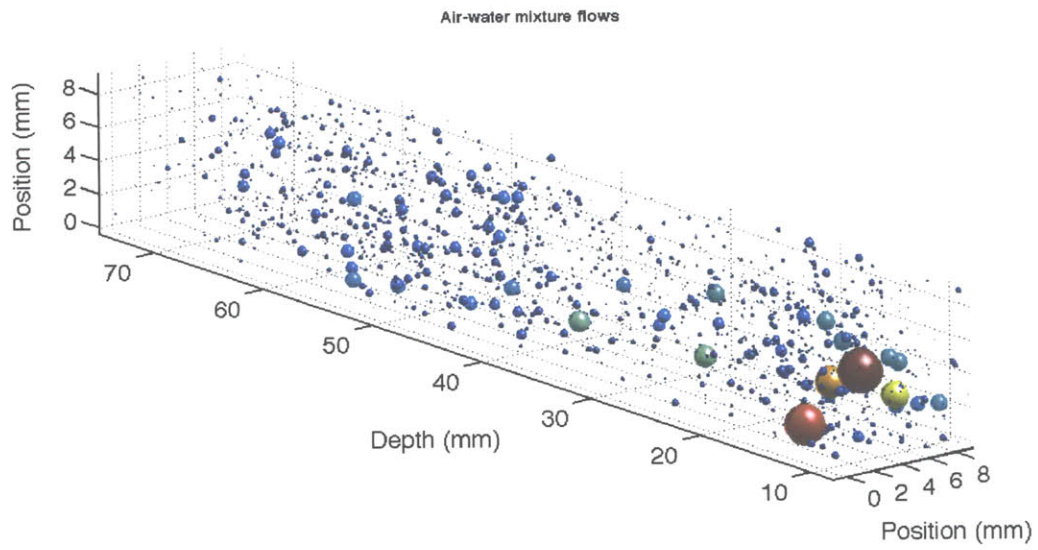
The automated data analysis algorithm is also applied to analyze the holograms of the oil-in-water two-phase flows. Figure 3-24(a) shows a 3D visualization of the processing results from a single hologram. Oil-droplet sizes are scaled for visibility with color indicating oil-droplet diameters. Figure 3-24(b) shows the oil-droplet size distribution histogram. The first column of this histogram has an artifact due to discretization. Oil-drop size data were fitted to a lognormal distribution, as suggested in [73]. The size distributions provide a measure of the dynamics during the separation process. The evolution in the log-normal mean and standard deviation

of the oil-droplet size, over 21 consecutive holograms spaced approximately 15 seconds apart, are shown in Figure 3-25(a) and (b), respectively. It is seen that the mean is statistically stationary, while the standard deviation drops significantly during the separation process. The larger droplets have increased buoyancy and rise past the field-of-view faster, and also break into medium size droplets; while the smaller droplets merge into medium size droplets. This is also evident in Figure 3-26, which shows four frames among the 21 consecutive holograms.

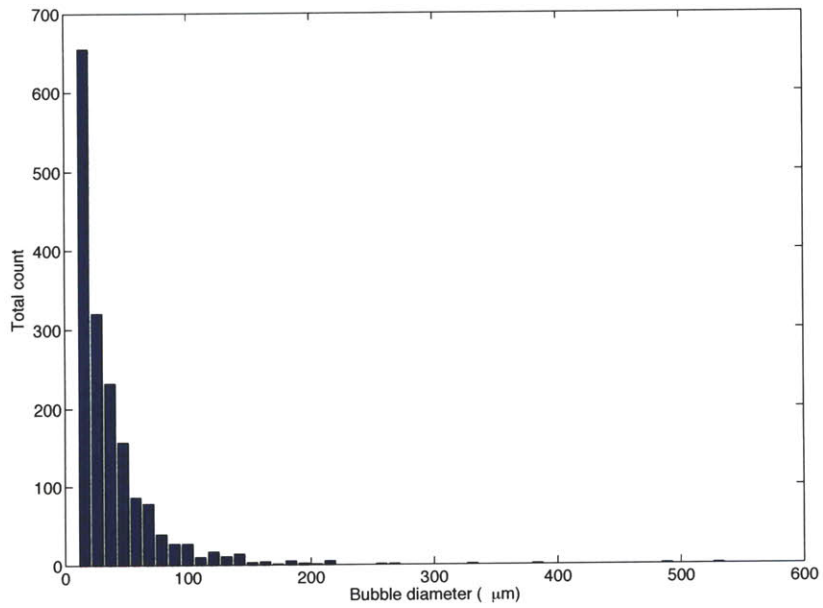
3.4 Conclusion

In this chapter, the holographic imaging system was analyzed by phase-space optics. The holographic information in the phase-space is in the interference terms of the reference field and the object field. In the Wigner space, the interference terms appear in the mid-way between the reference WDF and the object WDF. In the Ambiguity space, the interference terms are in high frequency region. This is useful when filtering in phase-space is applied.

An in-line digital holographic imaging system was applied to study two-phase flows. The captured holograms were numerically processed by performing a 2D projection followed by local depth estimation to obtain the size and position information of multiple bubbles simultaneously. It was shown that DH is a promising quantitative measurement technique in two-phase flow research.

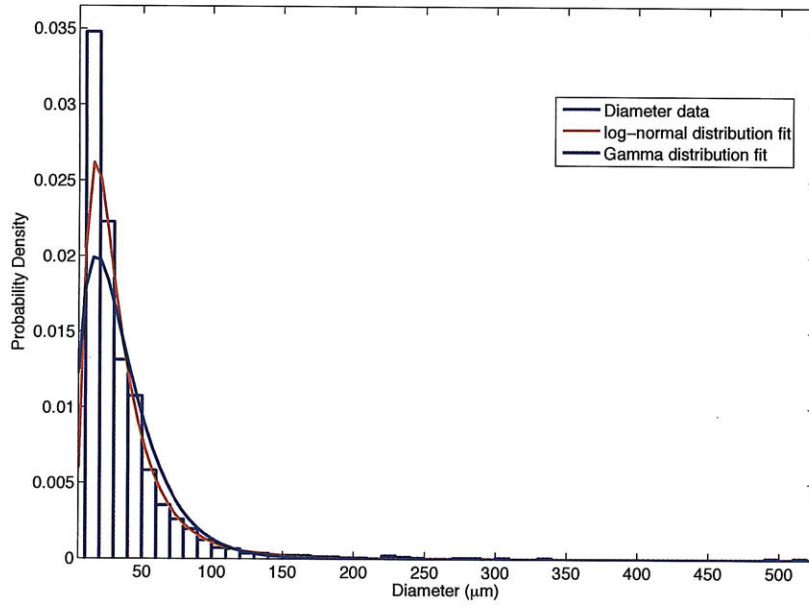


(a) 3D visualization of data processing results from a single hologram of the air-in-water two-phase flows (diameters not to scale)

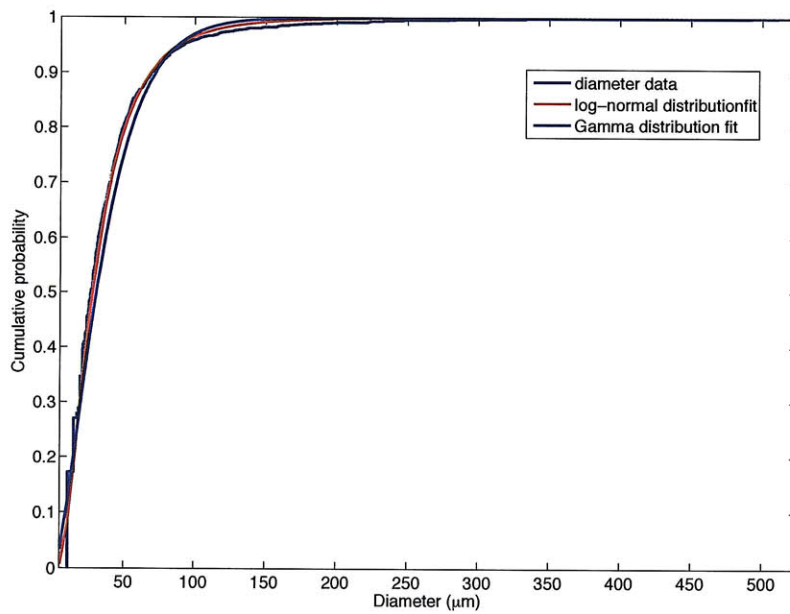


(b) Bubble size distribution

Figure 3-20: Data processing result from a 1000×1000 -pixel hologram of the air-in-water two-phase flows.

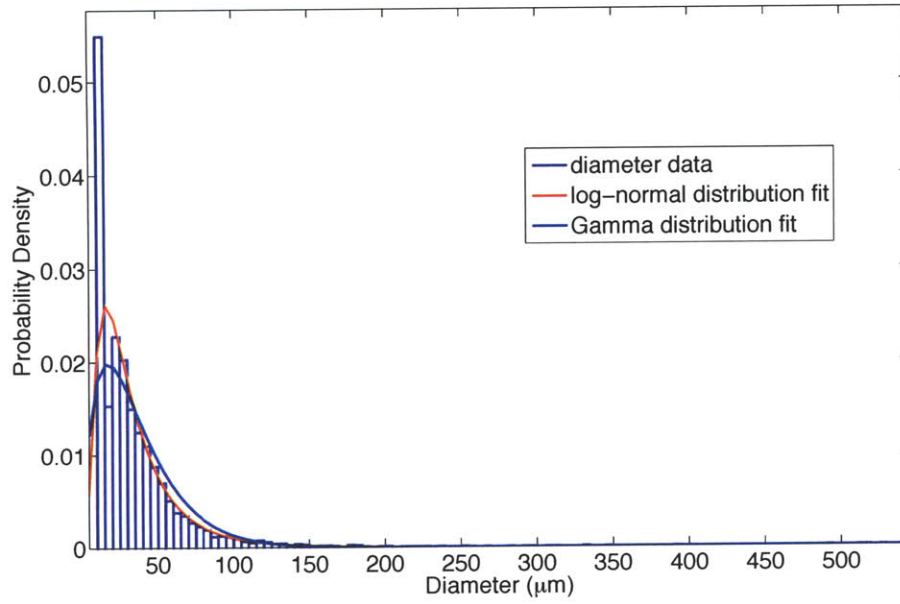


(a) Histogram of bubble sizes and probability distribution fits for a single hologram.

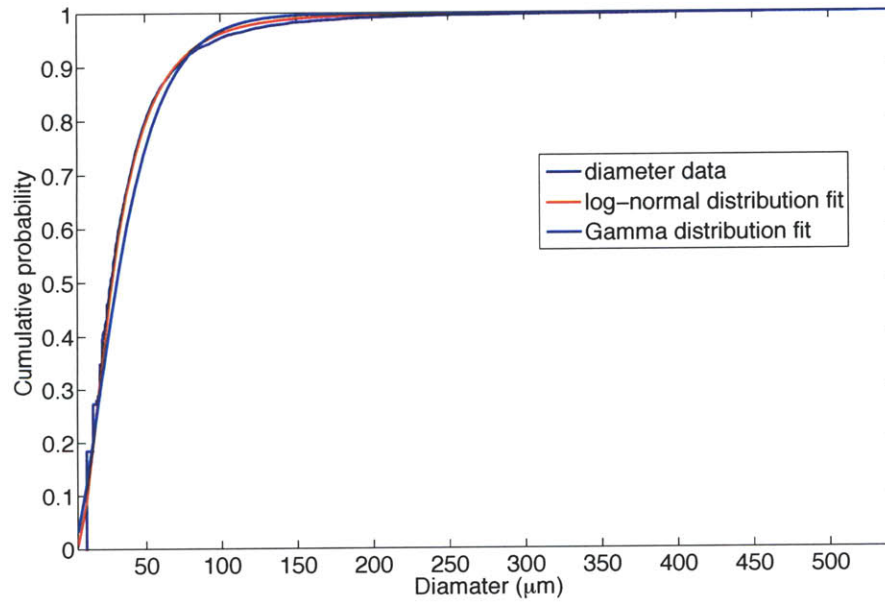


(b) Cumulative probability of the data and fits of (a).

Figure 3-21: Bubble size data fitted to lognormal and gamma distributions.

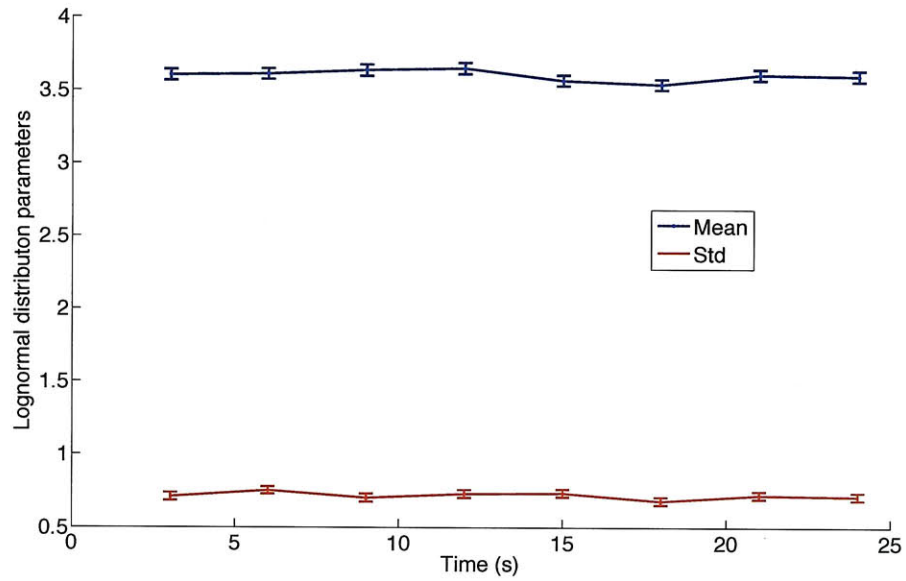


(c) Sizes and probability distribution fits for bubbles in eight consecutive holograms.

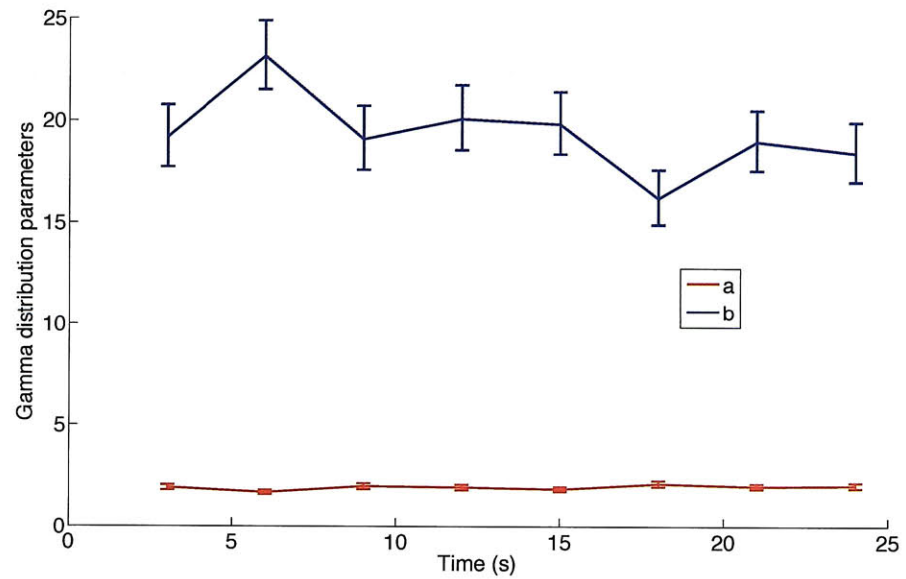


(d) Cumulative probability of the data and fits of (c).

Figure 3-21: Bubble size data fitted to lognormal and gamma distributions.

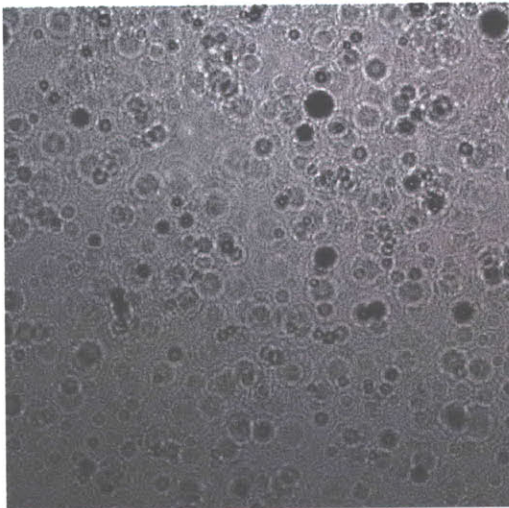


(a) Log-normal distribution parameters. μ : blue, σ : red.

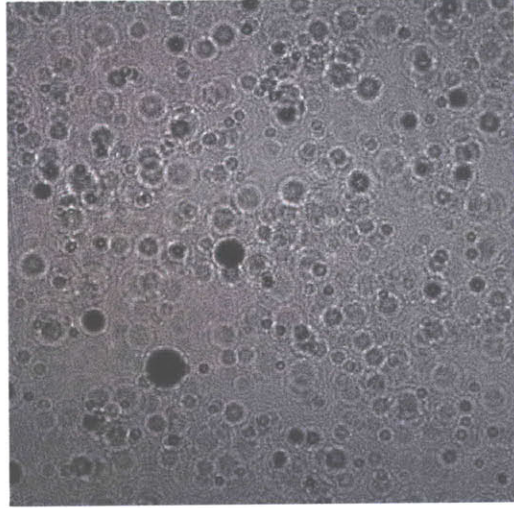


(b) Gamma distribution parameters. a : red, b : blue.

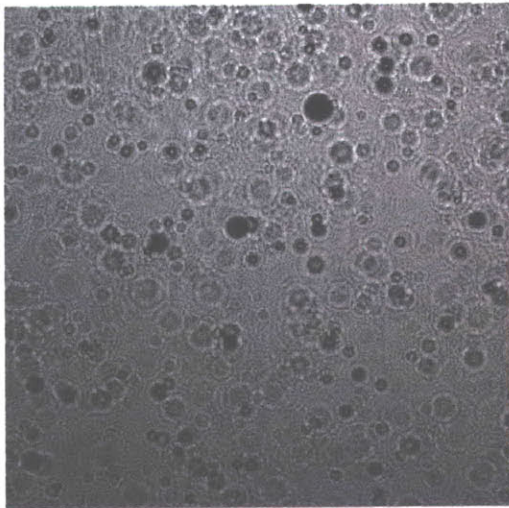
Figure 3-22: Bubble size distribution parameter evolution over eight consecutive holograms; error bars show the 90% confidence intervals for the estimated distribution parameters.



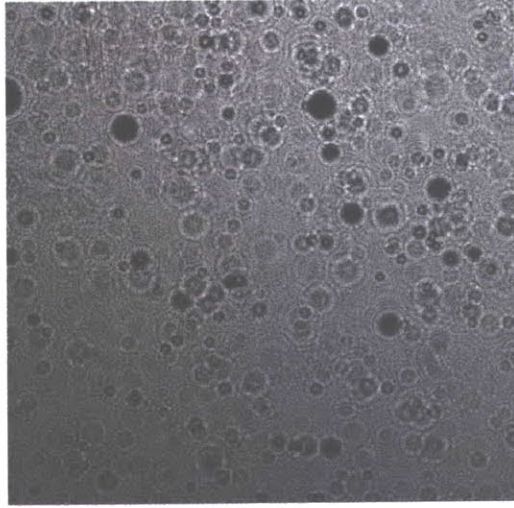
(a) Frame 1



(b) Frame 3

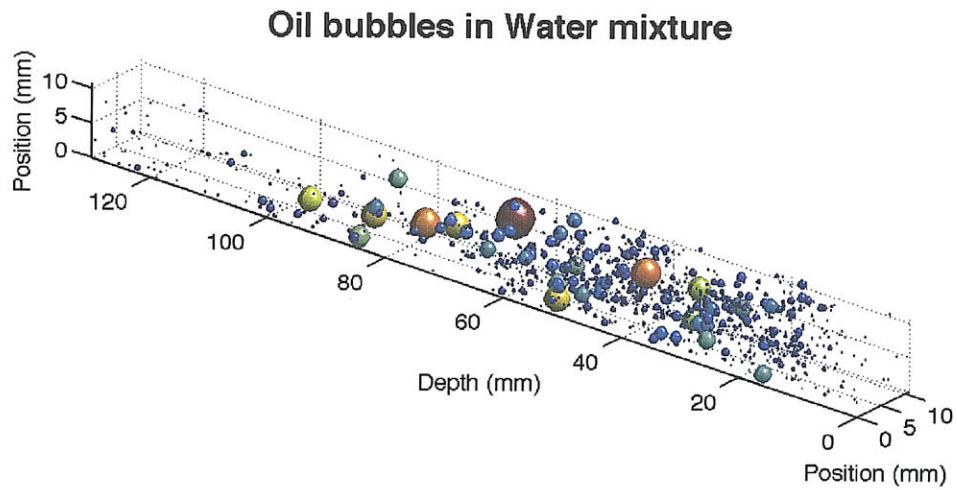


(c) Frame 5

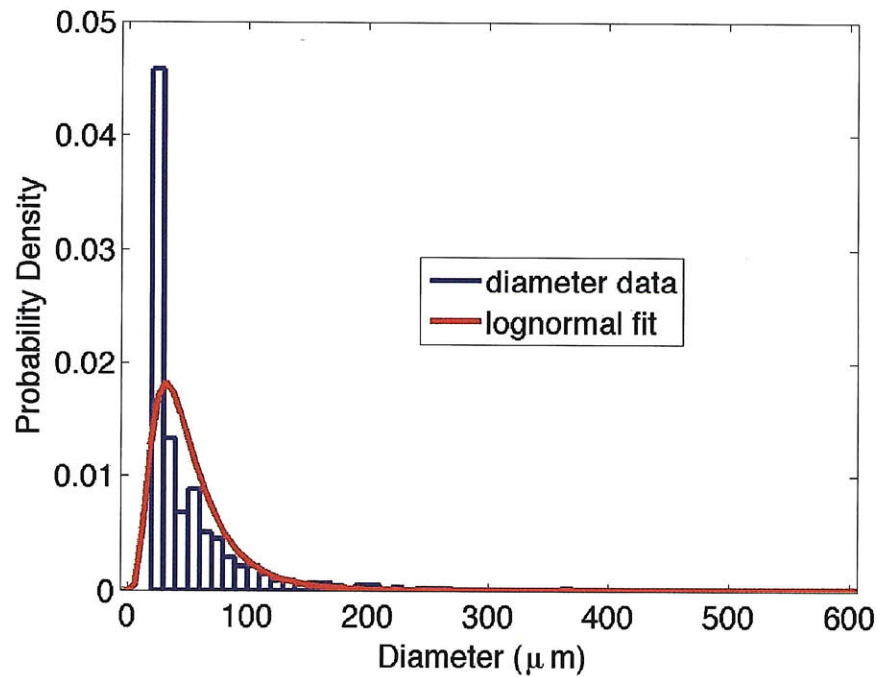


(d) Frame 8

Figure 3-23: Evolution of the holograms of the air-in-water two-phase flows.

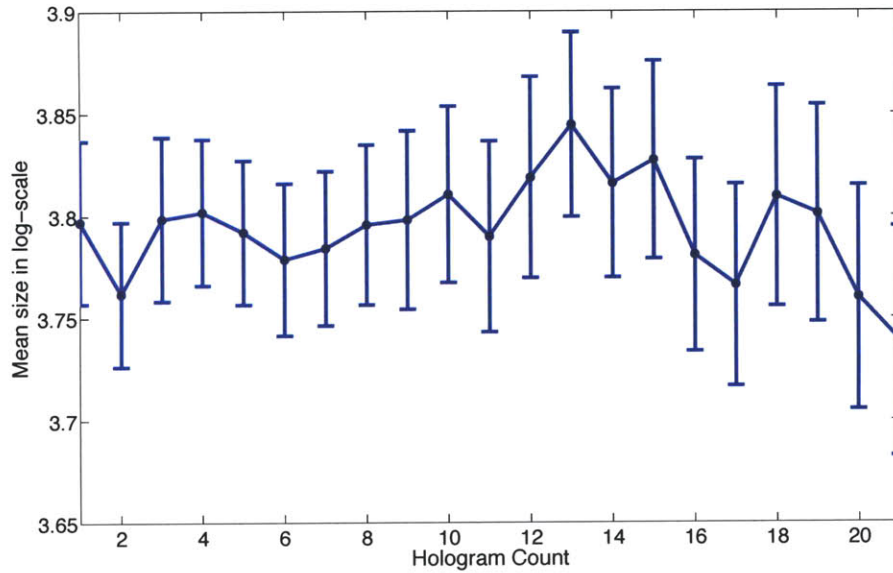


(a) 3D visualization of data processing results from a single hologram of the oil-in-water two-phase flows (not to scale)

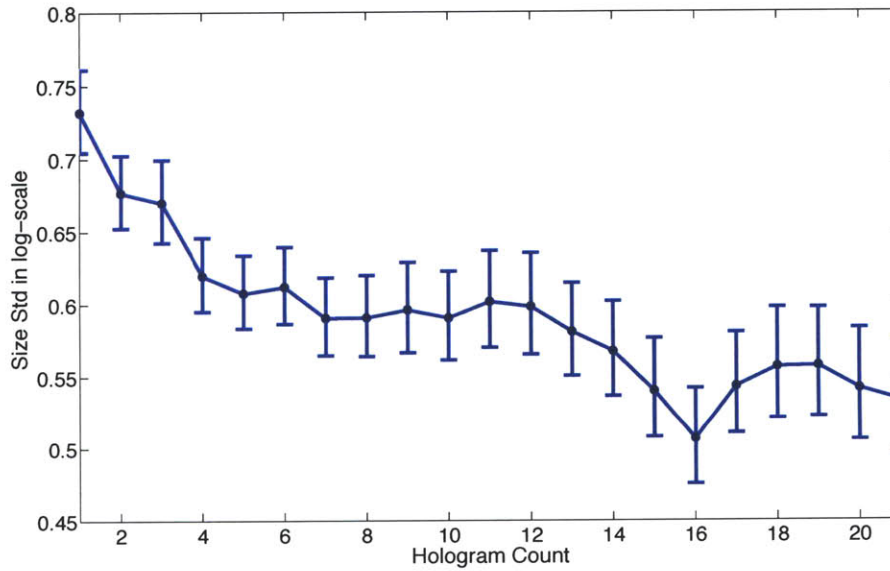


(b) Histogram of oil-droplet sizes and probability distribution fits for a single hologram

Figure 3-24: Data processing result from a 900×900 -pixel hologram of the oil-in-water two-phase flows.

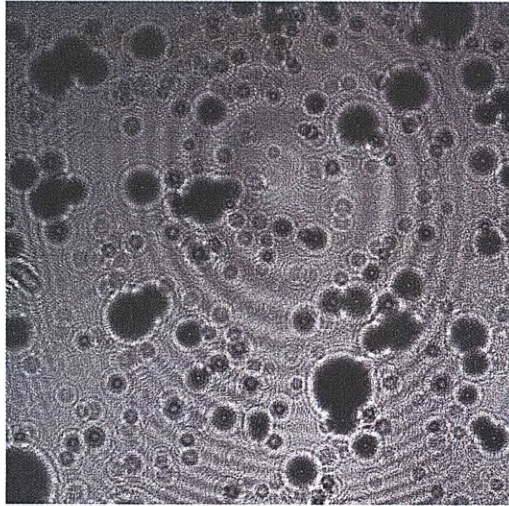


(a) Dynamic change in the log-normal mean oil-droplet size

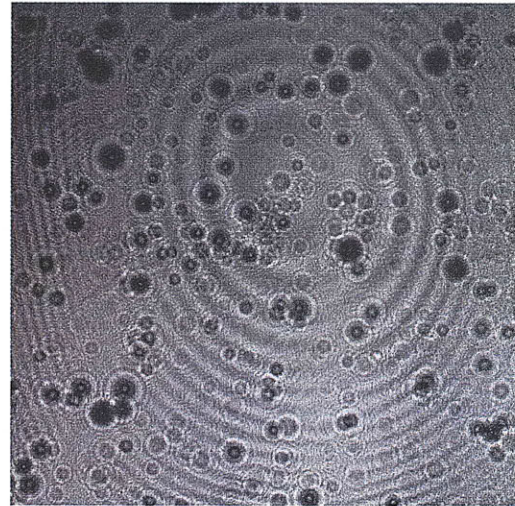


(b) Dynamic change in the log-normal standard deviation of the oil-droplet size

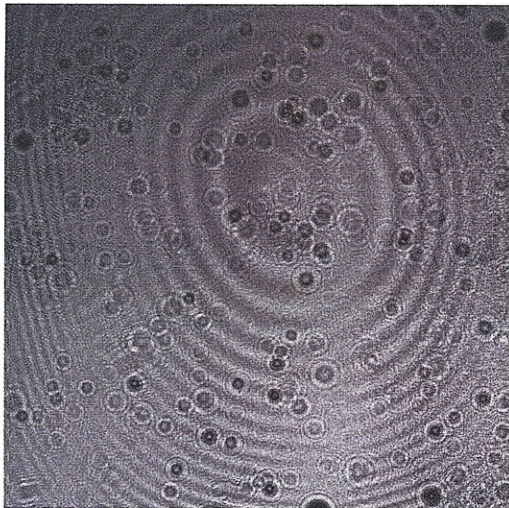
Figure 3-25: Oil-droplet size distribution parameter evolution over 21 consecutive holograms spaced approximately 15 seconds apart; error bars show the 90% confidence intervals for the estimated distribution parameters.



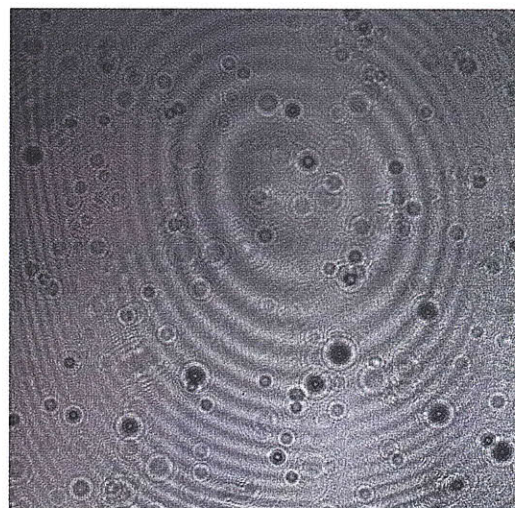
(a) Frame 2



(b) Frame 8



(c) Frame 16



(d) Frame 21

Figure 3-26: Evolution of the holograms of the oil-in-water two-phase flows.

Chapter 4

Light field imaging in phase-space

In high-density flows, the hologram of two-phase flows taken from a single view becomes a speckle-like noisy image. In addition, significant occlusions prevent targets from being observed due to information loss. One way to overcome the challenge of partial occlusion is to integrate views from multiple perspectives. Occlusion differs from view to view, and by digitally integrating multiple views, the shape of a target embedded in an occlusive media can be reconstructed. This perspective imaging principle is widely used in a number of imaging techniques, such as stereo imaging [92], synthetic aperture imaging [45], integral imaging [4], and light field imaging [47].

The use of a lens arrays to capture light fields has its roots in Lippmann's 1908 invention of integral imaging [49]. The principle of the system is that each lenslet records a perspective view of the scene observed from that position on the array. A conjugate system to integral imaging, termed light field imaging and often called plenoptic camera [2, 66] in the literature, is to put a field lens in front of the microlens array. Instead of taking perspective views of the scene directly, the light field system takes perspective views of the field lens under each microlens; perspective views of the scene are obtained by post-processing. A microlens array is also used in adaptive optics, where it is known as Shack-Hartmann wavefront sensor [84]. The microlens array focuses light onto a detector. As the wavefront slope changes at the lens, the lateral position of the focus shifts, thus enabling the wavefront slope to be sensed. Figure 4-1 shows the schematics of integral imaging and light field imaging, respec-

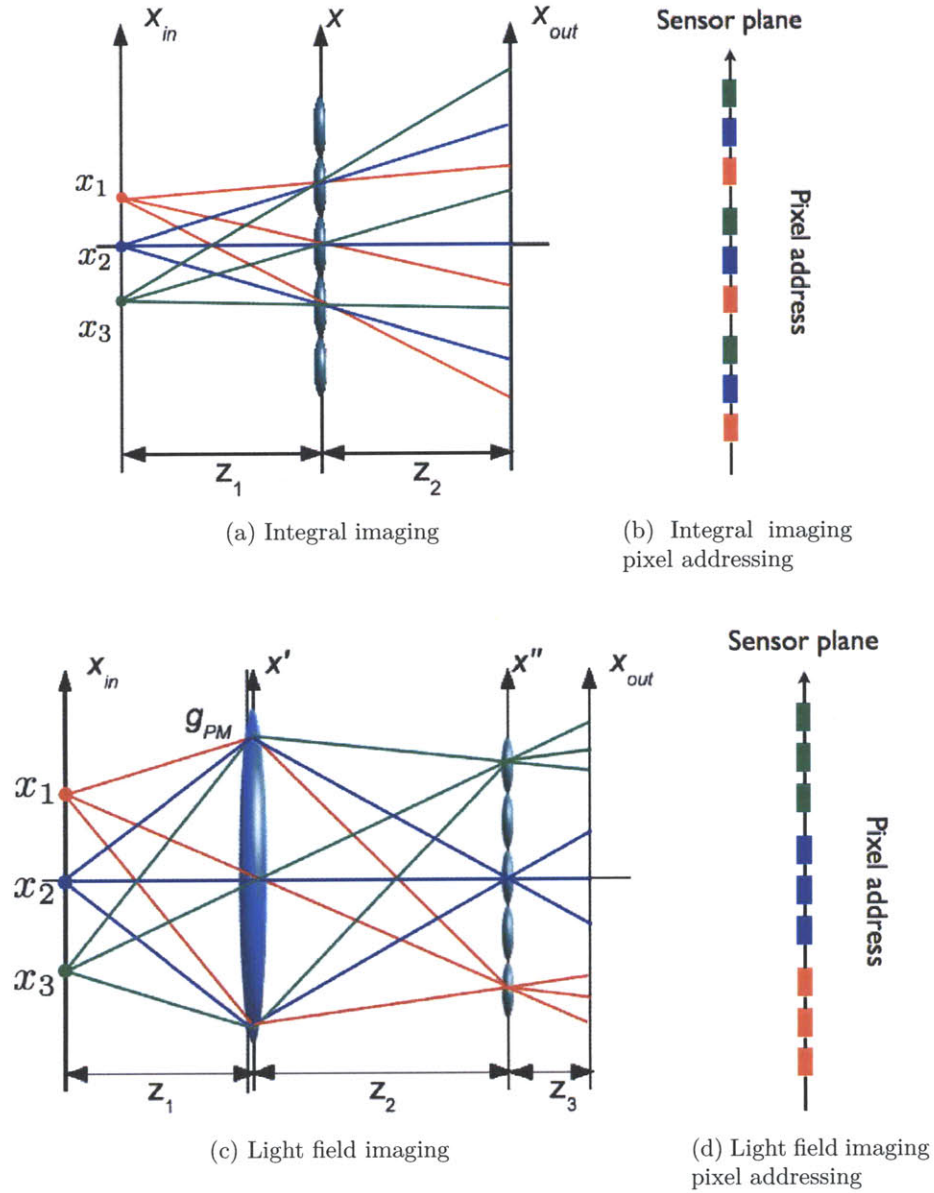


Figure 4-1: (a) Schematics of integral imaging and its pixel addressing at the sensor plane in (b); (c) Schematics of light field imaging and its pixel addressing at the sensor plane in (d).

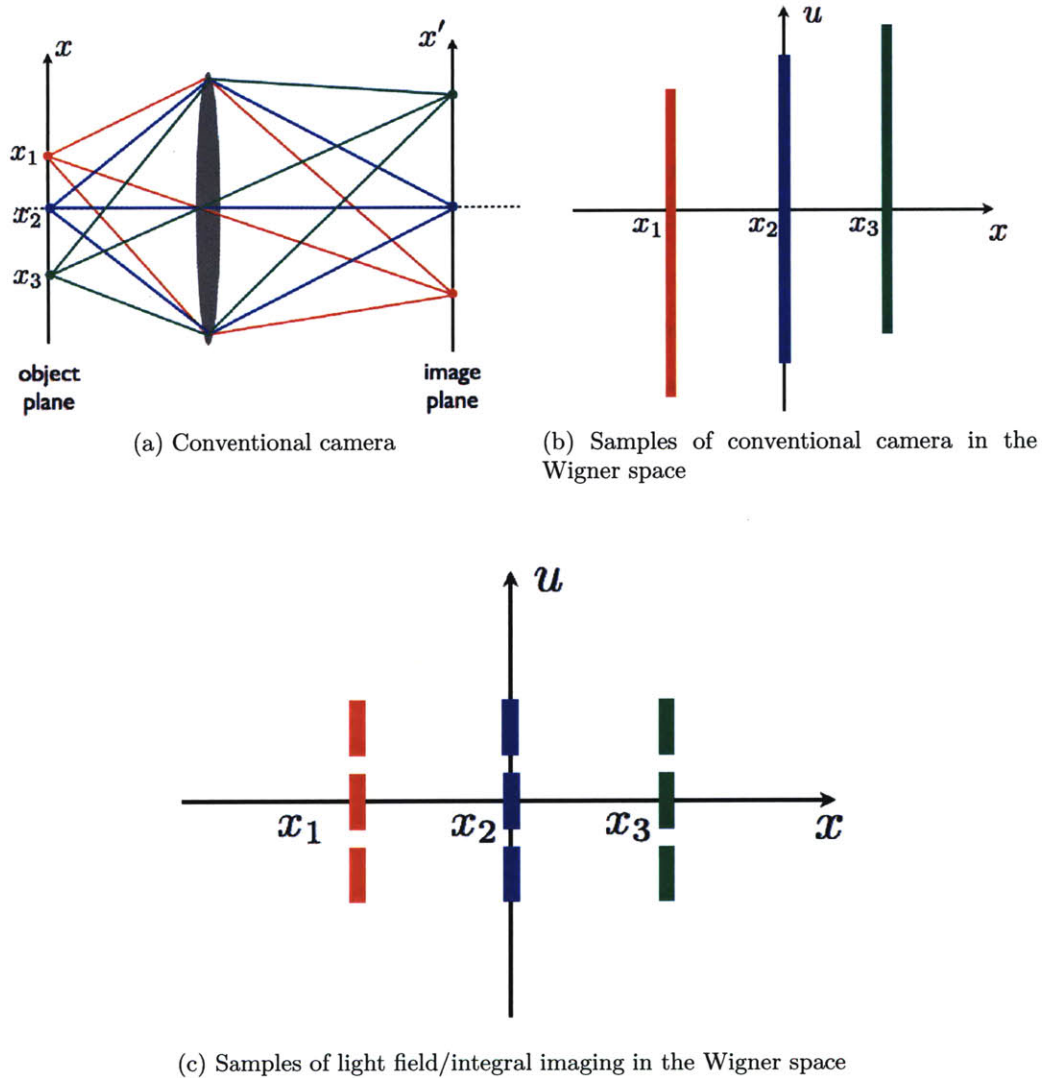


Figure 4-2: In conventional single lens imager, all rays from a point object are mapped to a point on the image plane, as shown in (a); In the Wigner space, samples are taken along the space x coordinate but not along the spatial frequency u coordinate, as shown in (b); In integral imaging (Figure 4-1(a-b)) and light field imaging (Figure 4-1(c-d)), samples are taken along both x and u coordinates, as shown in (c).

tively. Three object points at different positions x_1, x_2 and x_3 are mapped to different position at the sensor plane. In addition, different spatial frequencies, which correspond to different rays, of the same object point are also mapped to different pixels. Integral imaging and light field imaging have different pixel addressing at their sensor planes. Detailed analysis will be presented in the subsequent sections. As a comparison, Figure 4-2(a) shows the schematic diagram of a conventional camera with only a field lens to conjugate the object plane and the sensor plane. Each object point is mapped to a single point at the imaging plane. We can also compare the sampling schemes in the Wigner space. In Figure 4-2(b), the samples of a conventional camera are illustrated as continuous lines oriented along the spatial frequency (u) axis. So the conventional camera can only have (lateral) position discrimination. Samples of light field and integral imaging in the Wigner space are shown as dashed lines in Figure 4-2(c). This is because both space and spatial frequency information are obtained in these two setups.

4.1 Light fields and the Wigner distribution function

4.1.1 Light fields

“Light field” is a geometrical optics concept widely used in computer graphics community [44], mapping from rays to radiance. The concept was first introduced by Arun Gershun in 1936 [32] and defined as a 5D function, which gives the amount of light (radiance) traveling in every direction (parameterized by two directional cosines) through every point in space (parameterized by three Cartesian coordinates). This 5D representation is known as plenoptic function [1], and is shown in Figure 4-3(a). However, the 5D representation may be reduced to 4D in free space [36, 46, 63]. This is a consequence of the fact that the radiance is conservative along a ray unless blocked. The 4D set of rays can be parameterized in a variety of ways. One widely used representation is to parameterize the light field by two planes, where each ray is

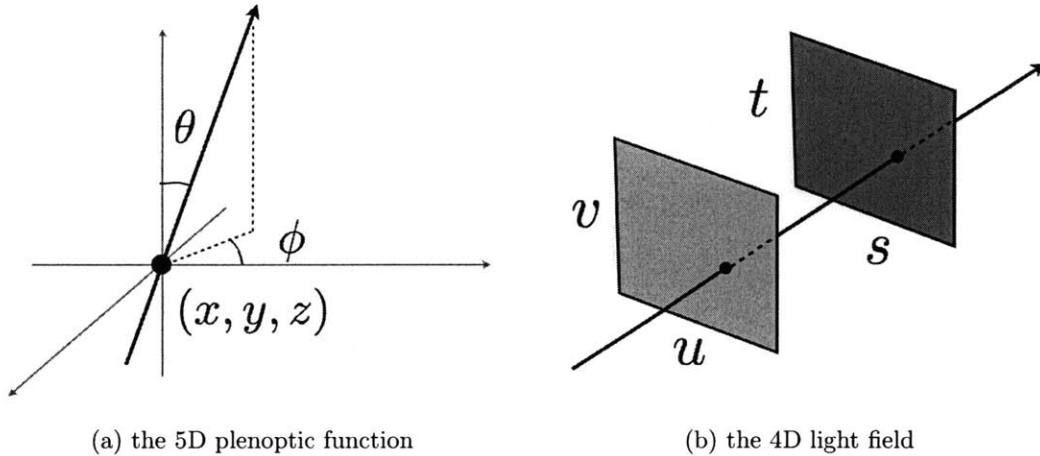


Figure 4-3: Light field parameterizations.

encoded by its intersections with two parallel planes [46], as shown in Figure 4-3(b). While this parameterization cannot represent all rays, for example, rays parallel to the two planes, it relates closely to the analytic geometry of perspective imaging [44]. As illustrated in Figure 4-3(b), a collection of perspective images of the st plane is taken from an observer position on the uv plane.

4.1.2 Radiance and the Wigner distribution

Radiance

Before relating light field to the WDF, we shall first find the connections between the radiance and the WDF. The concept of radiance comes from the geometrical models for energy transport in optical fields [8]. The basic assumption is that the energy radiated from an element $d\sigma$ of a planar source is distributed according to the elementary law

$$d\phi = B_\nu(\mathbf{r}, \mathbf{s}) \cos \theta d\sigma d\Omega dt \quad (4.1)$$

where $d\phi$ represents the amount of energy, per unit frequency interval at frequency ν , that is propagated in a short time interval dt from a source element $d\sigma$ at a point Q , specified by position vector \mathbf{r} into an element $d\Omega$ of solid angle around a direction specified by unit vector \mathbf{s} . θ denotes the angle that the \mathbf{s} direction makes with the

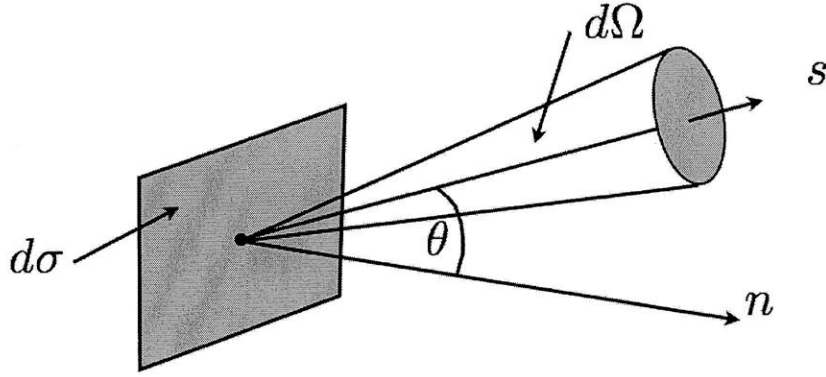


Figure 4-4: Illustration of the definition of the radiance function $B(\mathbf{r}, \mathbf{s})$.

unit normal \mathbf{n} to the source plane, as shown in Figure 4-4. The proportionality factor $B_\nu(\mathbf{r}, \mathbf{s})$, which in general depends on position (\mathbf{r}), direction (\mathbf{s}) and frequency (ν), is known as the radiance function. The energy flux emanating from a surface is calculated by

$$\phi = \iint B_\nu(\mathbf{r}, \mathbf{s}) \cos \theta d\sigma d\Omega \quad (4.2)$$

Radiance in wave optics

The relationship between the radiance function and the wave optics were first studied by A. Walther [107, 108, 110], and later by E. Wolf [56, 113] in the 1970s through the theory of partial coherence. First, write the field in its angular spectrum form

$$u(x, y, z) = \iint U(L, M) \exp\{ik(Lx + My + Nz)\} dLdM, \quad (4.3)$$

$$N = \sqrt{1 - L^2 - M^2}$$

where $(L, M, N) = \mathbf{n}$ denotes a unit vector which indicates the propagation direction of a plane wave with amplitude $U(L, M)$. The position vector is given by $\mathbf{r} = (x, y, z)$. $dLdM$ can be related to solid angle $d\Omega$ by

$$d\Omega = dLdM/N. \quad (4.4)$$

For partially coherent illumination, the field is described by the mutual intensity, which is defined as the ensemble averages

$$\begin{aligned}
\Gamma(\mathbf{r}_1, \mathbf{r}_2) &= \langle u(\mathbf{r}_1)u^*(\mathbf{r}_2) \rangle \\
&= \iiint \hat{\Gamma}(L_1, M_1, L_2, M_2) \\
&\quad \exp\{ik[L_1x_1 + M_1y_1 + N_1z_1 - L_2x_2 - M_2y_2 - N_2z_2]\} \\
&\quad dL_1dM_1dL_2dM_2,
\end{aligned} \tag{4.5}$$

where

$$\hat{\Gamma}(L_1, M_1, L_2, M_2) = \langle U(L_1, M_1)U^*(L_2, M_2) \rangle. \tag{4.6}$$

The energy flux associated with the field [107] is

$$\Phi = \iint N\hat{\Gamma}(L, M, L, M)dLdM. \tag{4.7}$$

we now introduce the average location of two points and their separation by writing

$$\begin{aligned}
x_a &= \frac{1}{2}(x_1 + x_2), \\
x_d &= x_1 - x_2,
\end{aligned} \tag{4.8}$$

and similarly for y . Applying the same transformation to the direction cosines,

$$\begin{aligned}
L_a &= \frac{1}{2}(L_1 + L_2), \\
L_d &= L_1 - L_2,
\end{aligned} \tag{4.9}$$

and similarly for M and noting that $N = \cos\theta$, we can rewrite Equation (4.7) in terms of the transformed variables as

$$\Phi = \int N_a\hat{\Gamma}(L_a, M_a, 0, 0)d\Omega \cos\theta. \tag{4.10}$$

In his paper, Walther introduced a function that takes the Fourier transform on

$\hat{\Gamma}(L_a, M_a, L_d, M_d)$ only to L_d and M_d

$$\hat{\Gamma}(L_a, M_a, L_d, M_d) = \frac{1}{\lambda^2} \iint \Gamma'(L_a, M_a, x_a, y_a) \exp\{-ik[L_d x_a + M_d y_a]\} dx_a dy_a. \quad (4.11)$$

It is easy to recognized that $\Gamma'(L_a, M_a, x_a, y_a)$ is the WDF of the field. Noting that $dx_a dy_a = d\sigma$ is the element area,

$$\hat{\Gamma}(L_a, M_a, 0, 0) = \frac{1}{\lambda^2} \iint \Gamma'(L_a, M_a, x_a, y_a) d\sigma. \quad (4.12)$$

Finally, we can find the radiance defined in wave optics quantities by relating Equation (4.1) and Equation (4.10) as

$$B = (1/\lambda^2)\Gamma'(L_a, M_a, x_a, y_a). \quad (4.13)$$

Equation (4.13) shows that the radiance is, up to a scaling constant, equal the WDF of the scalar field. Later, Walther showed that the radiance given by Equation (4.13) is a unique solution [110]. Radiance defined by Equation (4.13) is known as the generalized radiance function. However, the expression for radiance given by Equation (4.13), being the WDF of a scalar field, can become negative, which violates the positivity of radiance. In fact, Friberg showed that there cannot be a radiance function satisfying all the ideal properties of radiance [27]. On the other hand, in the short-wavelength limit, Walter's equation for radiance, (4.13), has been shown to satisfy all the ideal properties of radiance [24, 40], thereby proving the Wigner distribution equivalent to radiance at this limit. We shall conclude that the Wigner distribution of a scalar field is good measure of the radiance of this field.

Another interesting remark in finding the relationship between intensity distribution and coherence properties was pointed out in Walther's paper [107]. By substituting the transformations in variables by Equation (4.8) and Equation (4.9) into the

exponent when calculating the mutual intensity in Equation (4.5), he obtained

$$ik[L_1x_1 + M_1y_1 - L_2x_2 - M_2y_2] = ik[L_dx_a + M_dy_a + L_ax_d + M_ay_d]. \quad (4.14)$$

This shows that (x_a, L_d) , (y_a, M_d) , (x_d, L_a) , and (y_d, M_a) are Fourier pairs. The dependence of $\Gamma(x_a, y_a, x_d, y_d)$ on x_a and y_a represents the intensity distribution in the plane $z = 0$, while its dependence on x_d and y_d represents the coherence properties in this plane. In the far field, the dependence of $\hat{\Gamma}(L_a, M_a, L_d, L_d)$ on L_a and M_a (L_d and M_d) gives similar results.

4.1.3 Light field and the Wigner distribution

The relationship between the light field and the Wigner distribution function was recently studied by Zhang [119]. Since we have derived that the radiance is equal to the Wigner distribution, and the light field is equivalent to the radiance, it is seen that the light field is equal to the Wigner distribution

$$l(x, y, L, M) = \mathcal{W}(x, y, L/\lambda, M/\lambda) = \mathcal{W}(x, y, u, v). \quad (4.15)$$

One remaining question is to relate the theory to measurable quantities in experiments. This question is two-fold: on one hand, the Wigner distribution can be negative, in which case it is not a physically measurable quantity. On the other hand, there is no angular variation in radiance of the light transmitted through a point. A related issue is that, due to the uncertainty principle, simultaneously precise measurements in both space and spatial frequency(angle) are impossible. One possible solution is to consider that samples of the radiance (the Wigner distribution, and the light field) are taken by detectors with finite size. The resulting quantity is called the observable light field in [119].

Consider light transmitted through an arbitrary finite aperture centered on the point $(s, t, 0)$. The aperture has a transmittance function $T(x, y)$. The aperture is translated along the reference plane (s, t) at $z = 0$. Suppose we can measure the

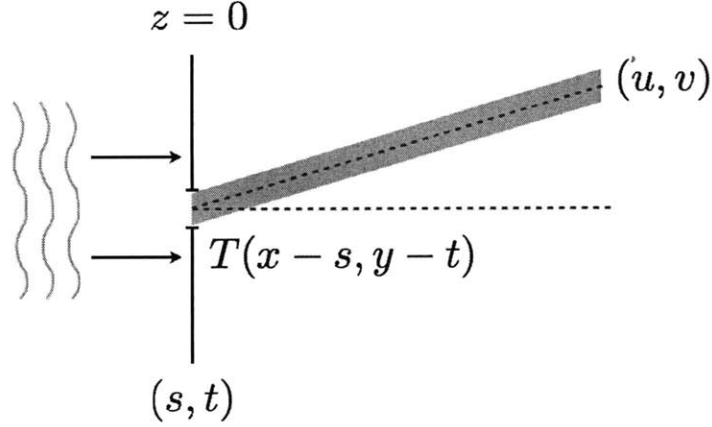


Figure 4-5: A physically measurable quantity related to the radiance is the intensity of light emanating in a particular direction (u, v) from a translated aperture $T(x - s, y - t)$.

intensity of light emanating in a particular direction (u, v) from a translated aperture $T(x - s, y - t)$, as shown in Figure 4-5.

Given a scalar field $u(x, y)$, the field after the aperture is $u(x, y)T(x - s, y - t)$. It can be written as its angular spectrum

$$\hat{U}(u, v) = \iint u(x, y)T(x - s, y - t) \exp\{-i2\pi(ux + vy)\} dx dy \quad (4.16)$$

The measured intensity is, dropping the scaling constant,

$$\begin{aligned} \mathcal{W}_{obs}(s, t, u, v) &= \langle |\hat{U}(u, v)|^2 \rangle \\ &= \iiint \langle u(x_1, y_1)u^*(x_2, y_2) \rangle \\ &\quad \times T(x_1 - s, y_1 - t)T^*(x_2 - s, y_2 - t) \\ &\quad \exp\{-i2\pi(u(x_1 - x_2) + v(y_1 - y_2))\} dx_1 dx_2 dy_1 dy_2. \end{aligned} \quad (4.17)$$

Rewriting Equation (4.17) into average and difference variables yields:

$$\begin{aligned} \mathcal{W}_{obs}(s, t, u, v) &= \iiint \langle u(x + \xi/2, y + \eta/2)u^*(x - \xi/2, y - \eta/2) \rangle \\ &\quad \times T(x + \xi/2 - s, y + \eta/2 - t)T^*((x - \xi/2 - s, y - \eta/2 - t) \\ &\quad \exp\{-i2\pi(u\xi + v\eta)\}dxdy d\xi d\eta \end{aligned} \quad (4.18)$$

where $x = (x_1 + x_2)/2$, $\xi = x_1 - x_2$, $y = (y_1 + y_2)/2$, $\eta = y_1 - y_2$. By invoking the convolution theorem, we can rewrite Equation (4.18) as the convolution of two Wigner distributions:

$$\begin{aligned} \mathcal{W}_{obs}(s, t, u, v) &= \iint \mathcal{W}_u(x, y, u, v) *_{u,v} \mathcal{W}_T(x - s, y - t, u, v)dxdy \\ &= \mathcal{W}_u(s, t, u, v) *_{s,t,u,v} \mathcal{W}_T(-s, -t, u, v) \end{aligned} \quad (4.19)$$

Therefore, the measurable quantity (the observable light field) is equivalent to the WDF of the scalar field blurred by the spatially inverted WDF of the aperture transmission function.

4.2 Wave optics analysis of light field imaging

A wave optics derivation of the light field imaging system is carried out in this section. The paraxial approximation is adopted through out. For simplicity, the equations are presented in one dimension; extension to 2D is straightforward.

4.2.1 Field at the sensor plane

The light field imaging arrangement is shown in Figure 4-6. The object plane is x_{in} . A pupil mask, g_{PM} , is assumed to be placed in front of the field lens. A lens, having a focal length f , is at x' . The microlens array is at x'' , with each microlens having a focal length of f_m and diameter Λ . The sensor or output plane is denoted as x_{out} . The distances between these planes are z_1 , z_2 , and z_3 , as shown in the figure.

To derive the field at the sensor plane, an input field $g_{in}(x_{in})$ is assumed at the

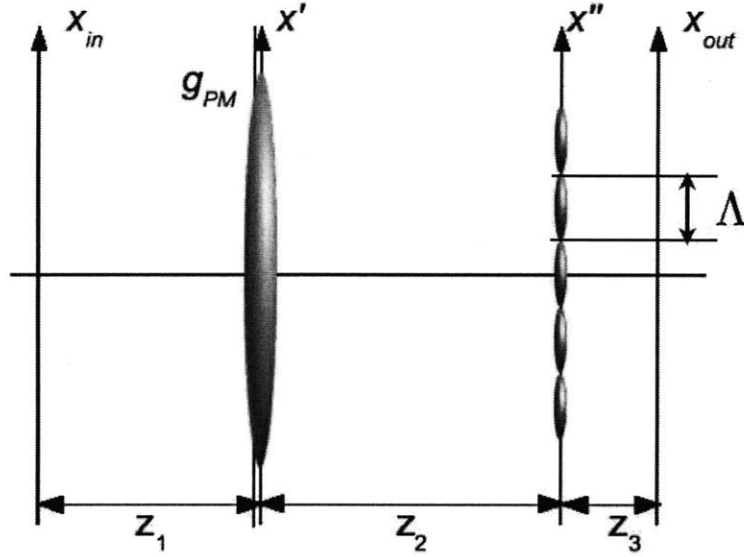


Figure 4-6: Light field imaging system setup.

input plane. After propagating through the field lens and the microlens array, the resultant field is recorded by a sensor. Starting from the input field $g_{in}(x_{in})$, after propagating to the plane immediately before the aperture stop, the field becomes $g_-(x')$. The propagation is computed through the Fresnel approximation,

$$g_-(x') = \int dx_{in} g_{in}(x_{in}) \exp \left\{ i \frac{\pi}{\lambda z_1} (x' - x_{in})^2 \right\}. \quad (4.20)$$

The field immediately after the field lens is

$$g_+(x') = g_-(x') g_{PM}(x') \exp \left\{ -i \pi \frac{x'^2}{\lambda f} \right\}. \quad (4.21)$$

The field immediately before the microlens array is

$$g_-(x'') = \int dx' g_+(x') \exp \left\{ i \frac{\pi}{\lambda z_2} (x'' - x')^2 \right\}. \quad (4.22)$$

Let

$$\psi_1 = \frac{1}{z_1} + \frac{1}{z_2} - \frac{1}{f} \quad (4.23)$$

denote the amount of defocus. Combining Equations (4.20)–(4.23), $g_-(x'')$ can be

rewritten as

$$g_-(x'') = \exp \left\{ i\pi \frac{x''^2}{\lambda z_2} \right\} \iint dx_{\text{in}} dx' g_{\text{in}}(x_{\text{in}}) \exp \left\{ i\pi \frac{x_{\text{in}}^2}{\lambda z_1} \right\} g_{PM}(x') \\ \exp \left\{ i\pi \frac{\psi_1 x'^2}{\lambda} \right\} \exp \left\{ -i2\pi \frac{x'}{\lambda} \left(\frac{x_{\text{in}}}{z_1} + \frac{x''}{z_2} \right) \right\}. \quad (4.24)$$

The transmittance function of the microlens array is

$$g_{ml}(x'') = \sum_{k=-l}^l \text{rect} \left(\frac{x'' - k\Lambda}{\Lambda} \right) \exp \left\{ -i\pi \frac{(x'' - k\Lambda)^2}{\lambda f_m} \right\}, \quad (4.25)$$

where $\text{rect}(\bullet)$ denotes a rectangular function, whose size is given by the diameter Λ of each lenslet. The total number of the microlenses are assumed to be $2l + 1$, so the system is symmetrical about the central lenslet.

The field immediately behind the microlens array is

$$g_+(x'') = g_-(x'') g_{ml}(x''). \quad (4.26)$$

The field at the output plane is

$$g_{\text{out}}(x_{\text{out}}) = \int dx'' g_+(x'') \exp \left\{ i\pi \frac{(x_{\text{out}} - x'')^2}{\lambda z_3} \right\}, \quad (4.27)$$

denoting

$$\psi_2 = \frac{1}{z_2} + \frac{1}{z_3} - \frac{1}{f_m}, \quad (4.28)$$

$g_{\text{out}}(x_{\text{out}})$ can be written as

$$g_{\text{out}}(x_{\text{out}}) = \exp \left\{ i\pi \frac{x_{\text{out}}^2}{\lambda z_3} \right\} \sum_{k=-l}^l \iiint dx_{\text{in}} dx' dx'' g_{\text{in}}(x_{\text{in}}) \exp \left\{ i\pi \frac{x_{\text{in}}^2}{\lambda z_1} \right\} \\ g_{PM}(x') \exp \left\{ i\pi \frac{\psi_1 x'^2}{\lambda} \right\} \exp \left\{ -i2\pi \frac{x'}{\lambda} \left(\frac{x_{\text{in}}}{z_1} + \frac{x''}{z_2} \right) \right\} \exp \left\{ i\pi \frac{\psi_2 x''^2}{\lambda} \right\} \\ \exp \left\{ i2\pi \frac{x''}{\lambda} \left(\frac{k\Lambda}{f_m} - \frac{x_{\text{out}}}{z_3} \right) \right\} \text{rect} \left(\frac{x'' - k\Lambda}{\Lambda} \right) \exp \left\{ -i\pi \frac{(k\Lambda)^2}{\lambda f_m} \right\}. \quad (4.29)$$

4.2.2 Coherent Point Spread Function

From Equation (4.29), we can derive the coherent point spread function (cPSF) of the system. By assuming the object is a point object at x_0 , and dropping the constant phase terms,

$$\begin{aligned}
\text{cPSF}(x_{\text{out}}) &= \sum_{k=-l}^l \iint dx' dx'' g_{PM}(x') \exp \left\{ i\pi \frac{\psi_1 x'^2}{\lambda} \right\} \\
&\exp \left\{ -i2\pi \frac{x'}{\lambda} \left(\frac{x_0}{z_1} + \frac{x''}{z_2} \right) \right\} \exp \left\{ i\pi \frac{\psi_2 x''^2}{\lambda} \right\} \text{rect} \left(\frac{x'' - k\Lambda}{\Lambda} \right) \\
&\exp \left\{ i2\pi \frac{x''}{\lambda} \left(\frac{k\Lambda}{f_m} - \frac{x_{\text{out}}}{z_3} \right) \right\} \exp \left\{ -i\pi \frac{(k\Lambda)^2}{\lambda f_m} \right\}. \quad (4.30)
\end{aligned}$$

4.2.3 Incoherent Point Spread Function

The relationship between the cPSF and the incoherent point spread function (iPSF) is given by

$$\begin{aligned}
\text{iPSF}(x_{\text{out}}) &= |\text{cPSF}(x_{\text{out}})|^2 \quad (4.31) \\
&= \sum_{k_1=-l}^l \iint dx'_1 dx''_1 g_{PM}(x'_1) \exp \left\{ i\pi \frac{\psi_1 x'^2_1}{\lambda} \right\} \exp \left\{ -i2\pi \frac{x'_1}{\lambda} \left(\frac{x_0}{z_1} + \frac{x''_1}{z_2} \right) \right\} \\
&\text{rect} \left(\frac{x''_1 - k_1\Lambda}{\Lambda} \right) \exp \left\{ i\pi \frac{\psi_2 x''^2_1}{\lambda} \right\} \exp \left\{ i2\pi \frac{x''_1}{\lambda} \left(\frac{k_1\Lambda}{f_m} - \frac{x_{\text{out}}}{z_3} \right) \right\} \\
&\exp \left\{ -i\pi \frac{(k_1\Lambda)^2}{\lambda f_m} \right\} \times \\
&\sum_{k_2=-l}^l \iint dx'_2 dx''_2 g_{PM}^*(x'_2) \exp \left\{ -i\pi \frac{\psi_1 x'^2_2}{\lambda} \right\} \exp \left\{ i2\pi \frac{x'_2}{\lambda} \left(\frac{x_0}{z_1} + \frac{x''_2}{z_2} \right) \right\} \\
&\text{rect} \left(\frac{x''_2 - k_2\Lambda}{\Lambda} \right) \exp \left\{ -i\pi \frac{\psi_2 x''^2_2}{\lambda} \right\} \exp \left\{ -i2\pi \frac{x''_2}{\lambda} \left(\frac{k_2\Lambda}{f_m} - \frac{x_{\text{out}}}{z_3} \right) \right\} \\
&\exp \left\{ i\pi \frac{(k_2\Lambda)^2}{\lambda f_m} \right\}. \quad (4.32)
\end{aligned}$$

Using a change of variables,

$$\begin{aligned}
x' &= (x'_1 + x'_2)/2, & \xi' &= x'_1 - x'_2, \\
x'' &= (x''_1 + x''_2)/2, & \xi'' &= x''_1 - x''_2
\end{aligned} \quad (4.33)$$

the iPSF can be rewritten as

$$\begin{aligned}
\text{iPSF}(x_{\text{out}}) &= \iint dx' dx'' \mathcal{W}_{g_{PM}} \left(x', \frac{\psi_1 x'}{\lambda} - \frac{x''}{\lambda z_2} - \frac{x_0}{\lambda z_1} \right) \\
&\quad \sum_{k_1=-l}^l \sum_{k_2=-l}^l \int d\xi'' \text{rect} \left(\frac{x'' + \xi''/2 - k_1 \Lambda}{\Lambda} \right) \text{rect} \left(\frac{x'' - \xi''/2 - k_2 \Lambda}{\Lambda} \right) \\
&\quad \exp \left\{ i2\pi \left(\frac{\psi_2 x''}{\lambda} - \frac{x_{\text{out}}}{\lambda z_3} - \frac{x'}{\lambda z_2} + \frac{\Lambda}{\lambda f_m} \frac{(k_1 + k_2)}{2} \right) \xi'' \right\} \\
&\quad \exp \left\{ i2\pi \frac{(k_1 - k_2)\Lambda}{\lambda f_m} \left(x'' - \frac{(k_1 + k_2)\Lambda}{2} \right) \right\}, \tag{4.34}
\end{aligned}$$

where $\mathcal{W}_{g_{PM}}$ is the WDF of the pupil mask function

$$\mathcal{W}_{g_{PM}}(x, u) = \int d\xi g_{PM}(x + \xi/2) g_{PM}^*(x - \xi/2) \exp \{ i2\pi u \xi \}, \tag{4.35}$$

and k_1 and k_2 are indices for the microlenses. Equation (4.34) can be simplified by introducing

$$k_+ = k_1 + k_2, \quad k_- = k_1 - k_2. \tag{4.36}$$

The values of k_+ and k_- need to satisfy the following conditions:

$$\begin{aligned}
k_1 &= (k_+ + k_-)/2, \quad k_2 = (k_+ - k_-)/2, \\
-l &\leq k_1, k_2 \leq l, \quad k_1 \text{ and } k_2 \text{ are integers.} \tag{4.37}
\end{aligned}$$

We rewrite Equation (4.34) as

$$\begin{aligned}
\text{iPSF}(x_{\text{out}}) &= \iint dx' dx'' \mathcal{W}_{g_{PM}} \left(x', \frac{\psi_1 x'}{\lambda} - \frac{x''}{\lambda z_2} - \frac{x_0}{\lambda z_1} \right) \\
&\quad \sum_{k_-} \sum_{k_+} \mathcal{W}_{\text{rect}(\frac{x}{\Lambda})} \left(x'' - \frac{k_+ \Lambda}{2}, \frac{\psi_2 x''}{\lambda} - \frac{x_{\text{out}}}{\lambda z_3} - \frac{x'}{\lambda z_2} + \frac{k_+ \Lambda}{2\lambda f_m} \right) \\
&\quad \exp \left\{ i2\pi \left(\frac{\psi_2 x''}{\lambda} - \frac{x_{\text{out}}}{\lambda z_3} - \frac{x'}{\lambda z_2} + \frac{x''}{\lambda f_m} \right) k_- \Lambda \right\}, \tag{4.38}
\end{aligned}$$

where $\mathcal{W}_{\text{rect}(\frac{x}{\Lambda})}$ is the WDF of the rect function,

$$\mathcal{W}_{\text{rect}(\frac{x}{\Lambda})}(x, u) = \int d\xi \text{rect}\left(\frac{x + \xi/2}{\Lambda}\right) \text{rect}\left(\frac{x - \xi/2}{\Lambda}\right) \exp\{i2\pi u\xi\}, \quad (4.39)$$

and k_+ and k_- satisfy the conditions in Equation (4.37).

The result of Equation (4.38) can be further evaluated for a few special cases. Assume that the object plane is conjugate to the microlens array plane, so the defocus term ψ_1 vanishes. In addition, assume that the pupil mask is a clear aperture and the diameter of the field lens is A , which is much larger than the size of the microlens Λ . The limiting case of $A \rightarrow +\infty$ will be considered. Then

$$g_{PM} = 1, \quad (4.40)$$

whose WDF is a δ -function,

$$\mathcal{W}_{g_{PM}} = \delta(u). \quad (4.41)$$

In addition, assume the field lens plane is conjugate to the sensor plane as in [47, 66], so $\psi_2 = 0$.

Substituting the above assumptions, we can rewrite Equation (4.38) as

$$\begin{aligned} \text{iPSF}(x_{\text{out}}) &= \sum_{k_-} \sum_{k_+} \iint dx' dx'' \delta\left(-\frac{x''}{\lambda z_2} - \frac{x_0}{\lambda z_1}\right) \\ &\exp\left\{i2\pi\left(-\frac{x_{\text{out}}}{\lambda z_3} - \frac{x'}{\lambda z_2} + \frac{x''}{\lambda f_m}\right)k_- \Lambda\right\} \\ &\mathcal{W}_{\text{rect}(\frac{x}{\Lambda})}\left(x'' - \frac{k_+ \Lambda}{2}, -\frac{x_{\text{out}}}{\lambda z_3} - \frac{x'}{\lambda z_2} + \frac{k_+ \Lambda}{2\lambda f_m}\right). \end{aligned} \quad (4.42)$$

Note that solving the argument of the δ -function gives the position of the image point at the microlens plane,

$$x_0'' = -\frac{z_2}{z_1} x_0. \quad (4.43)$$

Furthermore, since $\text{rect}(x/\Lambda)$ is non-zero only when $|x| < \Lambda/2$, $\mathcal{W}_{\text{rect}(x/\Lambda)}$ has the same spatial support. As a result, in Equation (4.42), k_+ can be determined by solving the

inequality,

$$\left| x_0'' - \frac{k_+\Lambda}{2} \right| < \frac{\Lambda}{2}, \quad (4.44)$$

and only one index, denoted by k_0 , satisfies this condition. Using this fact, the iPSF is further simplified as

$$\begin{aligned} \text{iPSF}(x_{\text{out}}) &= \sum_{k_-} \int dx' \mathcal{W}_{\text{rect}(\frac{\pi}{\Lambda})} \left(x_0'' - \frac{k_0\Lambda}{2}, -\frac{x_{\text{out}}}{\lambda z_3} - \frac{x'}{\lambda z_2} + \frac{k_0\Lambda}{2\lambda f_m} \right) \\ &\quad \exp \left\{ i2\pi \left(-\frac{x_{\text{out}}}{\lambda z_3} - \frac{x'}{\lambda z_2} + \frac{x_0''}{\lambda f_m} \right) k_- \Lambda \right\}. \end{aligned} \quad (4.45)$$

In order to simplify Equation (4.45) even further, let

$$\begin{aligned} u &= -\frac{x_{\text{out}}}{\lambda z_3} - \frac{x'}{\lambda z_2} + \frac{k_0\Lambda}{2\lambda f_m}, \\ x_s &= x_0'' - \frac{k_0\Lambda}{2}, \\ \alpha_s &= \frac{2\pi k_- \Lambda}{\lambda f_m} \left(x_0'' - \frac{k_0\Lambda}{2} \right). \end{aligned} \quad (4.46)$$

Substituting Equation (4.46) into Equation (4.45), the iPSF takes the form

$$\text{iPSF}(x_{\text{out}}) = \lambda z_2 \sum_{k_-} \exp(i\alpha_s) \int du \mathcal{W}_{\text{rect}(\frac{\pi}{\Lambda})}(x_s, u) \exp(i2\pi u k_- \Lambda). \quad (4.47)$$

Since

$$\int du \mathcal{W}_f(x_s, u) \exp(i2\pi u k_- \Lambda) = f\left(x_s + \frac{k_- \Lambda}{2}\right) f^*\left(x_s - \frac{k_- \Lambda}{2}\right), \quad (4.48)$$

and $f(x) = \text{rect}(x/\Lambda)$, Equation (4.48) is non-zero only if

$$k_- = 0. \quad (4.49)$$

Recalling the conditions of (4.37), $k_- = 0$ implies

$$\begin{aligned} k_0 &\in [-2l, -2l+2, \dots, 0, 2, \dots, 2l-2, 2l], \\ \text{or, } k_0/2 &\in [-l, -l+1, \dots, 0, 1, \dots, l-1, l]. \end{aligned} \quad (4.50)$$

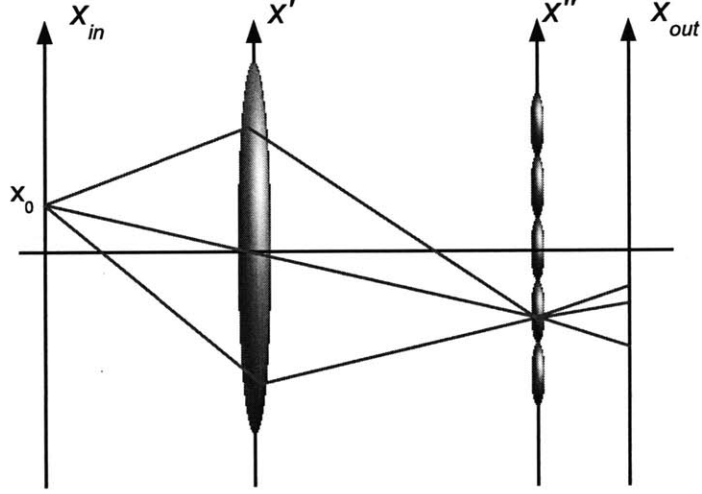


Figure 4-7: Illustration of the incoherent point spread function of the light field imaging system.

Thus, $k_0/2$ only takes integer values, and will be denoted by k_l hereafter.

The physical meaning of Equation (4.49) is that there is no cross-talk between the field after neighboring microlenses. Under this condition, Equation (4.50) suggests that spatial samples are discretized by the position of the centers of the microlenses. Because when $k_0/2 = n$, n is an integer, the spatial samples take discrete values, $n\Lambda$, which corresponds to the positions of the centers of the microlenses.

Substituting $k_- = 0$ and $k_0/2 = k_l$ into Equation (4.45), the expression for the iPSF becomes

$$\begin{aligned} \text{iPSF}(x_{\text{out}}) &= \int dx' \mathcal{W}_{\text{rect}(\frac{x}{\Lambda})} \left(-\frac{z_2}{z_1} x_0 - k_l \Lambda, \frac{k_l \Lambda}{\lambda f_m} - \frac{x_{\text{out}}}{\lambda z_3} - \frac{x'}{\lambda z_2} \right), \\ &= \begin{cases} 1 & \text{if } (k_l - 1/2)\Lambda < -(z_2/z_1)x_0 < (k_l + 1/2)\Lambda, \\ 0 & \text{otherwise,} \end{cases} \end{aligned} \quad (4.51)$$

and the mapping from the output coordinate x_{out} to the spatial frequency u is given by

$$u = \frac{k_l \Lambda}{\lambda f_m} - \frac{x_{\text{out}}}{\lambda z_3} - \frac{x'}{\lambda z_2}. \quad (4.52)$$

The results of Equation (4.51) are illustrated by Figure 4-7. A point object at x_0 is imaged onto the k_l^{th} microlens. Its spatial frequency components, which correspond

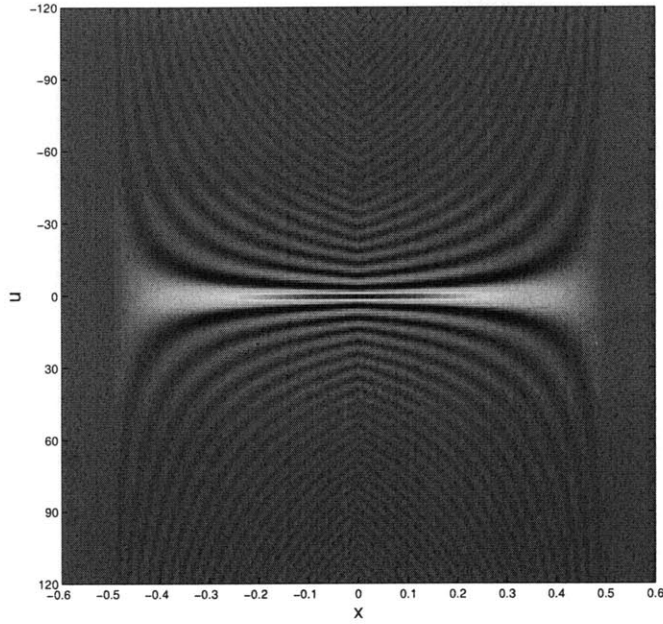


Figure 4-8: Wigner distribution function of a rect function. The spatial coordinates are normalized by the width of the rect function.

to different rays in fig 4-7, are sampled at different locations on the sensor plane, x_{out} . Equation (4.52) should be used to find the mapping between the spatial frequency and the corresponding sampling pixel on the sensor plane.

Sampling in spatial frequency domain

The sampling in spatial frequency domain can be further analyzed using the properties of the WDF of the rect function in Equation (4.51), which is

$$\mathcal{W}_{\text{rect}(x/\Lambda)}(x, u) = 2\Lambda \text{tri}[x/(\Lambda/2)] \text{sinc}\{(2\Lambda - 4|x|)u\}, \quad (4.53)$$

where $\text{tri}(\bullet)$ is a triangle function and $\text{sinc}(x) = \sin(x)/x$ is the sinc function. Figure 4-8 shows the WDF of a rect function.

I. Information spreads out as a sinc function.

If a single “ray” is chosen by fixing x' in Equation (4.51), or equivalently a single

spatial frequency component by fixing u in Equation (4.53), it results in a sinc-shaped intensity distribution at the sensor plane, as shown in Figure 4-9(a). Each pixel of the sensor integrates the intensities from multiple spatial frequency components, resulting a unit output, as in Equation (4.51).

The width of the main lobe of the sinc function is

$$w_f = 1/(\Lambda - 2|x_l|), \quad (4.54)$$

where x_l indicates the position of the image point (the center of the image of a point object in a strict sense) on the microlens relative to the center of this microlens and is given by

$$x_l = -(z_2/z_1)x_0 - k_l\Lambda \quad (4.55)$$

The dependence of w_f on x_l suggests that the spreading of the sinc-shaped spatial frequency samples depend on the position of their corresponding image points on the microlens plane, as illustrated in Figure 4-9. In Figure 4-9 (a), the red image point, which is near the center of a microlens, produces narrower sinc-shaped spatial frequency samples. In Figure 4-9 (b), the majority of the energy from a spatial frequency sample is measured by an individual pixel (the gray blocks in the figure). The blue image point in Figure 4-9 (a) is near the edge of a microlens. It produces much wider sinc-shaped spatial frequency samples. Each spatial frequency sample needs multiple pixels to measure the majority of its energy. As a result, the resulting pixel value is a combination of several nearby spatial frequency samples, as shown in Figure 4-9(c).

In section 4.1.3, the measurable Wigner distribution, or the observable light field, is shown to be a blurred version of the object WDF. The blurring effect is due to a convolution with the WDF of an aperture function. Later it will be shown that the blurring effect is equivalent to the mixing of the spatial frequency samples discussed in this section.

II. The center of the sinc-shaped spatial frequency sample can be calculated by letting $u = 0$ in Equation (4.53). Recalling that u is given by Equation (4.52), it

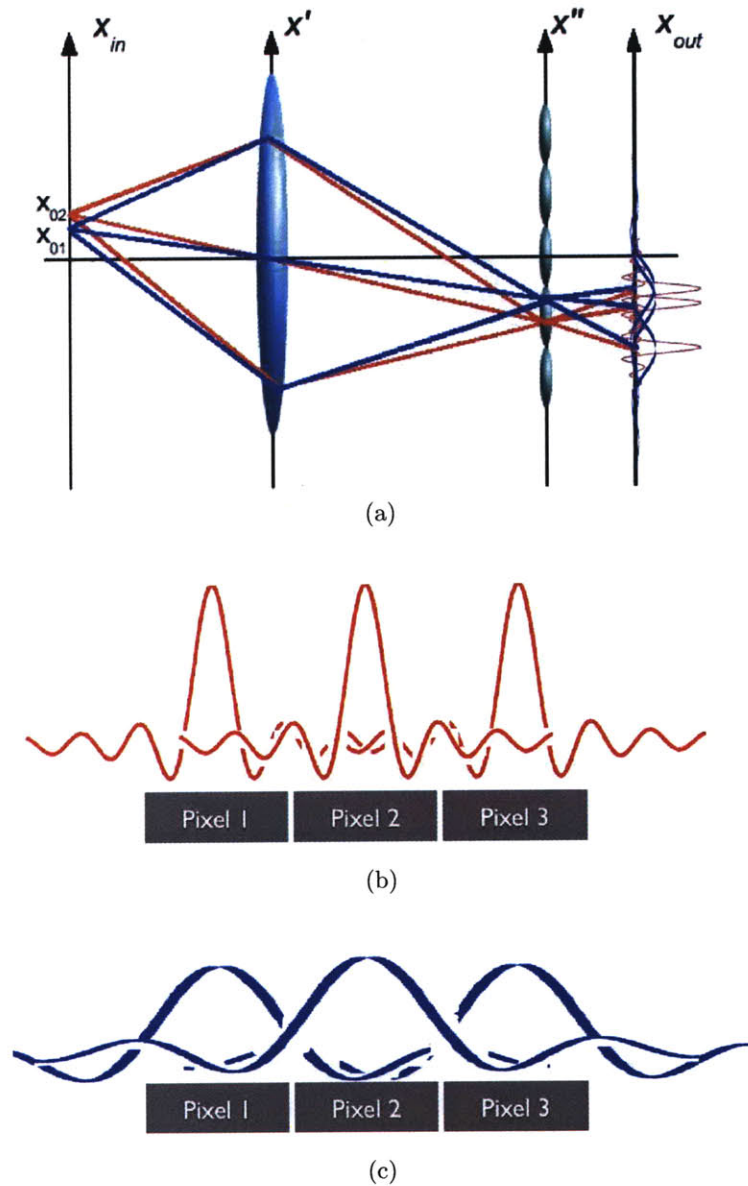


Figure 4-9: (a) A single spatial frequency component produces a sinc-shaped intensity distribution on the sensor plane. The red image point near the center of the microlens produces narrower sinc; and the blue image point near the edge of the microlens produces much wider sinc. (b) Spatial frequency sample of the red image point in (a) can be measured by an individual pixel (the gray blocks in the figure). (c) Spatial frequency sample of the blue image point in (a) spreads over multiple pixels. The resulting pixel value includes energy from several nearby spatial frequency samples.

gives the position of the center at the sensor plane

$$x_{\text{out}} = -\frac{z_3}{z_2}(x' - k_0\Lambda) + k_0\Lambda, \quad (4.56)$$

which is the same as the result predicted by geometrical optics.

III. The resolution in the spatial frequency domain can be measured as the width of the main lobe (w_f) of the sinc function. Since w_f is on the order of $1/\Lambda$, the spatial frequency resolution R_f of the system is on the order of $1/\Lambda$. The spatial frequency samples are recorded at the sensor plane, so the spatial frequency resolution can also be calculated in terms of x_{out} . Equation (4.52) suggests that u is mapped to $x_{\text{out}}/\lambda z_3$, so

$$R_f^{x_{\text{out}}} \sim \lambda/\text{NA}_m, \quad (4.57)$$

where $R_f^{x_{\text{out}}}$ is the spatial frequency resolution calculated in terms of x_{out} , and NA_m is the image side numerical aperture of the microlens and is given by

$$\text{NA}_m = \Lambda/2z_3. \quad (4.58)$$

A continuous sampling on the sensor plane is assumed when deriving Equation (4.57). In reality, all sensors are discretized by pixels. If the pixel size is smaller than the width of the main lobe of the sinc, then the spatial frequency resolution given in Equation (4.57) can be achieved. In the opposite case, the spatial frequency resolution will be limited by the pixel size.

IV. Equation (4.56) relates the points on the sensor plane and their conjugate points on the field lens plane. With the non-overlapping requirement between neighboring sub-images under each microlens, the spreading of single sub-image should be confined by the size of each microlens (assuming no gaps between neighboring microlenses):

$$|x_{\text{out}} - k_0\Lambda| \leq \Lambda/2. \quad (4.59)$$

Considering the most efficient use of the spatial frequency support of both the field lens and the microlens, the marginal ray from the field lens should reach the edge of

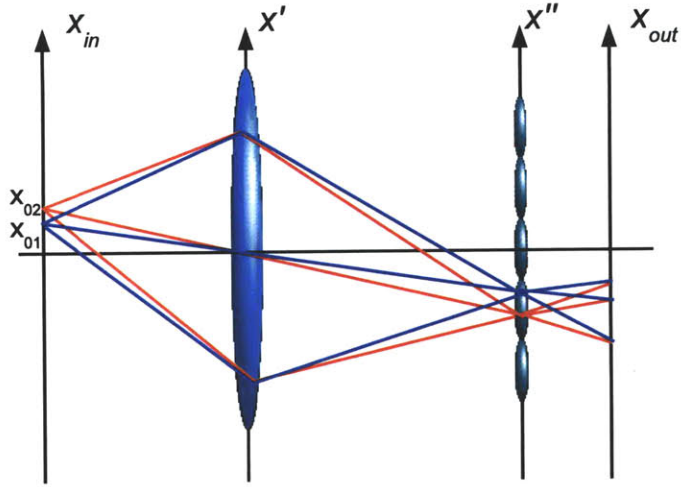


Figure 4-10: Illustration of incoherent point spread function. Two point objects x_{01} and x_{02} are imaged onto the same microlens and their spatial frequency components corresponding to the same x' are mapped to the same pixel on the output plane.

each sub-image, so

$$\frac{z_3}{z_2}(A/2) = (\Lambda/2). \quad (4.60)$$

This gives the optimum design requirement of the field lens and the microlens,

$$NA_m = NA_c, \quad (4.61)$$

where $NA_c = A/2z_2$ is the image side numerical aperture of the field lens. Result (4.61), i.e. matching the numerical aperture of the field and the microlens, is intuitively satisfying.

Sampling in space domain

As seen in Equation (4.51), all object points which satisfy

$$\left| -\frac{z_2}{z_1}x + k_l\Lambda \right| < \frac{\Lambda}{2} \quad (4.62)$$

will be imaged onto the same microlens. In addition, the center of the sinc-shaped spatial frequency samples of these points overlap on the sensor plane since Equation

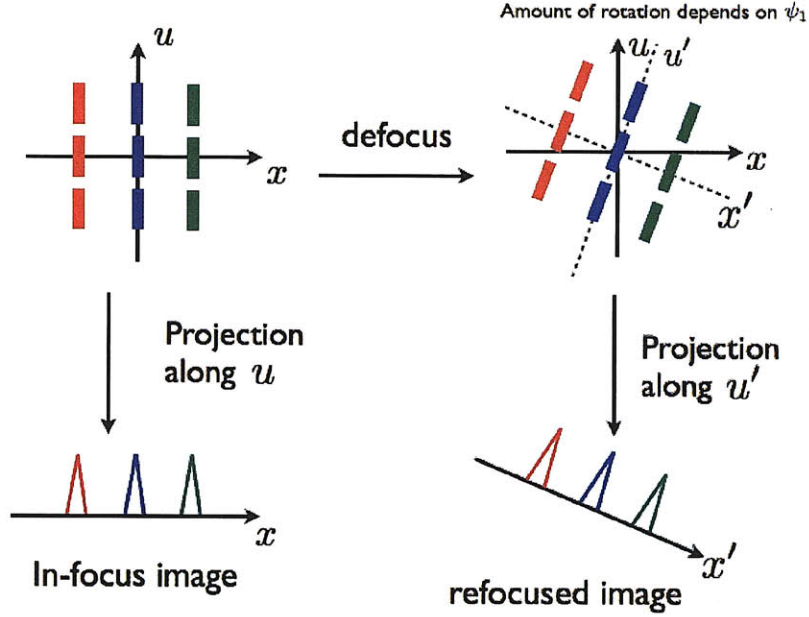


Figure 4-11: Digital processing to compute the image of the in-focus object (the left figure) and digitally refocus to the defocused object (the right figure).

(4.56) is independent of x_0 . As a result, the spatial resolution is the size of each microlens, Λ . This is shown in fig 4-10, where two point objects x_{01} and x_{02} are imaged onto the same microlens and their spatial frequency components corresponding to the same x' are mapped to the same pixel on the output plane.

Digital refocusing

To study the digital refocusing capability of the light field system, the output of defocused object, by letting $\psi_1 \neq 0$, should be studied. Neglecting the cross-talk between the field after nearby microlenses, the defocused iPSF, iPSF_d , can be derived from Equation (4.38),

$$\text{iPSF}_d(x_{\text{out}}) = \sum_{k=-l}^l \int dx' \mathcal{W}_{\text{rect}(\frac{x}{\Lambda})} \left(z_2 \psi_1 x' - \frac{z_2}{z_1} x_{\text{in}} - k\Lambda, -\frac{x_{\text{out}} - k\Lambda}{\lambda z_3} - \frac{x' - k\Lambda}{\lambda z_2} \right) \quad (4.63)$$

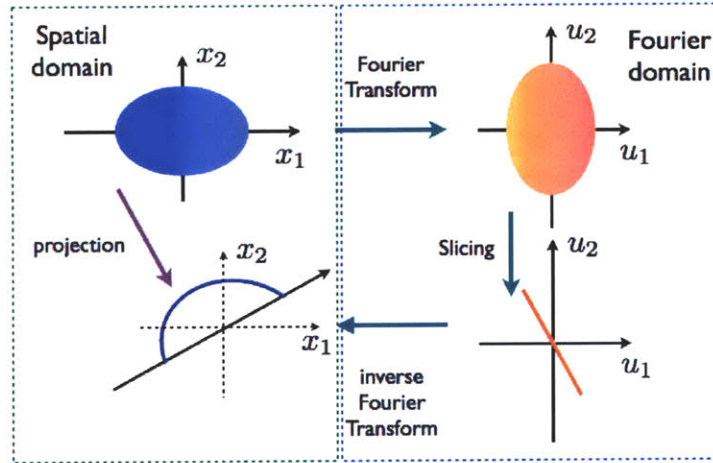


Figure 4-12: The Fourier Slicing Theorem. A projection taken along a certain direction is equivalent to taking a slice of the 2D Fourier transform along the same direction.

Equation (4.63) is a Fractional Fourier Transform (FrFT), with the defocus ψ_1 determining the fractional power [50]. Digital refocusing [65, 66] can be achieved by integrating the samples over the spatial frequency variable (equivalently, over x_{out}). Figure 4-11 shows how to compute an image from the data obtained from a light field imaging system. The intensity of an object is computed by projecting the data along the spatial frequency axis. Defocusing is equivalent to a rotation in the Wigner space, where the amount of rotation depends on the defocus. To digitally refocus to the image, a projection along the rotated spatial frequency axis, u' , is carried out. Instead of computing a projection directly, the Fourier Slicing Theorem [38] can be applied, which results in a more efficient computation [76]. The schematic diagram of the Fourier Slicing Theorem is shown in Figure 4-12. A projection of the Wigner distribution taken along a certain direction, which depends on the amount of defocus, can be implemented in the Ambiguity space. First, take a 4D Fourier transform of the WDF, which transforms it to its Fourier conjugate, the Ambiguity space. Next, take a slice of the ambiguity function along the same direction. Finally, take an 2D inverse Fourier transform on the Ambiguity function slice, which results in the projection in the Wigner space.

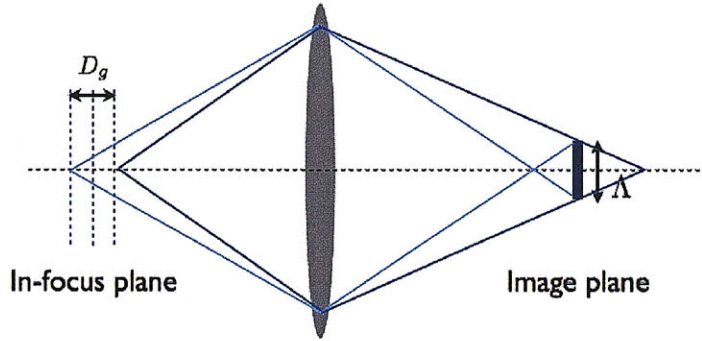


Figure 4-13: Geometrical defocus. Within the range D_g , all object point will be imaged onto the same pixel, Λ .

Depth of focus

Two terms contribute to the depth of focus (DoF) of the system, D . The size of the microlens results in a defocus range, D_g , which can be calculated by geometrical optics, as illustrated in Figure 4-13. The second term is due to the diffraction, D_d . The DoF can be approximated by the sum of these two terms,

$$D = D_g + D_d = \frac{\Lambda}{M \cdot \text{NA}} + \frac{\lambda}{\text{NA}^2}, \quad (4.64)$$

where M is the magnification, $M = z_2/z_1$ and NA is the object side numerical aperture of the field lens, $\text{NA} = A/2z_1$.

4.2.4 Partially coherent imaging using a light field imaging system

Up to here, the incoherent and coherent imaging using a light field imaging system have been discussed. In practice, the illumination is always partially coherent. Partially coherent imaging in a light field imaging system will be discussed in this section. Partially coherent light can be described by a temporally stationary stochastic process $g(x, t)$; the ensemble average of the product $g(x_1, t_1)g^*(x_2, t_2)$ is then a function

of the time difference $t_1 - t_2$:

$$\langle g(x_1, t_1)g^*(x_2, t_2) \rangle = \Gamma(x_1, x_2, t_1 - t_2), \quad (4.65)$$

where $\langle \bullet \rangle$ denotes the ensemble average. The function $\Gamma(x_1, x_2, t_1 - t_2)$ is known as the coherence function. Using the ergodicity and quasi-monochromaticity assumptions, the coherence function is sufficiently described by the mutual intensity J , defined as the coherence function at zero time delay:

$$J(x_1, x_2) = \langle g(x_1)g^*(x_2) \rangle \quad (4.66)$$

The mutual intensity at the sensor plane can be calculated by substituting the field in Equation (4.29) into Equation (4.66):

$$J(x_1, x_2) = \langle g_{\text{out}}(x_1)g_{\text{out}}^*(x_2) \rangle. \quad (4.67)$$

and the output intensity is

$$I(x) = J(x, x) = |g_{\text{out}}(x)|^2. \quad (4.68)$$

The intensity can be written as

$$\begin{aligned} I(x_{\text{out}}) = & \iiint dx_{\text{in}} dx' dx'' \mathcal{W}_{g_{\text{in}}} \left(x_{\text{in}}, \frac{x_{\text{in}} - x'}{\lambda z_1} \right) \mathcal{W}_{g_{PM}} \left(x', \frac{\psi_1 x'}{\lambda} - \frac{x''}{\lambda z_2} - \frac{x_{\text{in}}}{\lambda z_1} \right) \\ & \sum_{k_-} \sum_{k_+} \mathcal{W}_{\text{rect}(\frac{x}{\Lambda})} \left(x'' - \frac{k_+ \Lambda}{2}, \frac{\psi_2 x''}{\lambda} - \frac{x_{\text{out}}}{\lambda z_3} - \frac{x'}{\lambda z_2} + \frac{k_+ \Lambda}{2\lambda f_m} \right) \\ & \exp \left\{ i2\pi \left(\frac{\psi_2 x''}{\lambda} - \frac{x_{\text{out}}}{\lambda z_3} - \frac{x'}{\lambda z_2} + \frac{x''}{\lambda f_m} \right) k_- \Lambda \right\}, \end{aligned} \quad (4.69)$$

where the indices k_+ and k_- are defined in Equation (4.36) and satisfy the conditions in Equation (4.37). Again, assume a clear aperture, $g_{PM} = 1$, the object plane is conjugate to the microlens array plane, $\psi_1 = 0$, and the field lens plane and the sensor plane are conjugate planes, $\psi_2 = 0$ and no cross-talk between the fields behind

neighboring microlenses. So k_- equals to 0, and $k_+/2$ is restricted to integer values. The output intensity can be simplified as

$$I(x_{\text{out}}) = \sum_{k=-l}^l \iint dx_{\text{in}} dx' \mathcal{W}_{g_{\text{in}}} \left(x_{\text{in}}, \frac{x_{\text{in}} - x'}{\lambda z_1} \right) \mathcal{W}_{\text{rect}(\frac{x}{\Lambda})} \left(-\frac{z_2}{z_1} x_{\text{in}} - k\Lambda, -\frac{x_{\text{out}} - k\Lambda}{\lambda z_3} - \frac{x' - k\Lambda}{\lambda z_2} \right) \quad (4.70)$$

Equation (4.70) implies that light field imaging system samples the WDF of the object. It takes discrete spatial samples at the microlens plane, $k\Lambda$, and spatial frequency samples at the sensor plane, $(x_{\text{out}} - k\Lambda)/\lambda z_3$. The result is a blurred object WDF. The blurring is due to a convolution with the WDF of a rect function. A change of variables based on the physical implications makes this result evident. First, the spatial samples are discretized by the microlenses, with sampling rate Λ . As a result, the spatial frequency variables in $\mathcal{W}_{\text{rect}}$

$$\begin{aligned} u_1 &= (x' - k\Lambda)/\lambda z_2, \\ u_2 &= (k\Lambda - x_{\text{out}})/\lambda z_3 \end{aligned} \quad (4.71)$$

denote an input spatial frequency and an output spatial frequency, respectively. This can also be seen in Figure 4-14. Defining the magnification $m \equiv -z_2/z_1$, the spatial frequency variable in $\mathcal{W}_{g_{\text{in}}}$ can be rewritten as

$$\begin{aligned} \frac{x_{\text{in}} - x'}{\lambda z_1} &= \frac{x_{\text{in}} - k\Lambda}{\lambda z_1} + m u_1 \\ &= -\frac{k\Lambda}{\lambda z_1} - \frac{k\Lambda}{\lambda z_2} + m u_1. \end{aligned} \quad (4.72)$$

where the second equation is due to the approximation that $x_{\text{in}}/\lambda z_1 = -k\Lambda/\lambda z_3$. This approximation is valid because the spatial samples are discretized by the central

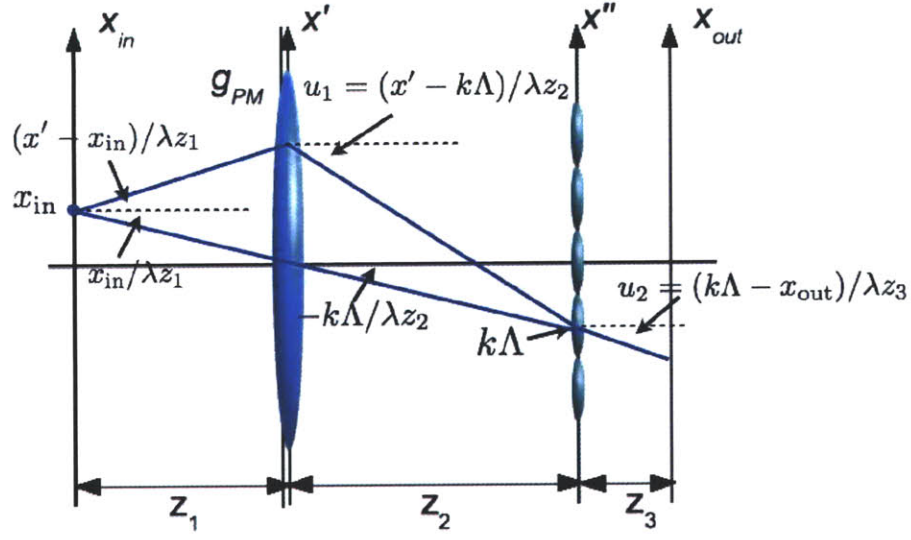


Figure 4-14: Illustration of input spatial frequency and output spatial frequency. Since spatial samples are discretized by the central positions of microlenses, it can be approximated that $x_{in}/\lambda z_1 = -k\Lambda/\lambda z_3$.

positions of the microlenses. So, Equation (4.70) takes the form

$$I(k\Lambda, u_2) = \sum_{k=-l}^l \iint dx_{in} du_1 \mathcal{W}_{g_{in}} \left(x_{in}, mu_1 - \frac{k\Lambda}{\lambda f} \right) \mathcal{W}_{\text{rect}(\frac{x}{\Lambda})} (-k\Lambda + mx_{in}, u_2 - u_1), \quad (4.73)$$

which can be seen as a double convolution between the WDF of the object and the WDF of a rect function. That is,

$$I(x, u) \sim \mathcal{W}_{g_{in}}(x, u) *_{x,u} \mathcal{W}_{\text{rect}(\frac{x}{\Lambda})}(x, u), \quad (4.74)$$

and the discretization in the space domain is realized by an integration for the same spatial sample

$$I(k\Lambda, u) = \int_{(k-1/2)\Lambda}^{(k+1/2)\Lambda} I(x, u) dx. \quad (4.75)$$

The result of Equation (4.74) is illustrated in Figure 4-15. The WDF of the object, \mathcal{W}_g , is space and spatial frequency limited due to the finite NA of the field

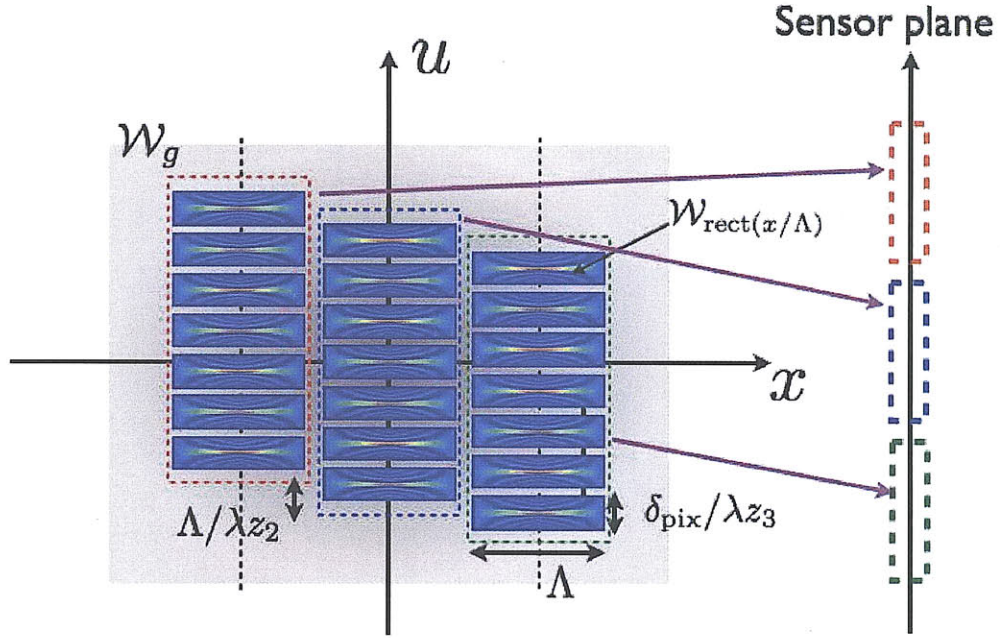
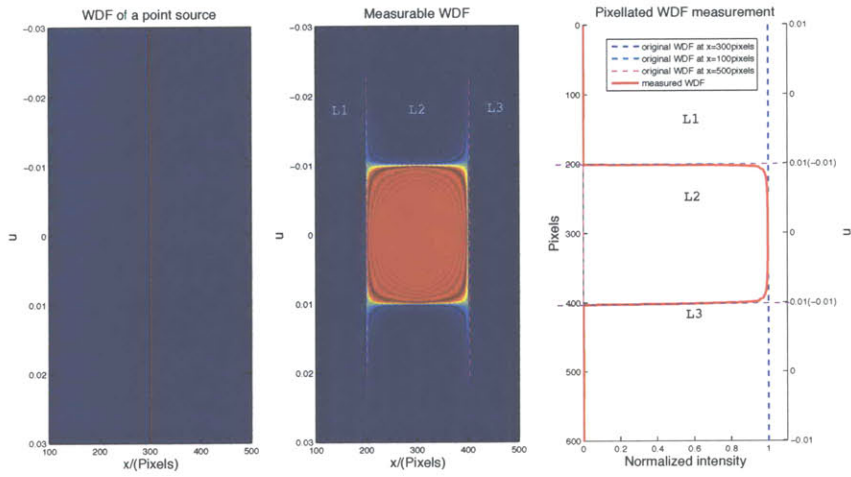
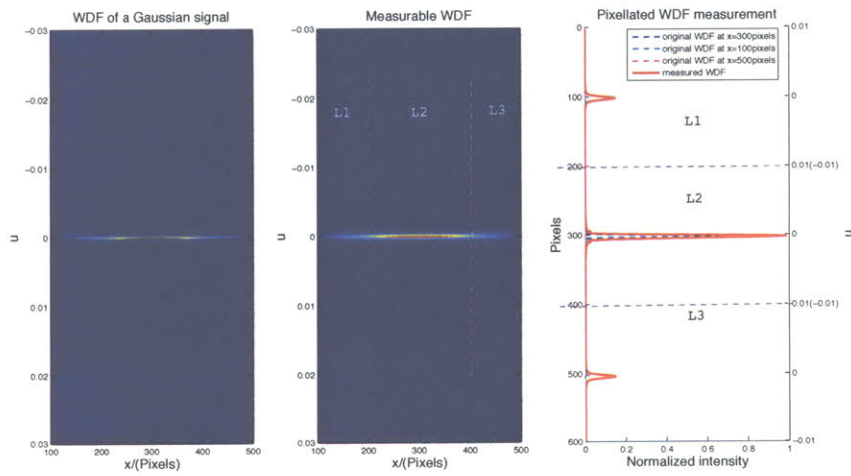


Figure 4-15: Sampling in the Wigner space by a light field imaging system. The object WDF is convolved with the WDF of a rect function. The convolution process is depicted as the replicas of the WDF of a rect function along both the spatial and spatial frequency axis directions. Three spatial samples are taken, depicted as three columns enclosed by dashed lines. Neighboring spatial samples are shifted by $\Lambda/\lambda z_2$ due to the physical displacements of different microlenses. 7 spatial frequency samples are taken at each position. Each spatial frequency sample has a width of $\delta_{\text{pix}}/\lambda z_3$, where δ_{pix} is the pixel size. The samples are recorded on a 1D sensor. The sample arrangement on the sensor is shown to the right.

lens, depicted as the grey area in the figure. The low-pass filtered object WDF is convolved with the WDF of a rect function. Each column enclosed by dashed lines corresponds to a microlens. The shift of the columns is due to the lateral displacement of the microlenses. The number of spatial frequency samples in a column is determined by the number of sensor pixels behind a microlens. The sample arrangement on the sensor plane is illustrated in the right-hand side of the figure.

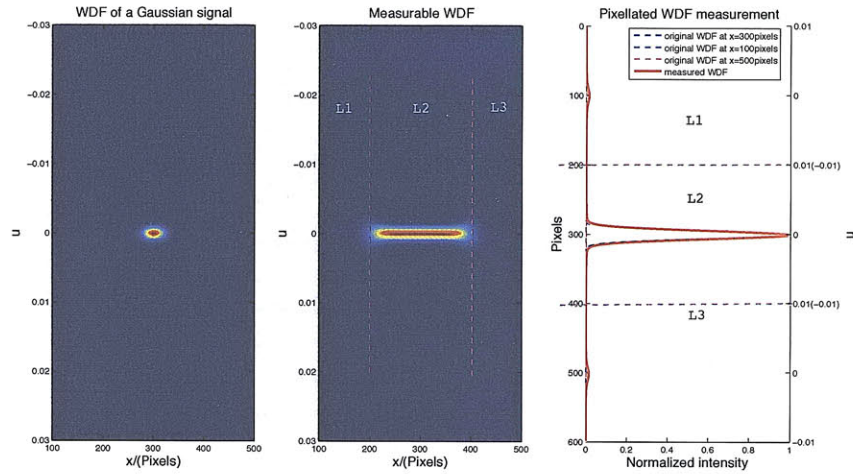


(a) Point object with infinite spatial frequency extent, its spatial frequency is cut off by the finite NA of the field lens

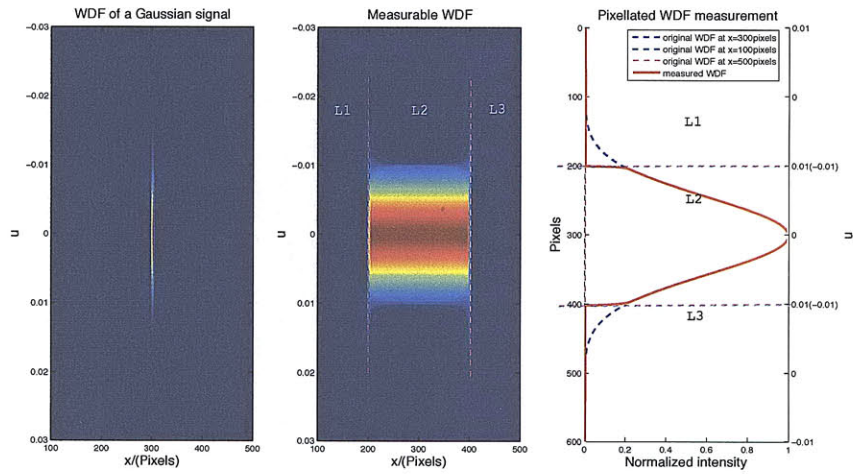


(b) Gaussian signal with large spatial extent

Figure 4-16



(c) Gaussian signal with intermediate space and spatial frequency extent.



(d) Gaussian signal with large spatial frequency extent. High frequency contents are cut off by the finite NA of the field lens.

Figure 4-16: Left: the original WDF of example object signals; middle: the measurable WDF, if continuous samples are taken in both space and spatial frequency; right: the resulting pixellated measurements (solid red line) and the original WDF (dashed lines). The three microlenses (L1, L2, and L3) discretize the measurable WDF into three columns. 200 spatial frequency samples are taken within each column. These three columns are rearranged side-by-side into a vector.

4.2.5 Simulation results

Simulations to better illustrate how a light field system measures the object Wigner distribution are shown in Figure 4-16. In the simulation, three microlenses with 200 pixels each were used. The plots on the left are the original WDF of several example object signals. The middle plots are the measurable WDF if continuous samples are taken in both space and spatial frequency. The right plots show the resulting pixellated measurements compared with the original WDF of the object at the centers of the three microlenses. The three microlenses discretize the measurable WDF into three columns and 200 spatial frequency samples are taken within each column, as illustrated in Figure 4-15. These three columns are rearranged side-by-side into a vector, as shown in Figure 4-15. The shift of the columns is assumed to be compensated by proper pixel addressing.

Figure 4-16(a) shows a point object with infinite spatial frequency, as shown in the right plot. The spatial frequency is cut off by the finite NA of the field lens, which results in a band-limited measurable WDF. The measurable WDF is a convolution between the band-limited object WDF and the WDF of the rectangular aperture. The resulting WDF has a rectangular shape in the Wigner space, as shown in the middle plot. The measurable WDF is discretized in space by the microlenses and in spatial frequency by the sensor pixels, which produces the pixellated WDF measurements in the right plot.

Figure 4-16(b) shows a Gaussian signal with a spatial extent larger than the size of a microlens. The region outside the second microlens, L2, is measured by the neighboring microlenses, L1 and L3, which produces two peaks in the right plot. The space coordinates only take discrete values that correspond to the centers of the microlenses. As a result, the peaks are the measured WDF vectors at these positions, pixels 100 and 500 in the figure, with varying spatial frequencies. The results are compared with the true WDF at pixels 100 and 500. The measurements have a larger value due to the integration defined in Equation (4.75).

Figure 4-16(c) shows a Gaussian signal whose space and spatial frequency extent

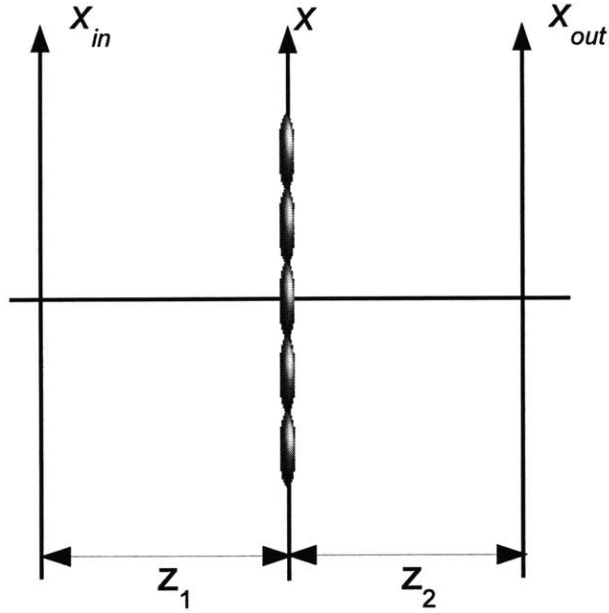


Figure 4-17: Integral imaging system setup.

fit to the space and spatial frequency support of the central microlens, L2. The right plot shows a good match between the measurements and the true value.

Figure 4-16(d) shows a Gaussian signal with its spatial frequency extent larger than the spatial frequency support of the system. The high frequency components of the signal get cut off as shown in both the middle and right plots.

4.3 Wave optics analysis of integral imaging

The integral imaging system, conjugate to the light field imaging system, is studied in this section. The difference of an integral imaging system is that no field lens is in front of the microlens array. Perspective images are taken by multiple microlenses onto the sensor plane. The system arrangement is shown in Figure 4-17. Similar to the previous discussions on the light field imaging system, the cPSF, iPSF and partially coherent imaging output of an integral imaging system will be studied in the section.

4.3.1 Coherent Point Spread Function

The field at the output plane is

$$g_{\text{out}}(x_{\text{out}}) = \sum_{k=-l}^l \iint dx_{\text{in}} dx g_{\text{in}}(x_{\text{in}}) \exp \left\{ i\pi \frac{x_{\text{in}}^2}{\lambda z_1} \right\} \text{rect} \left(\frac{x - k\Lambda}{\Lambda} \right) \exp \left\{ i\pi \frac{\psi x^2}{\lambda} \right\} \\ \exp \left\{ i \frac{2\pi}{\lambda} \left(-\frac{x_{\text{in}}}{z_1} - \frac{x_{\text{out}}}{z_2} + \frac{k\Lambda}{f_m} \right) x \right\} \exp \left\{ -i\pi \frac{(k\Lambda)^2}{\lambda f_m} \right\}. \quad (4.76)$$

where

$$\psi = \frac{1}{z_1} + \frac{1}{z_2} - \frac{1}{f_m} \quad (4.77)$$

denotes the amount of defocus.

The cPSF of the system is derived by assuming a point object at x_0 ,

$$\text{cPSF}(x_{\text{out}}) = \sum_{k=-l}^l \int dx \text{rect} \left(\frac{x - k\Lambda}{\Lambda} \right) \exp \left\{ i\pi \frac{\psi x^2}{\lambda} \right\} \\ \exp \left\{ i \frac{2\pi}{\lambda} \left(-\frac{x_0}{z_1} - \frac{x_{\text{out}}}{z_2} + \frac{k\Lambda}{f_m} \right) x \right\} \exp \left\{ -i\pi \frac{(k\Lambda)^2}{\lambda f_m} \right\}. \quad (4.78)$$

4.3.2 Incoherent Point Spread Function

Assume in-focus object

$$\psi = 0. \quad (4.79)$$

The iPSF of this system can be derived as

$$\text{iPSF}(x_{\text{out}}) = \int dx \sum_{k_-} \sum_{k_+} \mathcal{W}_{\text{rect}(\frac{x}{\Lambda})} \left(x - \frac{k_+ \Lambda}{2}, -\frac{x_0}{\lambda z_1} - \frac{x_{\text{out}}}{\lambda z_2} + \frac{k_+ \Lambda}{2\lambda f_m} \right) \\ \exp \left\{ i2\pi \left(-\frac{x_0}{\lambda z_1} - \frac{x_{\text{out}}}{\lambda z_2} + \frac{x}{\lambda f_m} \right) k_- \Lambda \right\}, \quad (4.80)$$

By letting

$$\begin{aligned}
x' &= x - \frac{k_+\Lambda}{2}, \\
u_0 &= -\frac{x_0}{\lambda z_1} - \frac{x_{\text{out}}}{\lambda z_2} + \frac{k_+\Lambda}{2\lambda f_m}, \\
\alpha_0 &= 2\pi\left(-\frac{x_0}{\lambda z_1} - \frac{x_{\text{out}}}{\lambda z_2} + \frac{k_+\Lambda}{2\lambda f_m}\right)k_-\Lambda,
\end{aligned} \tag{4.81}$$

the iPSF takes the form

$$\text{iPSF}(x_{\text{out}}) = \sum_{k_+} \sum_{k_-} \exp(i\alpha_0) \int dx' \mathcal{W}_{\text{rect}(\frac{x}{\Lambda})}(x', u_0) \exp\left\{i2\pi\frac{k_-\Lambda}{\lambda f_m}x'\right\}. \tag{4.82}$$

Since

$$\int dx' \mathcal{W}_f(x', u_0) \exp\left\{i2\pi\frac{k_-\Lambda}{\lambda f_m}x'\right\} = F\left(u_0 + \frac{k_-\Lambda}{2\lambda f_m}\right) F^*\left(u_0 - \frac{k_-\Lambda}{2\lambda f_m}\right), \tag{4.83}$$

where F is the Fourier transform of f . Here, $f(x) = \text{rect}(x/\Lambda)$, so

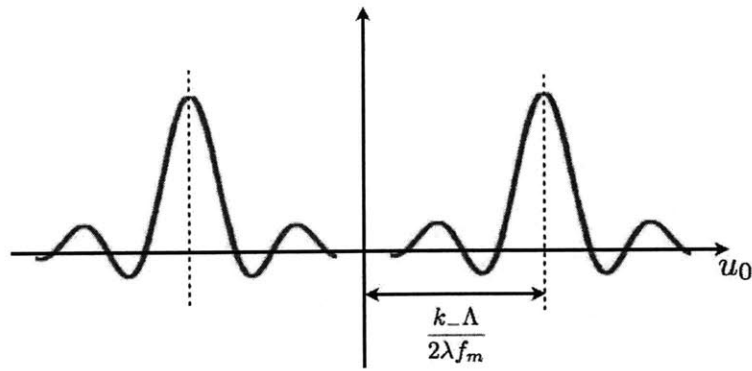
$$F(u) = \text{sinc}(\Lambda u). \tag{4.84}$$

The results of Equation (4.83) are illustrated in Figure 4-7. When k_- is large, two sinc functions will be separated by a large distance, thus the contribution of their product approximates zero, as shown in Figure 4-7(a). Figure 4-7(b) illustrates the marginal case, in which $k_- = \pm 1$, and the two sinc functions are separated by the distances equal to the width of their mainlobe. In this case, we approximate their product to be zero. Fig 4-7(c) shows the case where aliasing happens which results in cross-talk between neighboring microlenses.

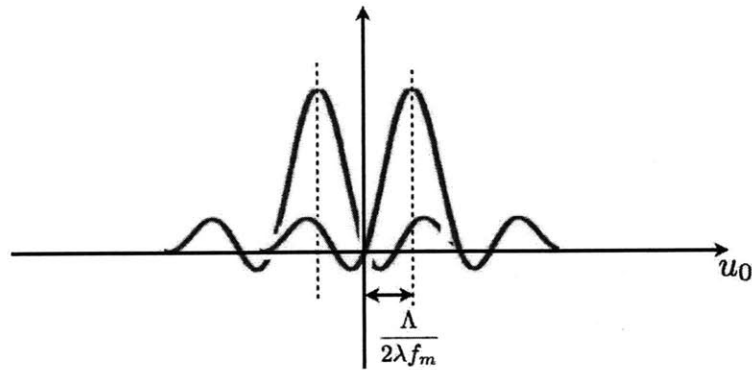
The requirement of no-cross-talk between sub-images can be derived as

$$\frac{\Lambda}{\lambda f_m} \geq \frac{2}{\Lambda}, \tag{4.85}$$

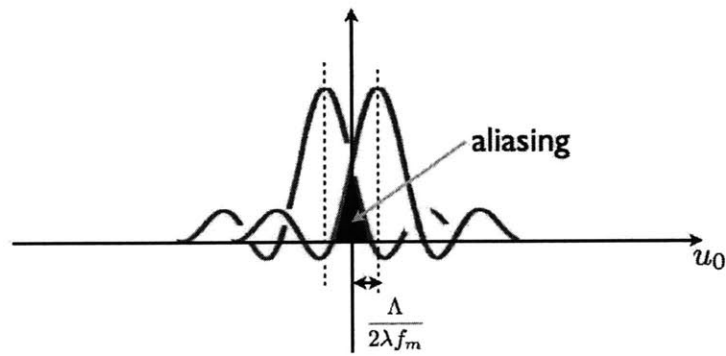
$$\Lambda \geq \sqrt{2\lambda f_m}, \tag{4.86}$$



(a)



(b)



(c)

Figure 4-18: Illustration of incoherent point spread function of integral imaging system.

where the width of the mainlobe of the sinc function is given by $2/\Lambda$. If Equation (4.86) is satisfied, then

$$k_- = 0, \text{ and } k_+/2 \text{ only takes integer value.} \quad (4.87)$$

Equation (4.80) is simplified as

$$\text{iPSF}(x_{\text{out}}) = \sum_{k=-l}^l \left| \text{sinc} \left(\frac{\Lambda}{\lambda} \left(-\frac{x_0}{z_1} - \frac{x_{\text{out}}}{z_2} + \frac{k\Lambda}{f_m} \right) \right) \right|^2 \quad (4.88)$$

The results of Equation (4.88) show that a point object at x_0 results in multiple output image due to the microlens array. The space is being sampled as different locations at the sensor plane x_{out} . The spatial frequency is sampled by different microlenses.

In addition, several properties of the image can be studied:

(1) Centers of the output images are located at

$$(x_{\text{out}} - k\Lambda) = -\frac{z_2}{z_1}(x_0 - k\Lambda). \quad (4.89)$$

which is the same as the result predicted by geometrical optics.

(2) Width of the mainlobe, w , which limits the spatial resolution is

$$\begin{aligned} w &= \frac{2\lambda z_2}{\Lambda} = \frac{\lambda}{\text{NA}}, \\ \text{NA} &= \frac{\Lambda}{2z_2}. \end{aligned} \quad (4.90)$$

(3) Digital refocusing: neglecting the cross-talk, the defocused-iPSF is,

$$\text{iPSF}_d(x_{\text{out}}) = \sum_{k=-l}^l \int dx \mathcal{W}_{\text{rect}(\frac{x}{\Lambda})} \left(x - k\Lambda, \frac{\psi x}{\lambda} - \frac{x_0}{\lambda z_1} - \frac{x_{\text{out}}}{\lambda z_2} + \frac{k\Lambda}{\lambda f_m} \right). \quad (4.91)$$

Equation (4.91) is in the form of a Fractional Fourier Transform (FrFT) of the rect function, with defocus ψ determining the fractional power. Fast digital refocusing

can be done using the Fourier Slicing Theorem [82].

4.3.3 Partially coherent imaging

The output intensity with an in-focus object can be derived as

$$I(x_{\text{out}}) = \sum_{k=-l}^l \iint dx_{\text{in}} dx \mathcal{W}_{g_{\text{in}}} \left(x_{\text{in}}, \frac{x_{\text{in}} - x}{\lambda z_1} \right) \mathcal{W}_{\text{rect}(\frac{x}{\Lambda})} \left(x - k\Lambda, -\frac{x_{\text{in}}}{\lambda z_1} - \frac{x_{\text{out}}}{\lambda z_2} + \frac{k\Lambda}{\lambda f_m} \right) \quad (4.92)$$

Equation (4.92) implies that an integral imaging system samples the object WDF. It takes discrete spatial frequency samples at the microlens plane, $k\Lambda$, and spatial samples at the sensor plane, $(x_{\text{out}} - k\Lambda)/\lambda z_3$. The result is an object WDF blurred by a 90 degree rotated WDF of a rect function. The 90 degree rotated WDF of a rect function is equivalent to the WDF of a sinc function. Similar to the light field derivation, the integral imaging output image can be written as a convolution between an object WDF and the WDF of a sinc function.

$$I(x, u) \sim \mathcal{W}_{g_{\text{in}}}(x, u) *_{x,u} \mathcal{W}_{\text{sinc}(\frac{x}{\Lambda})}(x, u), \quad (4.93)$$

and the discretization in the space domain is realized by integrating all values within each spatial frequency pixel

$$I(x, k\Lambda) = \int_{(k-1/2)\Lambda}^{(k+1/2)\Lambda} I(x, u) du. \quad (4.94)$$

The result of Equation (4.93) is illustrated in Figure 4-19. The WDF of the object, \mathcal{W}_g , is space and spatial frequency limited due to the finite NA of the microlens, depicted as the grey area in the figure. The low-pass filtered object WDF is convolved with the WDF of a sinc function. Each dashed line enclosed group corresponds to a microlens. The shifts of the spatial samples are due to the lateral displacement of the microlenses. The number of spatial samples is determined by the number of pixels behind a microlens. The number of spatial frequency samples is determined by the

number of microlenses. The sample arrangement on the sensor plane is illustrated in the right-hand side of the figure.

4.3.4 Simulation results

Simulations to better illustrate how an integral imaging system measures the object Wigner distribution are shown in Figure 4-20. In the simulation, three microlenses with 100 pixels each were used. The left plots are the original WDF of several example object signals. The middle plots are the measurable WDF if continuous samples are taken in both space and spatial frequency. The right plots show the resulting pixellated measurements compared with the original WDF of the object at the centers of the three microlenses. The three microlenses discretize the measurable WDF into three spatial frequency groups and 100 spatial samples are taken within each group, as illustrated in Figure 4-19. These three spatial frequency groups are rearranged side-by-side into a vector, as shown in Figure 4-19. The lateral shift is assumed to be compensated by proper pixel addressing.

Figure 4-20(a) shows a point object. Its WDF is a δ -function along the spatial frequency axis. The measurable WDF is a convolution between the δ -function and the WDF of the sinc aperture. The resulting WDF is shown in the middle figure. The measurable WDF is discretized in spatial frequency by the microlenses and in space by the sensor pixels, which produces the pixellated WDF measurements at the sensor plane, as shown in the right hand-side plot. Under each microlens, a sinc-shaped intensity pattern is produced, as derived in Equation (4.45).

Figure 4-20(b) shows a Gaussian signal with its spatial frequency extent larger than the NA of the microlens. The region outside the second microlens, L2, is measured by the neighboring microlenses, L1 and L3, which produces two peaks shown in the right figure. The spatial frequency coordinates only take discrete values that correspond to the centers of the microlenses. As a result, the peaks are the measured WDF vectors at these spatial frequencies, $u = \pm 0.01$, with varying space coordinates. The results are compared with the true WDF at $u = \pm 0.01$. The measurements have a larger value due to the integration in Equation (4.94), as shown in the right figure.

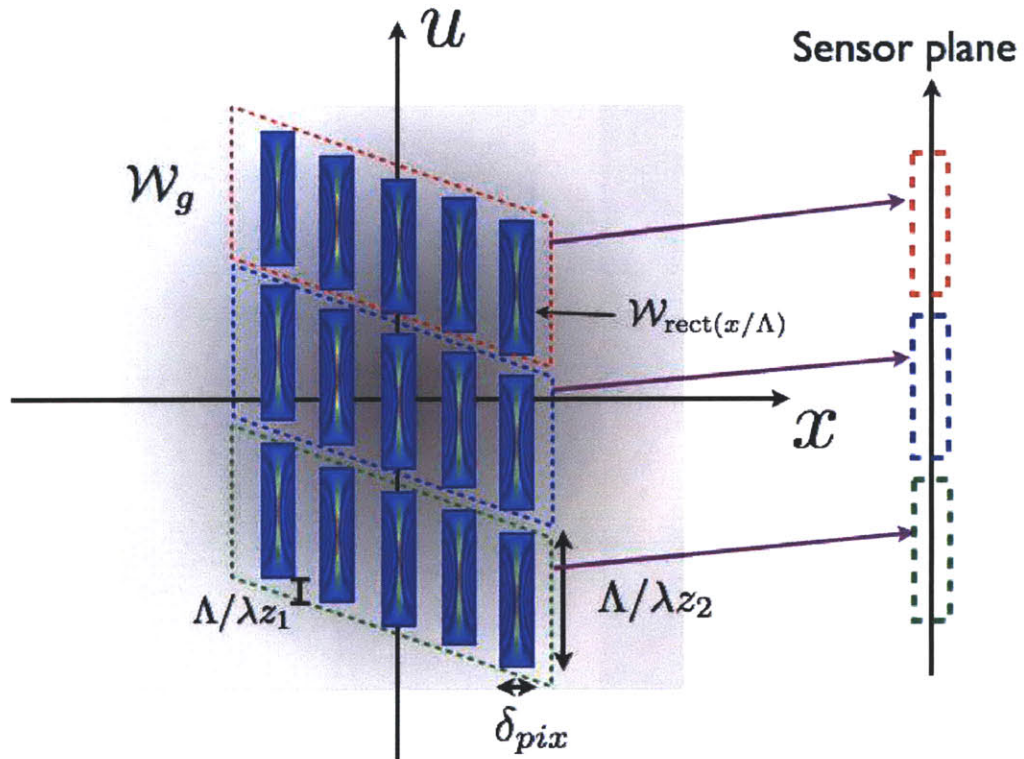
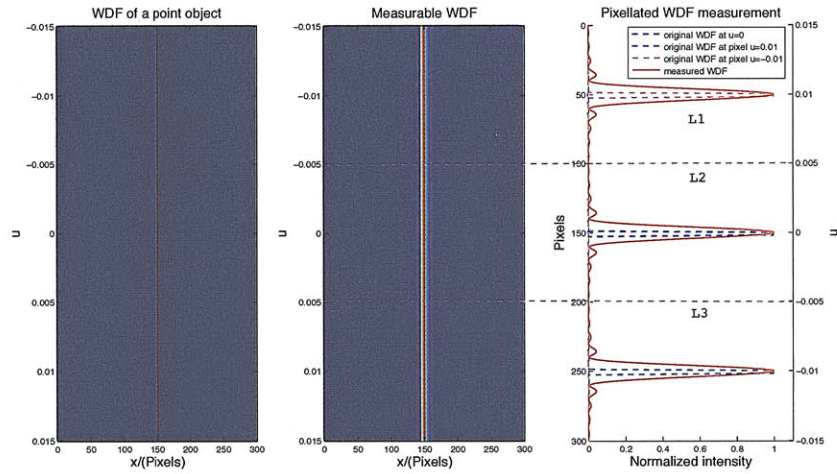
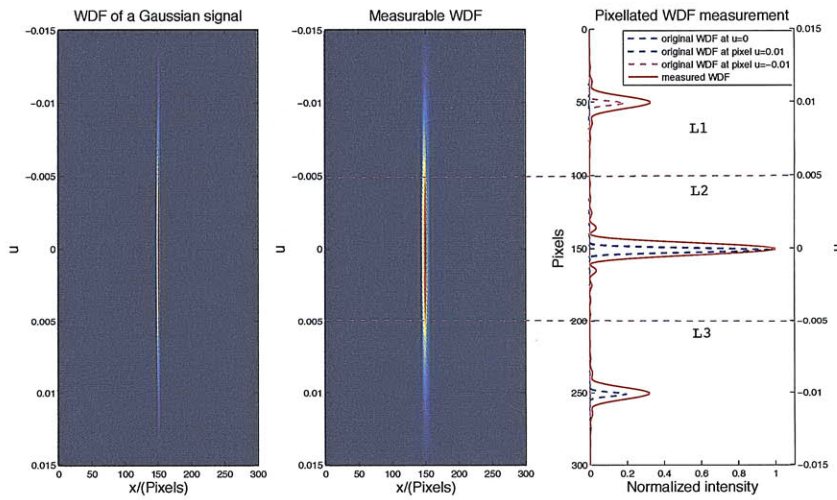


Figure 4-19: Sampling in the Wigner space by an integral imaging system. The object WDF is convolved with the WDF of a sinc function. The convolution process is depicted as the replicas of the WDF of a sinc function along both the spatial and spatial frequency axis directions. Three spatial frequency samples are taken, depicted as three groups enclosed by dashed lines. Each spatial frequency sample has a width of $\Lambda/\lambda z_2$. 5 spatial samples are taken at each spatial frequency. Each spatial sample has a width of pixel size, δ_{pix} . Neighboring spatial samples are shifted by $\Lambda/\lambda z_1$ due to the physical displacements of different microlenses. The samples are recorded on a 1D sensor. The sample arrangement on the sensor is shown to the right.

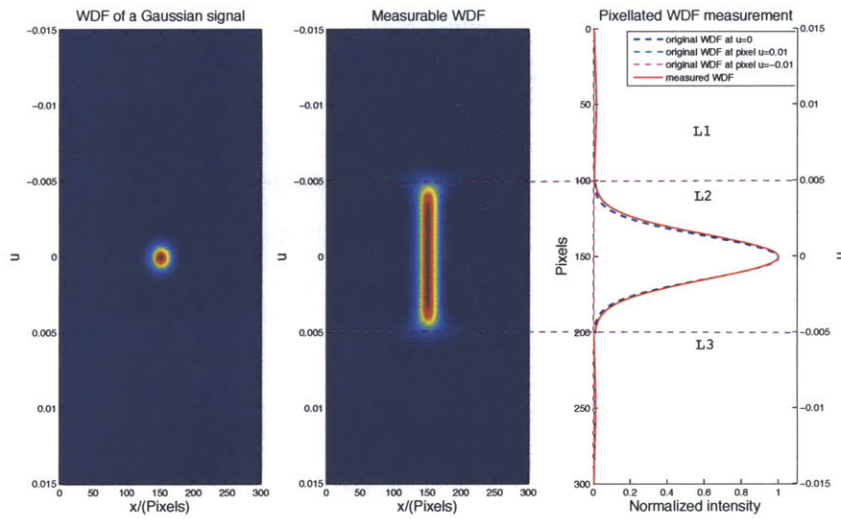


(a) Point object

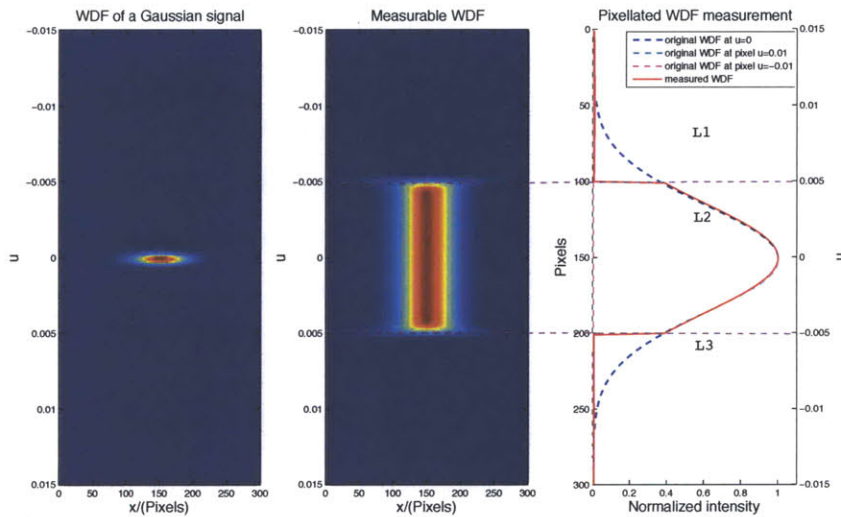


(b) Gaussian signal with large spatial frequency extent

Figure 4-20



(c) Gaussian signal with limited space and spatial frequency extent



(d) Gaussian signal with large spatial extent, high space contents are cut off if non-overlapping requirement is achieved

Figure 4-20: Left: the original WDF of example object signals; middle: the measurable WDF, if continuous samples are taken in both space and spatial frequency; right: the resulting pixellated measurements (solid red line) and it is compared with the original WDF of the object at u equals to 0, 0.01 and -0.01 in the left plots (cyan, blue and magenta dashed lines). The three microlenses discretize the measurable WDF into three groups. 100 spatial samples are taken within each group. These three groups are rearranged side-by-side into a vector.

Figure 4-20(c) shows a Gaussian signal with its space and spatial frequency extent fit to the space and spatial frequency support of the central microlens, L2.

The right plot shows good match between the measurements and the true value. Figure 4-20(d) shows a Gaussian signal with spatial extent larger than the spatial support if the non-overlapping between sub-images condition is achieved. The solid red line shows the measured WDF if the high spatial contents of the signal are cut off. The difference between the blue dashed line and the solid red line in the right plot is the overlapping/cutoff region.

4.4 Conclusion

In this chapter, the generalized radiance function, and the relations between the radiance and the Wigner distribution are first reviewed. Due to the uncertainty principle, accurate measurements in both space and spatial frequency domain are not achievable. An approach by scanning a finite aperture to measure the Wigner distribution is studied, resulting the measurable WDF. Two systems, the light field imaging system and the integral imaging system, are studied. Both systems produce images that can be described as measurable WDFs. In the light field imaging system, the aperture function is a rect function. In the integral imaging system, the aperture function is a sinc function.

Chapter 5

Conclusion

As semiconductor fabrication technology advances, sensors and cameras with increasingly high space-bandwidth product and high temporal sampling rate become available. In addition, increasing computational power makes implementing complicated post-processing practical. By incorporating optics, advanced algorithms and digital processing, computational imaging optimizes the tradeoffs between the optical and digital world.

Two types of computational imaging systems, digital holographic imaging and light field imaging, have been studied in this thesis. Analysis has been carried out with the aid of phase-space optics tools. Both imaging systems record the optical signals in an unconventional way, and object information can be recovered by special designed post-processing. In digital holography, the complex amplitude of the object wave is encoded in an interferogram. Fresnel approximated propagation can be applied to recover the original field given that the first Born approximation holds [8]. In light field imaging, the object Wigner distribution is sampled at the sensor plane. The object intensity can be retrieved by integrating the samples along the (rotated) spatial frequency axis in the Wigner space.

To conclude this thesis, all the presented topics are summarized and future research directions are presented.

5.1 Digital holographic imaging

It is seen that insightful understanding of holography can be obtained through phase-space optics analysis. By tracking Space Bandwidth transfer, the information transformation through a digital holographic imaging system can be traced. The inverse source problem of holography can be solved in certain cases by posing proper *priori* constraints. As is seen in its application to two-phase flows, 3D positions of bubbles can be computed by well tuned focus metrics applied to the reconstructed images. Size statistical distribution of the bubbles can also be obtained from the reconstructed images.

There are several interesting topics for future work:

Digital holography applied to two-phase flows

1) The robustness and adaptability of the developed digital holographic image processing algorithms should be tested and improved.

2) Statistical validations of the quantitative results produced by this technique should be verified by comparison with existing simulation and experimental results.

3) With the aid of Graphic Processing Unit (GPU), real-time digital holographic imaging is feasible. It is useful to implement the two-phase flow imaging experiments with GPU accelerated algorithms.

Inverse source problem

It is well known that holography only records spectral information on a spherical cap in the k -sphere space [112]. It is interesting to look into the inverse source problem with random sources. The *prior* information plays a key role in finding the unique solutions of the inverse source problem. The mathematical formulation of the interplay between the recorded information and *prior* constraints in inverse problem is interesting. Better understanding of the inverse source problem might lead to wider applications of digital holography. Another interesting application for solving inverse source problem is 3D intensity pattern generation.

Digital holographic imaging using partially coherent illumination

It is known that partially coherent illumination could result in higher resolution [8]. In particle holograms, partially coherent illumination could reduce cross-talk between different particles. On the other hand, the intensity measurements on the sensor do not contain the full information of the mutual intensity of the field, which decreases the resolution. In practice, the resolution is influenced by a number of other factors. It is interesting to study how the degree of coherence influences the lateral and axial resolution of holographic and light field/integral imaging systems.

5.2 Light field imaging

Light field is equivalent to the radiance, and the generalized radiance function equals to the Wigner distribution. One practical way to sample Wigner distribution is to take intensity measurements behind an aperture which is moving laterally in the field. Two types of imaging systems, the light field imaging and the integral imaging, realize this Wigner sampling scheme. In light field imaging, the aperture function is a rect function. In integral imaging, the aperture function is a sinc function. Another application for both the light field imaging and the integral imaging is digital refocusing, which provides axial ranging through the object space. In addition, imaging through partial occlusions is possible by integrating samples from different sub-images.

For future work, several interesting topics are related to the light field imaging

Sampling in the phase space

The light field imaging and integral imaging provide an idea to sample in the phase space. It is interesting to look into other ways to sample in the phase space by choosing proper aperture functions.

Imaging through partial occlusion

It is interesting to conduct the following successive experiments: (i) Build a prototype of a light field imaging system and carry out experiments without occlusions . Develop the image reconstruction algorithm, which takes different projections along different directions in Wigner space and integrates these projections. (ii) An experimental system where targets of known shape inserted in murky water of controlled composition, in terms of particle size and density, apply Bayesian estimation techniques to establish discrimination capability for known targets of different shapes achieved by different strategies of reconstruction algorithms.

Bibliography

- [1] E. H. Adelson and J. R. Bergen. The plenoptic function and the elements of early vision. In *Computational Models of Visual Processing*, pages 3–20. Cambridge, MA: MIT Press, 1991.
- [2] E. H. Adelson and J. Y. A. Wang. Single lens stereo with a plenoptic camera. *IEEE Trans. Pattern Anal. Mach. Intell.*, 14(2):99–106, 1992.
- [3] R. J. Adrian. Twenty years of particle image velocimetry. *Experiments in Fluids*, 39:159–169, August 2005.
- [4] H. Arimoto and B. Javidi. Integral three-dimensional imaging with digital reconstruction. *Opt. Lett.*, 26(3):157–159, 2001.
- [5] M. J. Bastiaans. The Wigner distribution function applied to optical signals and systems. *Optics Communications*, 25:26–30, April 1978.
- [6] M. J. Bastiaans. Wigner distribution function and its application to first-order optics. *J. Opt. Soc. Am.*, 69(12):1710–1716, 1979.
- [7] M. J. Bastiaans. Applications of the Wigner distribution function to partially coherent light beams. volume 3729 of *SPIE Proceedings*, pages 114–128, April 1999.
- [8] M. Born and E. Wolf. *Principles of Optics: Electromagnetic Theory of Propagation, Interference and Diffraction of Light*. Cambridge University Press, 7 edition, October 1999.
- [9] C. Brücker. 3D scanning PIV applied to an air flow in a motored engine using digital high-speed video. *Measurement Science and Technology*, 8(scanning PIV):1480–1492, December 1997.
- [10] C. W. McCutchen. Generalized aperture and the three-dimensional diffraction image. *J. Opt. Soc. Am.*, 54(2):240–242, 1964.
- [11] D. Carl, B. Kemper, G. Wernicke, and G. Bally. Parameter-optimized digital holographic microscope for high-resolution living-cell analysis. *Appl. Opt.*, 43(36):6536–6544, 2004.

- [12] H Chanson. Air bubble entrainment in open channels: Flow structure and bubble size distributions. *International Journal of Multiphase Flow*, 23(1):193–203, February 1997.
- [13] F. C. Cheong, B. Sun, R. Dreyfus, J. Amato-Grill, K. Xiao, L. Dixon, and D. G. Grier. Flow visualization and flow cytometry with holographic video microscopy. *Opt. Express*, 17(15):13071–13079, 2009.
- [14] L. Cohen. Time-frequency distributions - A review. *IEEE Proceedings*, 77:941–981, July 1989.
- [15] S. A. Collins, JR. Lens-system diffraction integral written in terms of matrix optics. *J. Opt. Soc. Am.*, 60(9):1168–1177, 1970.
- [16] I. J. Cox and C. J. R. Sheppard. Information capacity and resolution in an optical system. *Journal of the Optical Society of America A*, 3:1152–1158, August 1986.
- [17] R. B. D’Agostino and M. A. Stephens. *Goodness-of-fit techniques*, volume 68 of *Statistics, textbooks and monographs*. Marcel Dekker Inc., 1986.
- [18] J. A. Dominguez-Caballero. Digital holographic imaging of aquatic species. Master’s thesis, Massachusetts Institute of Technology, February 2006.
- [19] J. A. Dominguez-Caballero and G. Barbastathis. Stability of inversion in digital holographic particle imaging: Theory and experimental validation. In *Frontiers in Optics*, page FThV4. Optical Society of America, 2008.
- [20] J. A. Dominguez-Caballero, N. Loomis, W. Li, Q. Hu, J. Milgram, G. Barbastathis, and C. Davis. Advances in plankton imaging using digital holography. In *Computational Optical Sensing and Imaging*, page DMB5. Optical Society of America, 2007.
- [21] E. R. Dowski, Jr. and W. T. Cathey. Extended depth of field through wave-front coding. *Appl. Opt.*, 34:1859–+, April 1995.
- [22] F. Dubois, C. Schockaert, N. Callens, and C. Yourassowsky. Focus plane detection criteria in digital holography microscopy by amplitude analysis. *Opt. Express*, 14(13):5895–5908, June 2006.
- [23] J. R. Fienup. Phase retrieval algorithms: a comparison. *Appl. Opt.*, 21(15):2758–2769, 1982.
- [24] J. T. Foley and E. Wolf. Radiometry as a short-wavelength limit of statistical wave theory with globally incoherent sources. *Optics Communications*, 55:236–241, September 1985.
- [25] G. T. D. Francia. Resolving power and information. *J. Opt. Soc. Am.*, 45(7):497–499, 1955.

- [26] D. Freedman and P. Diaconis. On the histogram as a density estimator-l2 theory. *Zeitschrift Fur Wahrscheinlichkeitstheorie Und Verwandte Gebiete*, 57(4):453–476, 1981.
- [27] A. T. Friberg. On the existence of a radiance function for finite planar sources of arbitrary states of coherence. *J. Opt. Soc. Am.*, 69(1):192–198, 1979.
- [28] B. R. Frieden. Optical transfer of the three-dimensional object. *J. Opt. Soc. Am.*, 57(1):56–65, 1967.
- [29] W. D. Furlan, M. Martínez-Corral, B. Javidi, and G. Saavedra. Analysis of 3-D integral imaging displays using the Wigner distribution. *J. Display Technol.*, 2(2):180–185, 2006.
- [30] W. D. Furlan, C. Soriano, and G. Saavedra. Opto-digital tomographic reconstruction of the Wigner distribution function of complex fields. *Appl. Opt.*, 47(22):E63–E67, 2008.
- [31] D. Gabor. A New Microscopic Principle. *Nature*, 161:777–778, May 1948.
- [32] A. Gershun. The light field. *J. Math. and Physics*, 18:51–151, 1936.
- [33] J. Gillespie and R. King. The use of self-entropy as a focus measure in digital holography. *Pattern Recognition Letters*, 9(1):19–25, January 1989.
- [34] J. W. Goodman. *Introduction to Fourier optics*. Roberts & Company Publishers, 3 edition, 2004.
- [35] F. Gori. Fresnel transform and sampling theorem. *Optics Communications*, 39:293–297, November 1981.
- [36] S. J. Gortler, R. Grzeszczuk, R. Szeliski, and M. F. Cohen. The lumigraph. In *SIGGRAPH '96: Proceedings of the 23rd annual conference on Computer graphics and interactive techniques*, pages 43–54, New York, NY, USA, 1996.
- [37] B. Javidi and E. Tajahuerce. Three-dimensional object recognition by use of digital holography. *Opt. Lett.*, 25(9):610–612, 2000.
- [38] A. C. Kak and M. Slaney. *Principles of computerized tomographic imaging*. IEEE Service Center, Piscataway, NJ, 1988.
- [39] J. Katz and J. Sheng. Applications of holography in fluid mechanics and particle dynamics. *Annual Review of Fluid Mechanics*, 42(1):531–555, 2010.
- [40] K. Kim and E. Wolf. Propagation law for walther’s first generalized radiance function and its short-wavelength limit with quasi-homogeneous sources. *J. Opt. Soc. Am. A*, 4(7):1233–1236, 1987.

- [41] T. Kim and T. C. Poon. Three-dimensional matching by use of phase-only holographic information and the Wigner distribution. *J. Opt. Soc. Am. A*, 17:2520–2528, December 2000.
- [42] T. Latychevskaia and H. Fink. Solution to the twin image problem in holography. *Phys. Rev. Lett.*, 98(23):233901–233901–4, 2007.
- [43] E. N. Leith and J. Upatnieks. Reconstructed wavefronts and communication theory. *J. Opt. Soc. Am.*, 52(10):1123–1128, 1962.
- [44] M. Levoy. Light fields and computational imaging. *Computer*, 39(8):46–55, 2006.
- [45] M. Levoy, B. Chen, V. Vaish, M. Horowitz, I. McDowall, and M. Bolas. Synthetic aperture confocal imaging. *ACM Trans. Graph.*, 23(3):825–834, 2004.
- [46] M. Levoy and P. Hanrahan. Light field rendering. In *SIGGRAPH '96: Proceedings of the 23rd annual conference on Computer graphics and interactive techniques*, pages 31–42, New York, NY, USA, 1996.
- [47] M. Levoy, R. Ng, A. Adams, M. Footer, and M. Horowitz. Light field microscopy. In *SIGGRAPH '06*, pages 924–934, New York, NY, USA, 2006.
- [48] W. Li, N. Loomis, Q. Hu, and C. S. Davis. Focus detection from digital in-line holograms based on spectral $l(1)$ norms. *J. Opt. Soc. Am. A*, 24(10):3054–3062, October 2007.
- [49] G. Lippmann. La photographie integrale. *Comptes-Rendus, Academie des Sciences*, 146(446-551), 1908.
- [50] A. W. Lohmann. Image rotation, Wigner rotation, and the fractional Fourier transform. *J. Opt. Soc. Am. A*, 10(10):2181–2186, 1993.
- [51] A. W. Lohmann, R. G. Dorsch, D. Mendlovic, Z. Zalevsky, and C. Ferreira. Space-bandwidth product of optical signals and systems. *J. Opt. Soc. Am. A*, 13(3):470–473, 1996.
- [52] A. W. Lohmann and B. H. Soffer. Relationships between the Radon-Wigner and fractional Fourier transforms. *J. Opt. Soc. Am. A*, 11(6):1798–1801, 1994.
- [53] A. W. Lohmann, M. Testorf, and J. Ojeda-Castañeda. Holography and the Wigner function. *Proceedings of SPIE*, 4737(1):77–88, 2002.
- [54] N. Loomis and G. Barbastathis. Space-Bandwidth transfer in spherical reference holography using Wigner transforms. In *Digital Holography and Three-Dimensional Imaging*, page DMB4. Optical Society of America, 2009.
- [55] L. Ma, H. Wang, Y. Li, and H. Jin. Numerical reconstruction of digital holograms for three-dimensional shape measurement. *Journal of Optics A-Pure and Applied Optics*, 6(4):396–400, April 2004.

- [56] E. W. Marchand and E. Wolf. Walther's definitions of generalized radiance. *J. Opt. Soc. Am.*, 64(9):1273–1274, 1974.
- [57] C. P. McElhinney, J. B. McDonald, A. Castro, Y. Frauel, B. Javidi, and T. J. Naughton. Depth-independent segmentation of macroscopic three-dimensional objects encoded in single perspectives of digital holograms. *Opt. Lett.*, 32(10):1229–1231, May 2007.
- [58] D. Mendlovic and H. M. Ozaktas. Fractional Fourier transforms and their optical implementation: I. *J. Opt. Soc. Am. A*, 10(9):1875–1881, 1993.
- [59] D. Mendlovic, H. M. Ozaktas, and A. W. Lohmann. Graded-index fibers, Wigner-distribution functions, and the fractional Fourier transform. *Appl. Opt.*, 33:6188–6193, 1994.
- [60] J. H. Milgram and W. Li. Computational reconstruction of images from holograms. *Appl. Opt.*, 41:853–864, February 2002.
- [61] K. Mishima and T. Hibiki. Development of high-frame-rate neutron radiography and quantitative measurement method for multiphase flow research. *Nuclear Engineering and Design*, 184(2-3):183 – 201, 1998.
- [62] I. Moon, M. Daneshpanah, B. Javidi, and A. Stern. Automated three-dimensional identification and tracking of micro/nanobiological organisms by computational holographic microscopy. *Proceedings of the IEEE*, 97(6):990–1010, June 2009.
- [63] P. Moon and D. E. Spencer. *The photic field*. Cambridge, MA, MIT Press, 1981.
- [64] A. Naqwi, F. Durst, and G. Kraft. Sizing of submicrometer particles using a phase-doppler system. *Appl. Opt.*, 30(33):4903–4913, 1991.
- [65] R. Ng. Fourier slice photography. In *SIGGRAPH '05: ACM SIGGRAPH 2005 Papers*, pages 735–744, New York, NY, USA, 2005.
- [66] R. Ng, M. Levoy, M. Bredif, G. Duval, M. Horowitz, and P. Hanrahan. Light field photography with a hand-held plenoptic camera. Technical Report CTSR 2005-02, Stanford, 2005.
- [67] K. A. Nugent. X-ray noninterferometric phase imaging: a unified picture. *J. Opt. Soc. Am. A*, 24(2):536–547, 2007.
- [68] S. B. Oh and G. Barbastathis. Axial imaging necessitates loss of lateral shift invariance: proof with the Wigner analysis. *Appl. Opt.*, 48(30):5881–5888, 2009.
- [69] S. B. Oh and G. Barbastathis. Wigner analysis of 3-d coherence imaging. In *Computational Optical Sensing and Imaging*, page CTuD4. Optical Society of America, 2009.

- [70] S. B. Oh and G. Barbastathis. Wigner distribution function of volume holograms. *Opt. Lett.*, 34(17):2584–2586, 2009.
- [71] L. Onural. Sampling of the diffraction field. *Appl. Opt.*, 39(32):5929–5935, 2000.
- [72] L. Onural and M. T. Özgen. Extraction of three-dimensional object-location information directly from in-line holograms using Wigner analysis. *J. Opt. Soc. Am. A*, 9(2):252–260, 1992.
- [73] N. Opedal, G. Sørland, and J. Sjöblom. Methods for droplet size distribution determination of water-in-oil emulsions using low-field NMR. *The Open-Access Journal for the Basic Principles of Diffusion Theory, Experiment and Application* 7:1–29, 2009.
- [74] H. M. Ozaktas and D. Mendlovic. Fractional Fourier transforms and their optical implementation: II. *J. Opt. Soc. Am. A*, 10(12):2522–2531, 1993.
- [75] H. M. Ozaktas, Z. Zalevsky, and M. A. Kutay. *The Fractional Fourier Transform: with Applications in Optics and Signal Processing*. Wiley, 2001.
- [76] A. K. Ozdemir and O. Arikan. Fast computation of the ambiguity function and the Wigner distribution on arbitrary line segments. *IEEE Transactions on Signal Processing*, 49:381–393, February 2001.
- [77] M. T. Özgen. Automatic kernel design procedure for Cohen’s bilinear class of representations as applied to in-line Fresnel holograms. *Optics Communications*, 174:51–67, January 2000.
- [78] M. T. Özgen. Analysis of in-line Fresnel holograms via chirp separation. *Optical Engineering*, 45(3):035801–+, March 2006.
- [79] M. T. Özgen and K. Demirbas. Cohen’s bilinear class of shift-invariant space/spatial-frequency signal representations for particle-location analysis of in-line Fresnel holograms. *J. Opt. Soc. Am. A*, 15(8):2117–2137, 1998.
- [80] G. Pan and H. Meng. Digital holography of particle fields: reconstruction by use of complex amplitude. *Appl. Opt.*, 42(5):827–833, February 2003.
- [81] A. Papoulis. Ambiguity function in Fourier optics. *J. Opt. Soc. Am.*, 64(6):779–788, 1974.
- [82] J. Park, K. Hong, and B. Lee. Recent progress in three-dimensional information processing based on integral imaging. *Appl. Opt.*, 48(34):H77–H94, 2009.
- [83] F. Pereira, M. Gharib, D. Dabiri, and D. Modarress. Defocusing digital particle image velocimetry: a 3-component 3-dimensional DPIV measurement technique. Application to bubbly flows. *Experiments in Fluids*, 29(Suppl. S):S78–S84, Dec 2000.

- [84] B. C. Platt and R. Shack. History and principles of Shack-Hartmann wavefront sensing. *Journal of Refractive Surgery*, 17, 2001.
- [85] R. P. Porter. Diffraction-limited, scalar image formation with holograms of arbitrary shape. *J. Opt. Soc. Am.*, 60(8):1051–1059, 1970.
- [86] R. P. Porter and A. J. Devaney. Holography and the inverse source problem. *J. Opt. Soc. Am.*, 72:327–+, March 1982.
- [87] Y. Pu and H. Meng. Four-dimensional dynamic flow measurement by holographic particle image velocimetry. *Appl. Opt.*, 44(36):7697–7708, December 2005.
- [88] M. G. Raymer, M. Beck, and D. McAlister. Complex wave-field reconstruction using phase-space tomography. *Phys. Rev. Lett.*, 72(8):1137–1140, Feb 1994.
- [89] D. Reynolds and R. Rose. Robust Text-independent speaker identification using Gaussian Mixture Speaker Models. *IEEE Trans. On Speech and Audio Processing*, 3(1):72–83, January 1995.
- [90] J. Rissanen. Stochastic complexity and modeling. *Ann. Statist.*, 14(3):1080–1100, 1986.
- [91] S. Satake, H. Kanamori, T. Kunugi, K. Sato, T. Ito, and K. Yamamoto. Parallel computing of a digital hologram and particle searching for microdigital-holographic particle-tracking velocimetry. *Appl. Opt.*, 46(4):538–543, 2007.
- [92] D. Scharstein, R. Szeliski, and R. Zabih. A taxonomy and evaluation of dense two-frame stereo correspondence algorithms. In *Proceedings of the IEEE Workshop on Stereo and Multi-Baseline Vision (SMBV'01)*, page 131, Washington, DC, USA, 2001. IEEE Computer Society.
- [93] U. Schnars. Direct phase determination in hologram interferometry with use of digitally recorded holograms. *J. Opt. Soc. Am. A*, 11(7):2011–2015, 1994.
- [94] U. Schnars and W. Jueptner. *Digital Holography: Digital Hologram Recording, Numerical Reconstruction, and Related Techniques*. Springer, 2005.
- [95] U. Schnars and W. P. Juptner. Direct recording of holograms by a CCD target and numerical reconstruction. *Appl. Opt.*, 33:179–181, January 1994.
- [96] R. Simon and K. B. Wolf. Structure of the set of paraxial optical systems. *J. Opt. Soc. Am. A*, 17(2):342–355, 2000.
- [97] G. Situ and J. T. Sheridan. Holography: an interpretation from the phase-space point of view. *Opt. Lett.*, 32(24):3492–3494, 2007.
- [98] A. Stern and B. Javidi. Sampling in the light of Wigner distribution. *J. Opt. Soc. Am. A*, 21(3):360–366, 2004.

- [99] A. Stern and B. Javidi. Sampling in the light of Wigner distribution: errata. *J. Opt. Soc. Am. A*, 21(10):2038–2038, 2004.
- [100] A. Stern and B. Javidi. Improved-resolution digital holography using the generalized sampling theorem for locally band-limited fields. *J. Opt. Soc. Am. A*, 23(5):1227–1235, 2006.
- [101] N. Streibl. Three-dimensional imaging by a microscope. *J. Opt. Soc. Am. A*, 2(2):121–127, 1985.
- [102] M. L. Tachiki, M. Itoh, and T. Yatagai. Simultaneous depth determination of multiple objects by focus analysis in digital holography. *Appl. Opt.*, 47(19):D144–D153, 2008.
- [103] M. Testorf, B. Hennelly, and J. Ojeda-Castañeda. *Phase-Space Optics: Fundamentals and Applications*. McGraw-Hill Professional, 2009.
- [104] M. Testorf and A.W. Lohmann. Holography in phase space. *Appl. Opt.*, 47(4):A70–A77, 2008.
- [105] L. Tian, N. Loomis, J. A. Dominguez-Caballero, and G. Barbastathis. Bubble size measurement in high-density air-water mixture flows with wide size distributions using digital holography. In *Frontiers in Optics*, page FThB1. Optical Society of America, 2009.
- [106] J. Varley. Submerged gas-liquid jets - bubble-size prediction. *Chemical Engineering Science*, 50(5):901–905, March 1995.
- [107] A. Walther. Radiometry and coherence. *J. Opt. Soc. Am.*, 58(9):1256–1259, 1968.
- [108] A. Walther. Radiometry and coherence. *J. Opt. Soc. Am.*, 63(12):1622–1623, 1973.
- [109] A. Walther. Propagation of the generalized radiance through lenses. *J. Opt. Soc. Am.*, 68:1606–+, November 1978.
- [110] A. Walther. Theorem on the uniqueness of the generalized radiance. *Opt. Lett.*, 3(4):127–129, 1978.
- [111] E. Wigner. On the quantum correction for thermodynamic equilibrium. *Physical Review*, 40(5):0749–0759, June 1932.
- [112] E. Wolf. Three-dimensional structure determination of semi-transparent objects from holographic data. *Optics Communications*, 1:153–156, September 1969.
- [113] E. Wolf. Coherence and radiometry. *J. Opt. Soc. Am.*, 68(1):6–17, 1978.
- [114] K. B. Wolf, M. A. Alonso, and G. W. Forbes. Wigner functions for Helmholtz wave fields. *J. Opt. Soc. Am. A*, 16(10):2476–2487, 1999.

- [115] K. B. Wolf and A. L. Rivera. Holographic information in the Wigner function. *Optics Communications*, 144:36–42, February 1997.
- [116] P. M. Woodward. *Probability and information theory, with applications to radar*. Pergamon Press, London, 1953.
- [117] I. Yamaguchi and T. Zhang. Phase-shifting digital holography. *Opt. Lett.*, 22(16):1268–1270, 1997.
- [118] Y. Yang, B. Kang, and Y. Choo. Application of the correlation coefficient method for determination of the focal plane to digital particle holography. *Appl. Opt.*, 47(6):817–824, 2008.
- [119] Z. Zhang and M. Levoy. Wigner distributions and how they relate to the light field. In *Proc. IEEE International Conference on Computational Photography*, April 2009.